# DERIVING CLOSURES FOR BUBBLY FLOWS USING DIRECT NUMERICAL SIMULATIONS

Samensteling promotiecommissie:

| | |
|---|---|
| Prof. dr. ing. M. Wessling, voorzitter | Universiteit Twente |
| Prof. dr. ir. J.A.M. Kuipers, promotor | Universiteit Twente |
| Dr. ir. M. van Sint Annaland, assistent-promotor | Universiteit Twente |
| Prof. dr. D. Bothe | Rheinisch-Westfälische T.H. Aachen |
| Dr. ir. W. Harteveld | Shell Global Solutions |
| Prof. dr. S.T. Johansen | SINTEF Materials & Chemistry |
| Prof. dr. ir. R.F. Mudde | Technische Universiteit Delft |
| Prof. dr. D. Lohse | Universiteit Twente |
| Prof. dr. ir. J.J.W. van der Vegt | Universiteit Twente |

This work is part of the research programme of the 'Stichting voor Fundamenteel Onderzoek der Materie (FOM)', which is financially supported by the 'Nederlandse Organisatie voor Wetenschappelijk Onderzoek (NWO)', and Shell Global Solutions.

Publisher:
PrintPartners Ipskamp BV, P.O. Box 333, 7500AH, Enschede, The Netherlands

Deriving closures for bubbly flows using Direct Numerical Simulations / by W. Dijkhuizen. – Enschede: University of Twente, 2008. – Proefschrift.



ISBN 978-90-365-2664-7

# DERIVING CLOSURES FOR BUBBLY FLOWS USING DIRECT NUMERICAL SIMULATIONS

## PROEFSCHRIFT

ter verkrijging van
de graad van doctor aan de Universiteit Twente,
op gezag van de rector magnificus,
prof. dr. W.H.M. Zijm,
volgens besluit van het College voor Promoties,
in het openbaar te verdedigen
op vrijdag 25 april 2008 om 15.00 uur

door

**Wouter Dijkhuizen**

geboren op 21 april 1980
te Zevenaar

Dit proefschrift is goedgekeurd door de promotor

**Prof. dr. ir. J.A.M. Kuipers**

en de assistent promotor

**Dr. ir. M. van Sint Annaland**

“Ex nihilo nihil fit”

De Rerum Natura
Titus Lucretius Carus (ca. 99-55 B.C.)

Aan mijn ouders

# Table of contents

# Summary

CFD modeling of dispersed multiphase flows can be quite challenging because of the wide range of time- and length-scales involved. A modern methodology to bridge the different scales is multi-scale modeling, which involves applying different (types of) models to describe phenomena prevailing at different time and length scales. This approach requires however, closure equations for the unresolved sub-grid phenomena in the higher level models. These closures can in principle be obtained from analytical theory, experiments and direct numerical simulations (DNS), each with their own strong and weak points. Analytical theory is limited to idealized situations, for instance spherical bubbles in the limit of high Reynolds numbers, while experiments are time-consuming, costly and easily influenced by disturbances and contaminations and often not all relevant quantities can be measured simultaneously and with the desired accuracy. A third and relatively new path is to use DNS, which is not restricted to any idealized situation nor suffers from experimental difficulties. One of the strongest points is the freedom to change any of the physical properties or other parameters (geometry, operating parameters, etc.) at will and study their influence independently at great detail, having all the information on all variables (such as flow field, pressure field, etc.) available. The objective of this thesis was to improve a 3D Front Tracking model and to use it to obtain closures for the drag, lift and virtual mass forces acting on single bubbles rising in an initially quiescent infinite liquid. Using periodic boundary conditions, also the influence of neighboring bubbles (referred to as 'swarm effects') on the drag force was studied. In addition, dedicated experiments have been performed to validate the numerical results for the drag and lift forces acting on single bubbles.

To enable simulations over a wide range of bubble sizes and physical properties, first a 3D Front Tracking model has been improved with respect to volume conservation and parasitic currents. It was found that the cause of both these problems was related to the numerical treatment of the surface tension force and the pressure jump across the bubble interface, which was improved by directly accounting for the discontinuous pressure jump on the Lagrangian control points representing the bubble surface. This enabled the simulation of even very small bubbles (0.3 mm) in the notoriously difficult air-water system without numerical problems. To improve the performance of simulations for bubbles rising in very viscous liquids, the stress tensor in the Navier-Stokes equations has been discretized semi-implicitly, effectively removing the viscosity-stability time-step limitation. In addition, the model has been fully optimized for numerical efficiency, which, amongst other things, involved an improved implementation of the ICCG matrix solver. The end result is a numerical model that is capable of simulating bubbly flows with very different physical properties in weeks instead of months.

This improved model has been used to investigate the drag force acting on single bubbles rising in initially quiescent liquids, varying the dynamic viscosity of the continuous phase from that of a viscous glycerine/water mixture to the industrially important and numerically very challenging water case. It is well-known from literature that the drag force can be very sensitive to contaminations in the liquid and therefore a

combined numerical and experimental approach was followed. The numerical simulations, representing ultrapure liquids, agreed very well with experimental data from literature where ultrapure liquids were used, but showed a large difference with popular closures for deformed bubbles (derived from experimental data using lesser purified liquids), especially at lower liquid viscosities (i.e. water). Experiments, performed without purifying the liquids, have shown that the drag force is significantly higher than in the numerical simulations, most likely related to the added friction at the bubble surface.

A similar approach, using both experiments and numerical simulation, was used to study the lift force on a single rising bubble, by applying a linear shear field. It was found numerically (pure system) that there is a good agreement with the correlation proposed by Tomiyama et al. (2002) for deformed bubbles, which was derived from experimental data. For spherical bubbles the results agree better to the correlation by Legendre & Magnaudet (1998), which conform to the analytical solutions at both low and high Reynolds numbers. For the experimental validation a set-up has been constructed consisting of a running belt submerged in a column filled with liquid. The results show that – contrary to the simulations – the shear rate has a very pronounced effect on the sign and magnitude of the lift force coefficient.

Virtual mass, which is very important to accurately describe the bubble acceleration, was studied by releasing bubbles with different ellipsoidal shapes and orientation in an initially quiescent liquid. The numerical results show that neither the physical properties nor the equivalent bubble diameter have any influence on the virtual mass coefficient, although at higher gas/liquid density ratios more numerical resolution is required inside the bubbles to obtain a grid-independent solution. It was concluded that the virtual mass force only depends on the bubble shape and orientation and the numerical results show an excellent agreement with the analytical solution for the virtual mass force coefficient for prolate and oblate spheroids.

Finally, the modification of the drag force exerted on a bubble in a bubble swarm has been studied using the improved FT model with one or several bubbles positioned in a full periodic computational domain. For viscous liquids, the overall trend is an increase in the drag force coefficient as a function of the gas fraction (up to 15%), which corresponds to the hindrance effect. However, large bubbles first show a sharp decrease of the relative drag force with increasing gas fraction, before it starts to increase with the void fraction. A comparison between simulations with free-slip and periodic boundaries showed that this was caused by wake-acceleration effects in the periodic case, even though a relatively large computational domain was used. For air bubbles in water this wake-acceleration effect was not observed and for this case the drag force increase is smaller than for the viscous case. Moreover, it was concluded that for air bubbles in water, the extent of the swarm effect was not much affected by the bubble diameter.

# Samenvatting

CFD modellering van gedispergeerde meerfasen stromingen kan zeer uitdagend zijn, vanwege het brede spectrum aan betrokken tijd- en lengteschalen. Een moderne methodologie om de verschillende schalen te overbruggen is de multischaal aanpak, welke bestaat uit het toepassen van verschillende (types) modellen om de belangrijkste fenomenen te beschrijven op verschillende tijd en lengteschalen. Hiervoor zijn echter sluitingsrelaties vereist voor de niet-beschreven sub-grid verschijnselen in de hogere modellen. Deze sluitingsrelaties kunnen in principe verkregen worden vanuit analytische theorie, experimenten en directe numerieke simulaties (DNS), ieder met zijn eigen sterke en zwakke punten. Analytische theorie is beperkt tot geïdealiseerde situaties, bijvoorbeeld ronde bellen in de limiet van hoge Reynolds kentallen, terwijl experimenten veel tijd kosten, duur zijn en makkelijk worden beïnvloed door verstoringen en verontreinigingen en vaak niet alle relevante grootheden simultaan en met de gewenste nauwkeurigheid kunnen worden gemeten. Een derde en relatief nieuw pad is het gebruik van DNS, welke niet beperkt is tot geïdealiseerde situaties, noch lijdt onder de problemen van experimenten. Een van de sterke punten is de vrijheid om de fysische grootheden of andere parameters (geometrie, operationele grootheden, etc.) op elke moment te kunnen veranderen en om hun invloed onafhankelijk en in detail te kunnen bestuderen, aangezien alle informatie over alle variabelen (zoals het stromingsveld, drukveld, etc.) beschikbaar is. Het doel van dit proefschrift was om het 3D Front Tracking model te verbeteren en om dit te gebruiken om sluitingsrelaties af te leiden voor de wrijving-, lift- en virtuele massakrachten die werken op enkele bellen tijdens het opstijgen in een vloeistof die initieel in rust is. Door gebruik te maken van periodieke randvoorwaarden kan ook de invloed van naburige bellen (zwerm effecten) op de wrijvingskracht worden bestudeerd. Bovendien zijn er specialistische experimenten uitgevoerd om de bevindingen van de numerieke simulaties voor de wrijving- en liftkrachten werkend op een enkele bel te valideren.

Om simulaties over een breed gebied van bel groottes en fysische eigenschappen te kunnen uitvoeren, is eerst het 3D Front Tracking model verbeterd met het oog op volumebehoud en parasitaire stromingen. Er is geconcludeerd dat de oorzaak van beide problemen is gerelateerd aan de numerieke behandeling van de oppervlaktespanning en de druksprong over het beloppervlak, welke is verbeterd door de discontinue druksprong direct te verdisconteren op de Lagrangiaanse controle punten die het beloppervlak beschrijven. Dit maakt het mogelijk om zelfs hele kleine bellen (0.3 mm) in het notoir moeilijke lucht-water systeem te simuleren zonder numerieke problemen. Om de prestaties van de simulaties voor bellen die opstijgen in zeer viskeuze vloeistoffen te verbeteren is de spanningstensor in de Navier-Stokes vergelijkingen semi-impliciet gediscretiseerd, waardoor effectief de viscositeits-stabiliteits beperking wordt weggenomen. Bovendien is het model volledig geoptimaliseerd voor numerieke efficiëntie, welke onder andere een verbeterde implementatie van de ICCG algoritme behelste. Het eindresultaat is een numeriek model dat in staat is om stromingen met bellen en zeer uiteenlopende fysische eigenschappen te simuleren in weken in plaats van maanden.

Dit verbeterde model is gebruikt om de wrijvingskracht op een enkele bel stijgend in een initieel stilstaande vloeistof te onderzoeken, waarbij de dynamische viscositeit van de continue fase is gevarieerd van die van een viskeus glycerine/water mengsel tot die van de industrieel belangrijke en numeriek gecompliceerde situatie van water. Het is bekend vanuit de literatuur dat de wrijvingskracht zeer gevoelig is voor verontreinigingen in de vloeistof en daarom is een gecombineerde numerieke en experimentele aanpak gevolgd. De numerieke simulaties, welke ultrazuivere vloeistoffen vertegenwoordigen, komen zeer goed overeen met de experimentele data uit de literatuur waar ultrazuivere vloeistoffen zijn gebruikt, maar vertonen een groot verschil met veelgebruikte sluitingsrelaties voor vervormde bellen (afgeleid van experimenten met minder zuivere vloeistoffen), vooral bij lagere viskositeiten (bv. water). Experimenten, uitgevoerd zonder de vloeistoffen te zuiveren, laten zien dat de wrijvingskracht significant hoger is dan in de numerieke simulaties, wat waarschijnlijk veroorzaakt wordt door de hogere wrijving aan het beloppervlak.
Een vergelijkbare aanpak, met zowel experimenten en numerieke simulaties, is gebruikt om de liftkracht te bestuderen, door middel van het aanbrengen van een lineair afschuifspanningsveld. Een goede overeenkomst is gevonden tussen de numerieke simulaties (zuivere vloeistof) en de correlatie die voorgesteld is door Tomiyama et al. (2002) voor vervormde bellen, die gebaseerd is op experimentele gegevens. Voor ronde bellen komen de resultaten beter overeen met de correlatie van Legendre & Magnaudet (1998), die in de limietsituaties overeenkomt met de analytische oplossingen voor zowel lage en hoge Reynolds kentallen. Voor de experimentele validatie is een opstelling gebruikt, bestaande uit een lopende band ondergedompeld in een kolom gevuld met vloeistof. De resultaten tonen aan dat – in tegenstelling tot de simulaties – de afschuifspanning een zeer duidelijk effect heeft op het teken en de grootte van de liftkracht coëfficiënt.
Virtuele massa, zeer belangrijk voor een nauwkeurige beschrijving van de acceleratie van een bel, is bestudeerd door het loslaten van bellen met verschillende ellipsoïdale vormen en oriëntaties in een vloeistof die initieel in rust verkeert. De numerieke resultaten tonen aan dat de fysische eigenschappen, noch de equivalente beldiameter invloed hebben op de virtuele massa coëfficiënt, maar dat bij hogere gas/vloeistof dichtheidsratio's meer numerieke resolutie in de bellen nodig is om tot een grid-onafhankelijke oplossing te komen. De conclusie luidt dat de virtuele massa kracht alleen afhankelijk is van de belvorm en oriëntatie en dat de numerieke resultaten uitstekend overeenkomen met de analytische oplossing voor de virtuele massa kracht voor prolate en oblate sferoïden.
Als laatste is de verandering van de wrijvingskracht voor een bel in een bellenzwerm bestudeerd, met behulp van het verbeterde FT model waarbij een of enkele bellen zijn geplaatst in een volledig periodiek domein. De dominante trend is dat voor viskeuze vloeistoffen er een toename is in de wrijvingscoëfficiënt als functie van de gasfractie (tot 15%), welke overeenkomt met het hinderingseffect. Echter, voor grote bellen treedt er eerst een scherpe daling van de relatieve wrijvingskracht op, voordat deze begint toe te nemen met de gasfractie. Een vergelijking tussen simulaties met 'free-slip' en periodieke randvoorwaarden laat zien dat dit wordt veroorzaakt door zog-acceleratie

effekten in het periodieke geval, zelfs als een relatief groot numeriek domein wordt gebruikt. Voor luchtbellen in water is dit zog-acceleratie effect niet gevonden en in dit geval is de toename in de wrijvingskracht lager dan voor viskeuze vloeistoffen. Bovendien is geconcludeerd dat voor luchtbellen in water de grootte van het zwermeffect niet erg afhankelijk is van de beldiameter.

# 1

# Introduction


## Abstract

This chapter gives an introduction into the concept of deriving closure equations using direct numerical simulation (DNS). While multiphase flows are widely encountered in industry, CFD modelling of these systems can be quite challenging because of the wide range of time- and length-scales of the prevailing phenomena. Therefore a multilevel modelling strategy is employed, which requires closures for the coarser grained models. These closures can be obtained from analytical theory, experiments and direct numerical simulations (DNS). Analytical theory is usually limited to idealized cases, while experiments tend to suffer from the effects of contaminations. Direct numerical simulations can be used to investigate and overcome these problems and furthermore have the advantage of being able to change physical properties and other parameters at will. In this work a 3D Front Tracking model has been improved to reduce volume loss and parasitic currents and it has been optimized so that simulations run in weeks instead of months. It is used to generate closures for the drag, lift and virtual mass forces acting on single bubbles in an infinite liquid. Also the effect of bubble swarms on the drag force is studied, using periodic boundary conditions.

## 1.1 Modelling of gas-liquid flows

Multiphase systems are widely encountered in industrial processes, involving a.o. metal casting, fuel synthesis (Fischer-Tropsch), slurry polymerization and oil processing. The hydrodynamics of these systems are not only influenced by the individual phases, but also by their complex interactions, which is why CFD-based modelling of these systems is a computational challenge. In order to resolve all different time- and length-scales, a multi-level modelling strategy is used (van Sint Annaland et al., 2003), based on three different models (Fig. 1.1).

At the lowest level, direct numerical simulations (DNS) are capable of predicting the bubble shape, as well as the flow field inside and outside the bubble based solely on the Navier-Stokes and continuity equations. The results can be used to obtain closures for the forces acting on a single or a few bubbles or droplets, such as the drag, lift and virtual mass forces.
One level higher, the discrete bubble model (DBM) is capable of handling a large number of bubbles ($<O(10^6)$), at the expense of information about the bubble shape and detailed flow field around the individual bubbles. Therefore, this information has to be supplied in the form of closures for the forces acting on the bubbles, which also implicitly contains the bubble shape.
Industrial systems are mainly modelled using an Euler-Euler approach, which does not even discriminate between individual bubbles on a sub-grid scale. However, the same closures can be used as for the DBM, supplemented by a bubble population balances. Because of the number of additional equations required by the higher level models, their results depend crucially on the quality of these closures.

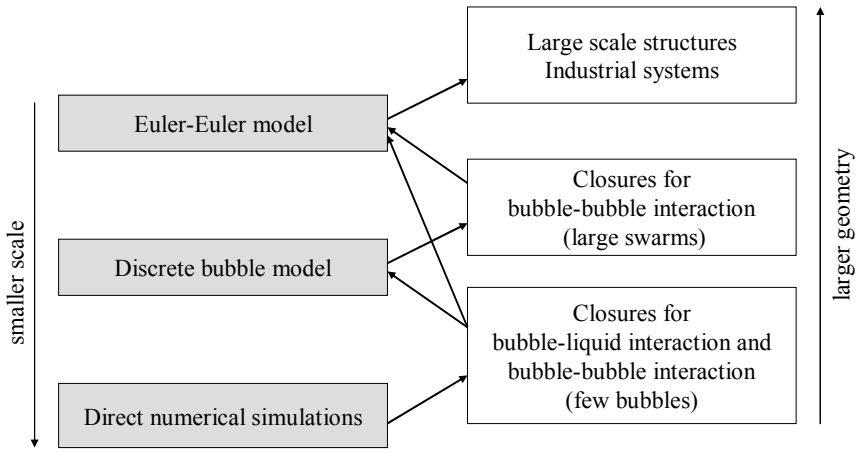


**Figure 1.1:** Multi-level modelling strategy for gas-liquid flows.

## 1.2 Interfacial closures

Closures for forces acting on dispersed elements can be obtained from analytical theory, dedicated experiments and DNS, each with their own strong and weak points. Analytical theory is often limited to idealized situations, for instance spherical bubbles in viscous liquids, which differ largely from industrially relevant cases, where bubbles are usually deformed and the flow pattern can be very dynamic. Nevertheless, analytical theory is invaluable when it comes to validation of experiments and numerical simulations.

On the other hand experiments often suffer from contaminants (Clift et al., 1976), which increase the drag force by changing the slip condition at the surface from no-shear to no-slip (Fig. 1.2). Secondly, a gradient in the concentration of contaminants on the bubble surface can create a Marangoni convection pattern opposing to the direction of motion (Palaparthi et al., 2005). The difficulty for experiments lies in determination of how pure the system is, and how the physical properties are altered by a small amount of contaminants. In addition it may be very difficult to experimentally determine all the required information simultaneously and non-invasively, as for example for the drag force on a bubble in a bubble swarm.

DNS can be used to overcome the problems faced by analytical theory and experiments, since it is not limited to idealized systems and contaminants are not an issue, which however can also be regarded as a drawback. Moreover, it is very easy to change physical properties and other parameters, allowing for extensive parameter studies that are not practical by means of experiments.

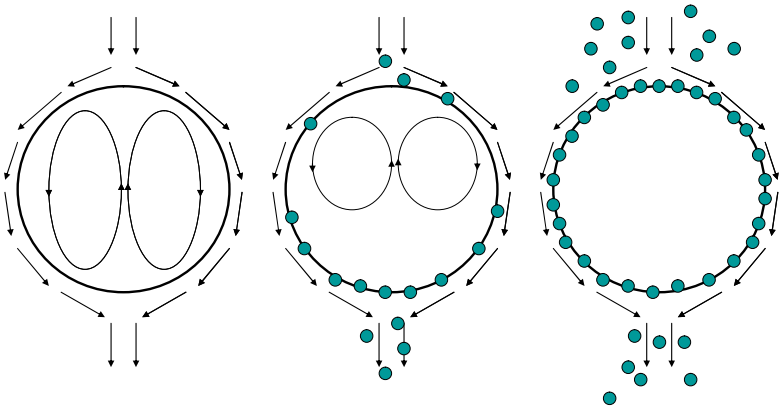

**Figure 1.2:** Schematic overview of the effect of contaminants on the drag force. From left to right: ultrapure liquid with no-shear boundary condition at the bubble interface; slightly contaminated liquid with a limited circulation inside the bubble; fully contaminated bubble, without any circulation (full no-slip boundary).

## 1.3 Direct numerical simulations

There are many different DNS models available in literature for multiphase flows with deformable interfaces, of which the strong and weak points are given in Table 1.1. For a more thorough overview the interested reader is referred to van Sint Annaland et al.

(2006). The main difference between these models is in the description of the phase boundaries: while the Volume of Fluid (VOF) and Lattice Boltzmann (LB) models both capture the interface using data from the fixed grid, the Front Tracking (FT) model tracks the interface explicitly using a Lagrangian surface mesh. As a consequence, the LB and VOF models exhibit automatic - potentially unphysical - coalescence when two bubbles meet, since the model cannot tell them apart. On the other hand the FT model needs a sub grid model to allow bubbles to merge (Singh & Shyy, 2007). This difference makes FT uniquely qualified for studying bubble-bubble interactions. Secondly, the superior interface resolution of the FT model is potentially more accurate in the description of surface tension forces. Of course FT also has some drawbacks, most notably the fact that the volume of the dispersed phases is not intrinsically conserved. Also the need for restructuring of the front is generally regarded as a drawback in literature.

**Table 1.1:** Overview of different DNS techniques for multiphase flows (van Sint Annaland et al., 2006).

| Method | Advantages | Disadvantages |
|---|---|---|
| Level set | Conceptually simple<br>Easy to implement | Limited accuracy<br>Volume loss |
| Shock-capturing | Straightforward implementation<br>Abundance of advection schemes available | Numerical diffusion<br>Fine grids required<br>Limited to small discontinuities |
| Marker particle | Extremely accurate<br>Robust<br>Accounts for substantial topology changes in the interface | Computationally expensive<br>Redistribution of marker particles required |
| SLIC VOF | Conceptually simple<br>Straightforward extension to 3D | Numerical diffusion<br>Limited accuracy<br>Artificial coalescence and break-up |
| PLIC VOF | Relatively simple<br>Accurate<br>Accounts for substantial topology changes in the interface | Artificial coalescence and break-up |
| Lattice Boltzmann | Accurate<br>Accounts for substantial topology changes in the interface | Difficult to implement<br>Artificial coalescence and break-up |
| Front Tracking | Extremely accurate<br>Robust<br>Accounts for substantial topology changes in the interface<br>No automatic coalescence and break-up | Mapping between interface and Euler grid required<br>Dynamic remeshing required<br>Volume loss |

The main challenges for DNS are related to the treatment of the surface tension force, large density jumps at the interface and high Reynolds numbers, which can all be found in the important air/water system. A high surface tension force (small bubbles) causes unphysical velocity vectors (Fig. 1.3), which may lead to excessive volume loss or other instabilities. As an illustration, standard FT is unable to simulate a 1 mm air bubble in water, since it vanishes due to volume losses of the dispersed phase before it has reached its steady-state rise velocity. While other DNS models do conserve the bubble volume, they are usually plagued by even greater numerical stability problems, making it impossible to carry out these simulations. As a consequence Scardovelli and Zaleski (1999) and Zaleski (2005) concluded that there is no three-dimensional calculation of a falling drop or rising bubble in the difficult air/water conditions.

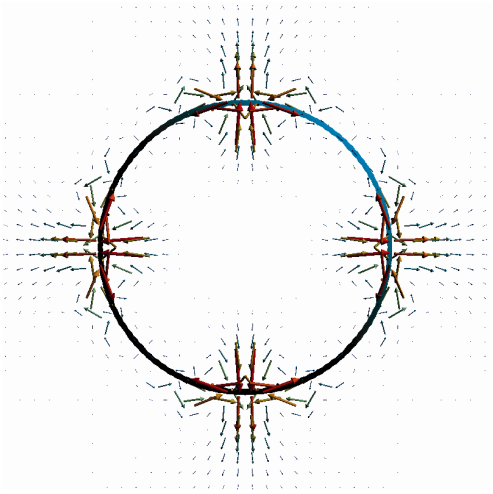

**Figure 1.3:** Spurious currents around the cross-section of a stationary 1 mm air bubble in water (zero gravity) using a standard first order pressure treatment in the momentum balance. These unphysical velocity vectors (~ $10^{-4}$ m/s) are caused by the mismatch between the surface tension force and pressure jump at the bubble interface.

## 1.4 Objectives

The objectives of this study are to further develop and use the 3D Front Tracking model to obtain better closures for interface forces, which can subsequently improve the results of DBM and Euler-Euler simulations following the multi-scale methodology. The focus is on the drag, lift and virtual mass forces acting on single bubbles and the effect of bubble swarms on the drag force. For validation, the drag and lift forces have also been studied using dedicated experiments.

In Chapter 2, a 3D Front Tracking model is improved with respect to volume conservation and parasitic currents, so that even small bubbles with very high surface tension forces can be studied without numerical problems. Semi-implicit treatment of the stress tensor in the Navier-Stokes equations is implemented, so that the viscosity-stability criterion is no longer limiting the time-step of the simulations. Finally, the

model will be optimized for numerical efficiency, to allow large numbers of simulations to run in weeks instead of months.

Chapter 3 focuses on the drag force exerted on a single bubble rising in an initially quiescent liquid. Numerical simulations are carried out across a wide range of physical properties of the continuous phase and bubble sizes to obtain a new closure for the drag force for bubbles, valid for ultrapure liquids. In addition experiments have been carried out to validate this closure and examine the effect of contaminants.

Chapter 4 treats the lift force, which is studied using a linear shear field. Again, numerical simulations are used to obtain results valid for ultrapure liquids, while with experiments the effect of contaminations on the lift force is elucidated.

The virtual or added mass force is studied in Chapter 5, by studying accelerating bubbles of different shapes in an initially quiescent liquid. The numerical results are then compared to the analytical solution for ellipsoidal bubbles.

Finally, Chapter 6 focuses on the so-called swarm effect on the drag force, which is defined as the modification of the drag force exerted on a bubble due to the presence of neighbouring bubbles, when increasing the gas fraction. Simulations have been carried out using single and multiple air bubbles in a full periodic domain and the results are compared to the drag force coefficient of a single bubble in an infinite liquid.

## References

1. R. Clift, J.R. Grace and M.E. Weber, Bubble, drops and particles, Academic Press, New York (1978).
2. R. Palaparthi, D.T. Papageorgiou and C. Maldarelli, Theory and experiments on the stagnant cap regime in the motion of spherical surfactant-laden bubbles, *J. Fl. Mech.* **559** (2006), 1-44.
3. R. Singh and W. Shyy, Three-dimensional adaptive Cartesian grid method with conservative, interface restructuring and reconstruction, *J. Comp. Ph.* **224** (2007), 150-167.
4. M. van Sint Annaland, N.G. Deen and J.A.M. Kuipers, Multi-level modeling of dispersed gas-liquid two-phase flows, series: Heat and mass transfer (eds. M. Sommerfeld and D. Mewes), Springer, Berlin (2003).
5. M. van Sint Annaland, W. Dijkhuizen, N.G. Deen and J.A.M. Kuipers, Numerical simulation of gas bubbles behaviour using a 3D front tracking method, *AIChE J.* **52** (2006), 99.
6. R. Scardovelli and S. Zaleski, Direct numerical simulation of free-surface and interfacial flow, *Annu. Rev. Fluid Mech.*, **31** (1999), 567.
7. A. Tomiyama, H. Tamai, I. Zun and S. Hosokawa, Transverse migration of single bubbles in simple shear flows, *Chem. Eng. Sci.* **57** (2002), 1849-1858.
8. S. Zaleski, Interface Tracking – VOF, VKI lecture series, Von Karman Institute for Fluid Mechanics, Belgium (2005).

# 2

# Front Tracking model


## Abstract

In this chapter, an improved 3D Front Tracking model is described, which is used to obtain a-priori closures for the interfacial forces in bubbly flows. Dedicated test-cases are used to assess the accuracy of the numerical results using analytical solutions and the performance is compared to other Front Tracking models reported in the literature. Moreover, benchmarks are used to find the optimal computational settings. From literature it is well-known that this type of model is often plagued by spurious currents and volume conservation issues. Therefore, several improvements have been made to enable the simulation of even very small bubbles or droplets with very high surface tension forces. First of all, a new method to account for the pressure jump at the bubble interface is implemented, which reduces the magnitude of the spurious currents by two orders of magnitude. Secondly, in order to further improve volume conservation and interface smoothness, the numerical implementation of the advection of the interface has been upgraded with higher order interpolation and time-stepping methods.

Besides numerical stability and accuracy, another focus was on speeding up the calculations, in order to enable parameter studies consisting of hundreds of simulations. The time-step constraint for viscous liquids has been overcome by using a semi-implicit treatment of the viscous stress tensor in the Navier-Stokes equations. Finally, the ICCG matrix solver has been optimized, since it is responsible for more than 90% of the total computation time. The structure of the matrix equations has been exploited in order to obtain a speed-up of a factor of 2 to 4. Benchmarking of the optimized ICCG matrix solver has revealed that for modern computers at full load, the performance is not limited by CPU, but rather by memory performance.

## 2.1 Introduction

Multiphase systems are widely encountered in industrial processes, involving a.o. metal casting, fuel synthesis (Fischer-Tropsch), slurry polymerization and oil processing. Their hydrodynamics are not only dictated by the individual phases, but especially by complex interactions between the phases, making CFD-based modelling a computational challenge. Industrial systems are mainly modelled using a Eulerian approach, which does not discriminate individual bubbles, droplets or particles on a sub-grid scale. Therefore, closure equations are required for the interfacial forces (viz. drag, lift and virtual mass) and sub-grid-scale turbulence, which can in principle be derived from direct numerical simulations (DNS).

The main challenges for DNS are in the treatment of the surface tension force, large density jumps and high Reynolds numbers, which are all encountered in the important air/water system. To illustrate the current state of the art, Scardovelli and Zaleski (1999) and Zaleski (2005) claim that there is no three-dimensional calculation of a falling drop or rising bubble for the difficult air/water conditions.

Compared to other DNS techniques, Front Tracking (FT; Unverdi and Tryggvason, 1992) offers a more accurate surface tension treatment, because of the sub-grid interface resolution. In addition, the explicit interface tracking allows to prevent unphysical coalescence of bubbles, which is particularly important when studying bubble swarms. However, FT also has some drawbacks, most notably the fact that the volume conservation of the dispersed phases is not intrinsically enforced. Also, the need for restructuring of the front is generally regarded as a drawback in literature.

In this work a standard 3D FT model (van Sint Annaland et al., 2006) has been improved, to allow the simulation of even very small bubbles, with very high surface tension forces, without numerical problems. Secondly, the computational costs have been reduced, to enable large numbers of simulations necessary to derive closures for interface forces. More specifically, the following has been improved:

- Direct coupling between the surface tension force and the pressure jump at the interface, to reduce the magnitude of spurious currents while maintaining a sharp interface representation.
- Direct calculation of the phase fractions from the interface triangulation, eliminating the standard, but computationally expensive and diffusive method proposed by Unverdi & Tryggvason (1992).
- Higher order advection of the interface, to reduce volume conservation errors and improve interface smoothness.
- Semi-implicit treatment of the stress tensor, avoiding time-step limitations for highly viscous flows.
- Custom-made ICCG matrix solver, to reduce the calculation time.

In the following paragraph a general description of the model is given, with the improvements worked out in more detail. Subsequently, the improved model will be validated and benchmarked using a collection of dedicated test cases.

## 2.2 Model formulation

### 2.2.1 General overview

The model is based on the incompressible Navier-Stokes equations, with a singular source-term $\mathbf{F}_\sigma$ for the surface tension force at the interface:

$$\rho \frac{\partial \mathbf{u}}{\partial t} = -\nabla p - \rho \nabla \cdot (\mathbf{u}\mathbf{u}) - \nabla \cdot \boldsymbol{\tau} + \rho \mathbf{g} + \mathbf{F}_\sigma \tag{2.1}$$

where $\mathbf{u}$ is the velocity field, $\boldsymbol{\tau}$ the stress tensor and $p$ the pressure field. Mass conservation is enforced by the incompressible continuity equation:

$$\nabla \cdot \mathbf{u} = 0 \tag{2.2}$$

Since the velocity field is continuous even across interfaces for pure gases and liquids, a one-field formulation can be used to describe all phases at once. However, the shear stress and pressure are not continuous across the interface and the usual jump condition is given by Eq. 2.3. The physical properties (viz. density $\rho$ and dynamic viscosity $\eta$) now change discontinuously across the interface, indicated by a Heaviside function $H_i$ which is equal to one inside fluid $i$ and zero everywhere else (Eq. 2.4).

$$\left[-p - \boldsymbol{\tau}\right] \cdot \mathbf{n} = \mathbf{F}_\sigma \cdot \mathbf{n} \tag{2.3}$$

$$\begin{aligned} \rho &= \sum_{i=1}^{N_{ph}} H_i(\mathbf{x}) \rho_i \\ \eta &= \sum_{i=1}^{N_{ph}} H_i(\mathbf{x}) \eta_i \end{aligned} \tag{2.4}$$

The interface is represented (parameterized) by an unstructured grid (triangulation) with the Lagrangian (control) points co-moving with the fluid. For each time step the following procedure is carried out: first, the Navier-Stokes equations together with the continuity equation are solved with a fractional step projection method to obtain the flow field. Then, the front (interface) is moved to its new location, using locally interpolated velocities, after which the surface grid is restructured (if necessary) and the physical properties are updated (see Fig. 2.1).

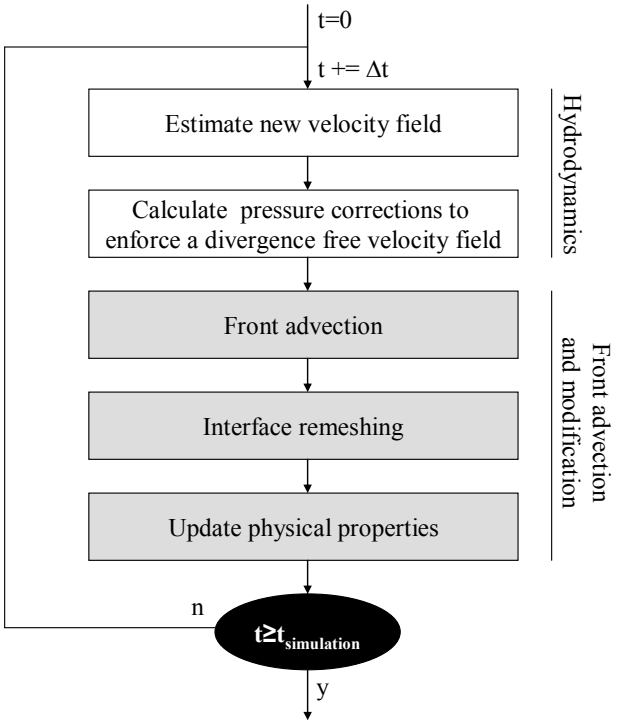


**Figure 2.1:** Order of operations in the 3D Front Tracking model.

## 2.2.2 Discretised Navier-Stokes equations

The system of equations is solved on a Cartesian staggered grid, using a fractional step method. First of all, an explicit estimate of the velocity $\mathbf{u}^{n*}$ is calculated, using information from the previous time step (indicated with the superscript $n$):

$$\mathbf{u}^{n*} = \mathbf{u}^{n} + \frac{\Delta t}{\rho}\left[-\nabla p - \nabla \cdot \mathbf{u}\mathbf{u} - \nabla \cdot \boldsymbol{\tau} + \rho \mathbf{g} + \mathbf{F}_{\sigma}\right]^{n} \tag{2.5}$$

The convective term is discretised with a second order flux-delimited Barton scheme (Centrella & Wilson, 1984) and the diffusion term with a second order central scheme. For highly viscous systems at small length scales, the time-step $\Delta t$ can be limited by the stability of the explicit treatment of the diffusion terms, which is cured by treating part of the diffusion terms implicitly (following Uhlmann, 2005). Therefore, the stress tensor is split into an implicit part ($\boldsymbol{\tau}^{n**}$), with all the derivatives containing the velocity component in one direction, and an explicit part ($\boldsymbol{\tau}^{n}$) containing the other velocity components (e.g. $\mathbf{u}_y$ and $\mathbf{u}_z$ when solving for $\mathbf{u}_x$):

$$\boldsymbol{\tau} = \boldsymbol{\tau}^{n} + \boldsymbol{\tau}^{n^{**}} = \begin{bmatrix} -2\eta \dfrac{\partial u_x^{n^{**}}}{\partial x} & -\eta\left(\dfrac{\partial u_y^{n^{**}}}{\partial x} + \dfrac{\partial u_x^{n}}{\partial y}\right) & -\eta\left(\dfrac{\partial u_z^{n^{**}}}{\partial x} + \dfrac{\partial u_x^{n}}{\partial z}\right) \\ -\eta\left(\dfrac{\partial u_x^{n^{**}}}{\partial y} + \dfrac{\partial u_y^{n}}{\partial x}\right) & -2\eta \dfrac{\partial u_y^{n^{**}}}{\partial y} & -\eta\left(\dfrac{\partial u_z^{n^{**}}}{\partial y} + \dfrac{\partial u_y^{n}}{\partial z}\right) \\ -\eta\left(\dfrac{\partial u_x^{n^{**}}}{\partial z} + \dfrac{\partial u_z^{n}}{\partial x}\right) & -\eta\left(\dfrac{\partial u_y^{n^{**}}}{\partial z} + \dfrac{\partial u_z^{n}}{\partial y}\right) & -2\eta \dfrac{\partial u_z^{n^{**}}}{\partial z} \end{bmatrix} \tag{2.6}$$

Note that as a result of this partial implicit treatment, the stress tensor has lost its diagonal symmetry (i.e. $\boldsymbol{\tau}_{zx} \neq \boldsymbol{\tau}_{xz}$). These implicit terms have been chosen such that each velocity component can be solved separately and the remaining explicit terms are relatively small. For each velocity component this discretisation results in a seven-point stencil (Eq. 2.7) and the three independent systems of linear equations (one for each velocity component) are solved sequentially using an ICCG matrix solver.

$$u_x^{n^{**}} = u_x^{n^{*}} - \frac{\Delta t}{\rho}\left[ -\frac{\partial}{\partial x}\left(2\eta \frac{\partial u_x^{n^{**}}}{\partial x}\right) - \frac{\partial}{\partial y}\left(\eta \frac{\partial u_x^{n^{**}}}{\partial y}\right) - \frac{\partial}{\partial z}\left(\eta \frac{\partial u_x^{n^{**}}}{\partial z}\right)\right] \tag{2.7}$$

$$u_{x,i+\frac{1}{2},j,k}^{n^{**}} = u_{x,i+\frac{1}{2},j,k}^{n^{*}} + \frac{\Delta t}{\rho_{i+\frac{1}{2},j,k}}\left[ 2\eta_{i+1,j,k} \frac{u_{x,i+\frac{3}{2},j,k}^{n^{**}} - u_{x,i+\frac{1}{2},j,k}^{n^{**}}}{\Delta x^2} - 2\eta_{i,j,k} \frac{u_{x,i+\frac{1}{2},j,k}^{n^{**}} - u_{x,i-\frac{1}{2},j,k}^{n^{**}}}{\Delta x^2} + \right.$$
$$\eta_{i+\frac{1}{2},j+\frac{1}{2},k} \frac{u_{x,i+\frac{1}{2},j+1,k}^{n^{**}} - u_{x,i+\frac{1}{2},j,k}^{n^{**}}}{\Delta x \Delta y} - \eta_{i+\frac{1}{2},j-\frac{1}{2},k} \frac{u_{x,i+\frac{1}{2},j,k}^{n^{**}} - u_{x,i+\frac{1}{2},j-1,k}^{n^{**}}}{\Delta x \Delta y} +$$
$$\left. \eta_{i+\frac{1}{2},j,k+\frac{1}{2}} \frac{u_{x,i+\frac{1}{2},j,k+1}^{n^{**}} - u_{x,i+\frac{1}{2},j,k}^{n^{**}}}{\Delta x \Delta z} - \eta_{i+\frac{1}{2},j,k-\frac{1}{2}} \frac{u_{x,i+\frac{1}{2},j,k}^{n^{**}} - u_{x,i+\frac{1}{2},j,k-1}^{n^{**}}}{\Delta x \Delta z} \right]$$

All the forces in the Navier-Stokes equations have now been accounted for; however the continuity equation has not yet been satisfied, which can be accomplished via a standard pressure correction $\delta p$:

$$\begin{aligned} \delta p &\equiv p^{n+1} - p^{n} \\ \mathbf{u}^{n+1} &= \mathbf{u}^{n^{**}} - \frac{\Delta t}{\rho} \nabla(\delta p) \end{aligned} \tag{2.8}$$

According to the continuity equation, the velocity field has to be divergence free, or in other words: the pressure correction has to cancel the divergence of the intermediate velocity:

$$\nabla \cdot \mathbf{u}^{n+1} = \nabla \cdot \mathbf{u}^{n**} - \nabla \cdot \left[ \frac{\Delta t}{\rho} \nabla (\delta p) \right] = 0$$
$$\nabla \cdot \left[ \frac{\Delta t}{\rho} \nabla (\delta p) \right] = \nabla \cdot \mathbf{u}^{n**} \tag{2.9}$$

which leads to the following discretisation for a cell (i,j,k):

$$\begin{aligned}
&\left( \frac{\Delta t}{\Delta x \rho_{i+\frac{1}{2},j,k}} + \frac{\Delta t}{\Delta x \rho_{i-\frac{1}{2},j,k}} + \frac{\Delta t}{\Delta y \rho_{i,j+\frac{1}{2},k}} + \frac{\Delta t}{\Delta y \rho_{i,j-\frac{1}{2},k}} + \frac{\Delta t}{\Delta z \rho_{i,j,k+\frac{1}{2}}} + \frac{\Delta t}{\Delta z \rho_{i,j,k-\frac{1}{2}}} \right) \delta p_{i,j,k} \\
&- \frac{\Delta t \delta p_{i+1,j,k}}{\Delta x \rho_{i+\frac{1}{2},j,k}} - \frac{\Delta t \delta p_{i,j,k}}{\Delta x \rho_{i-\frac{1}{2},j,k}} - \frac{\Delta t \delta p_{i,j+1,k}}{\Delta y \rho_{i,j+\frac{1}{2},k}} - \frac{\Delta t \delta p_{i,j-1,k}}{\Delta y \rho_{i,j-\frac{1}{2},k}} - \frac{\Delta t \delta p_{i+1,j,k}}{\Delta z \rho_{i,j,k+\frac{1}{2}}} - \frac{\Delta t \delta p_{i,j,k-1}}{\Delta z \rho_{i,j,k-\frac{1}{2}}} \\
&= u^{n+\frac{1}{2}}_{x,i+\frac{1}{2},j,k} - u^{n+\frac{1}{2}}_{x,i-\frac{1}{2},j,k} + u^{n+\frac{1}{2}}_{y,i,j+\frac{1}{2},k} - u^{n+\frac{1}{2}}_{y,i,j-\frac{1}{2},k} + u^{n+\frac{1}{2}}_{z,i,j,k+\frac{1}{2}} - u^{n+\frac{1}{2}}_{z,i,j,k-\frac{1}{2}}
\end{aligned} \tag{2.10}$$

It can be seen that apart from the central pressure correction term, six neighbours are used, which leads to a matrix with seven diagonal bands. Moreover, it can be seen that the matrix is symmetric, since a pressure difference between two cells has the exact opposite effect on both cells. Periodic boundaries add six more bands to the matrix, since not only direct neighbours, but also cells across the domain have to be addressed.

### 2.2.3 Optimized ICCG matrix solver

From the discretised Navier-Stokes equations it follows that there are two kinds of matrix equations to be solved: first three matrix equations to obtain the velocities in three directions and finally a pressure correction equation. All of these cases consist of a symmetric sparse matrix with dimension $N_x * N_y * N_z$. Using regular boundary conditions the matrix has seven diagonals, while for full 3D periodic boundaries there are thirteen bands.

First of all, the symmetry of the matrices has been exploited by storing only the lower half and the diagonal (Fig. 2.2, left). This not only reduces the memory requirements to store the matrix by 40%, but also significantly lowers the required memory throughput. For the periodic case, the benefit is even greater, because it proves possible to store its thirteen bands in only four vectors (Fig. 2.2, right).

Secondly, it was found that the pressure correction matrix contains mostly identical terms, corresponding to the continuous phase (which has a fixed density). By properly scaling the entire matrix, these “liquid-phase” row-vectors can be omitted. More importantly, this allows the corresponding matrix-vector multiplications in the algorithm of the matrix solver to be replaced by a simple vector addition, which significantly boosts performance (Eq. 2.11). Note that the improvements to the matrix

solver have no impact on the simulation results whatsoever: the algorithm of the ICCG matrix solver is still essentially the same.

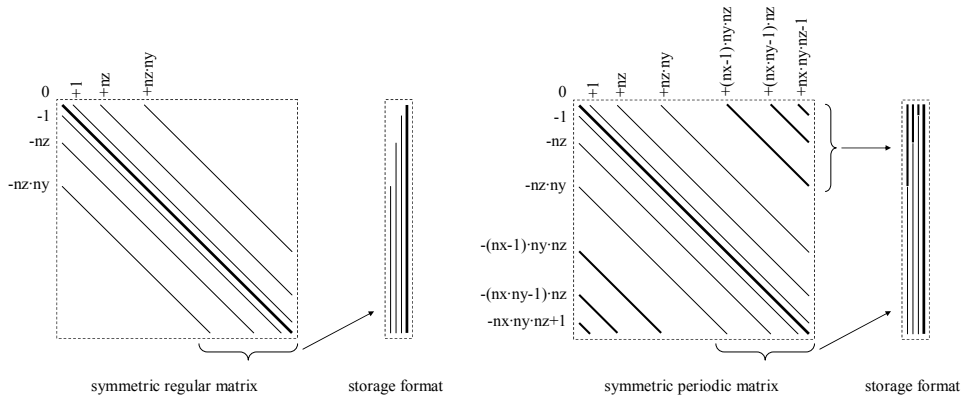


**Figure 2.2:** Conversion of the general matrix format to a highly efficient sparse banded symmetric storage. Only the lower four regular bands (left) and the top three periodic bands (right) are stored in a compact four-band format, which is efficient in terms of both memory usage and addressing.

$$\mathbf{Ax} = \left( \sum_{j=1..N} a_{1,j}x_j, \sum_{j=1..N} a_{2,j}x_j, \cdots, \sum_{j=1..N} a_{N,j}x_j \right)$$

$$\Delta x = \Delta y = \Delta z \quad \& \quad \rho_{i+\frac{1}{2},j,k} = \rho_{i-\frac{1}{2},j,k} = \rho_{i,j+\frac{1}{2},k} = \rho_{i,j-\frac{1}{2},k} = \rho_{i,j,k+\frac{1}{2}} = \rho_{i,j,k-\frac{1}{2}} \Rightarrow \tag{2.11}$$

$$\left[ \sum_{j=1..N} a_{i,j}x_j \right]_{continuous} = \frac{\Delta t}{\Delta x^2 \rho_l} \left( -x_{j-nz*ny} - x_{j-nz} - x_{j-1} + 6x_j - x_{j+1} - x_{j+nz} - x_{j+nz*ny} \right)$$

## 2.2.4 Surface tension force

One of the most widespread surface tension models for FT is based on the idea of pull-forces, which are computed directly from the markers representing the interface. The individual pull-force of marker $a$ acting on marker $m$ can be computed from their normal vectors and joint tangent:

$$\mathbf{F}_{\sigma,a\to m} = \sigma \left( \mathbf{t}_{ma} \times \mathbf{n}_a \right) \tag{2.12}$$

There is however a subtle difference in the way the total force on a marker is calculated by different research groups (see Fig. 2.3). Shin & Juric (2002) first compute the net inwards pointing force on each tangent, which is defined as the sum of two pull forces. These inward pointing forces are then distributed equally to both adjacent markers, leading to the following force on marker m:

$$\mathbf{F}_{\sigma,m} = \sum_{i} \mathbf{F}_{inward,i} = \sum_{i=a,b,c} \frac{\mathbf{F}_{\sigma,m\to i} + \mathbf{F}_{\sigma,i\to m}}{2} \tag{2.13}$$

Alternatively, the sum of the pull-forces acting on the marker can be taken (Deen et al., 2004), which can be shown to give exactly the same solution since the inward directed forces cancel each other out (Eq. 2.14). Since this variation is much simpler and requires only half the computational work, it is be used in this work. According to Tryggvason (2001) this direct approach avoids the complicated and not very accurate polynomial interpolation of the surface in 3D. As a consequence complicated error-suppressing algorithms such as described by Singh and Shyy (2006) are also avoided. Finally, the total net surface tension force is automatically zero for a closed surface.

$$\mathbf{F}_{\sigma,m} = \frac{1}{2}\left( \sum_{i=a,b,c} \mathbf{F}_{\sigma,m\to i} + \sum_{i=a,b,c} \mathbf{F}_{\sigma,i\to m} \right) = \frac{1}{2} \sum_{i=a,b,c} \mathbf{F}_{\sigma,i\to m} \tag{2.14}$$

When the force on a marker has been calculated, a mass-weighing distribution function (Deen et al., 2004) is used to map the total force to the surrounding cells based on their density:

$$\begin{aligned}
\left(\mathbf{F}_{\sigma}\right)_{i,j,k} &= \frac{\sum_{m} \rho_{i,j,k} D\left(\mathbf{x}_{i,j,k} - \mathbf{x}_{m}\right) \mathbf{F}_{\sigma,m}}{\sum_{m} \rho_{i,j,k} D\left(\mathbf{x}_{i,j,k} - \mathbf{x}_{m}\right)} \\
D(\mathbf{r}) &= d_x(r_x)\, d_y(r_y)\, d_z(r_z) \\
d_x(r_x) &= \begin{cases} 1 - \dfrac{|r_x|}{h} & |r_x| \le h \\ 0 & |r_x| > h \end{cases}
\end{aligned} \tag{2.15}$$

The physical background of this mass-weighing function is based on the continuity of velocity at the interface: a force which acts equally on the gas and on the liquid phase must yield the same velocity at the interface. Therefore the momentum should be balanced based on the density in the different cells, which reduces the magnitude of the spurious currents considerably and thus makes it possible to simulate systems with very high density ratios of $O(10^4)$ without any numerical problems.
Other FT models described in literature typically alleviate this problem by smearing out the surface tension forces over a large stencil using e.g. a Peskin-like function (Tryggvason et al., 2001; Shin & Juric, 2002). Also they have a diffuse density gradient over several cells at the interface, as a result of the way the phase fractions are calculated (see §2.2.7). This may allow them to simulate systems with moderately high

surface tension forces or high density ratios, but at the cost of a sharp interface representation.

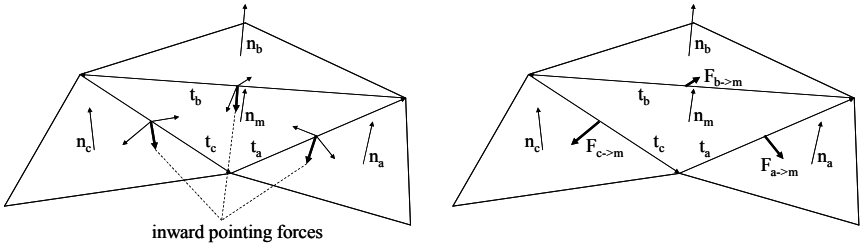


**Figure 2.3:** Surface tension forces acting on a triangular marker. Shin & Juric (2002) use the net inwards pointing forces on each of the tangents (left), while Deen et al. (2004) use the pull-forces on the marker (right). It was shown that both methods are identical, since the pull-forces in the plane of marker m cancel each other out.

## 2.2.5 Interfacial pressure jump

The coupling between surface tension forces and the pressure jump at the interface is crucially important to prevent unphysical spurious currents, as was demonstrated by Popinet and Zaleski (1999) using a 2D Front Tracking model. They used a large computational stencil (3x3 nodes) to accurately capture the pressure jump at the interface. However, this is not feasible in 3D, due to the resulting computationally prohibitive 27-band pressure matrix. Moreover, it is important to understand that interfacial tension creates a pressure discontinuity at the position of the front, which is not easily accounted for in a Eulerian framework, even with higher order discretisations.

The magnitude of the pressure jump related to the surface tension force can easily be calculated from the jump condition (Eq. 2.3), when the shear stress in the normal direction is neglected (Eq. 2.16). This makes it possible to separate the pressure inside the dispersed phases into a continuous (dynamic) part and a discontinuous pressure jump, which can be mapped to the Euler grid in the same way as the surface tension force. The main advantage is that now both the surface tension force and the pressure jump act at exactly the same location, which means that only a relatively small net force will be transmitted to the Euler grid. This is much more accurate than a purely Eulerian treatment of the pressure discontinuity, thereby leading to much lower spurious currents and improved numerical stability. All of this is realized with hardly any additional computational cost, because the surface tension force has already been calculated.

$$\int_{\partial S} [p] dS = \int_{\partial S} \mathbf{F}_\sigma \cdot \mathbf{n}$$

$$[p] = \frac{\int_{\partial S} \mathbf{F}_\sigma \cdot \mathbf{n}}{\int_{\partial S} dS} = \frac{\sum_m \mathbf{F}_{\sigma,m} \cdot \mathbf{n}_m}{\sum_m S_m} \tag{2.16}$$

### 2.2.6 Surface advection

Sousa et al. (2004) mention that when the Reynolds number is high (>50) small undulations may appear at the interface, which are "due to variations in the velocity field from cell to cell." The solution they present in their article is a filter to suppress these undulations. Instead of using a filter, in this work the focus is on tackling the cause of the disturbances, which is found to be primarily dominated by the advection of the surface grid.

Most Front Tracking models in literature utilize a first order velocity interpolation. The problem with this type of interpolation is that it is piecewise linear, not providing a smooth transition between nodes. As a result the first order interpolation produces an imprint of the Euler grid on the bubble (Fig. 2.4, left). To keep the surface smooth, a higher order velocity interpolation is needed, for which a third order spline is a good candidate since it guarantees a smooth interpolation and thus the bubble surface will stay smooth (Fig. 2.4, right). The spline is independent for each velocity component in every direction, because at the nodal points the interpolation matches the interpolated values exactly. Between every two velocity nodes the local interpolation polynomial becomes:

$$s_{x,i}(x,y,z)=\sum_{a=0}^{1}\sum_{b=0}^{1}\sum_{c=0}^{1}d_{x,a}d_{y,b}d_{z,c}\begin{bmatrix}u_{x,i+a,j+b,k+c}+\left(d_{x,a}^{2}-1\right)M_{x,i+a,j+b,k+c}+\\ \left(d_{y,b}^{2}-1\right)M_{y,i+a,j+b,k+c}+\left(d_{z,c}^{2}-1\right)M_{z,i+a,j+b,k+c}\end{bmatrix} \tag{2.17}$$

$$\begin{aligned} d_{x,0}&=\frac{x_{i+1}-x}{\Delta x} & d_{y,0}&=\frac{y_{i+1}-y}{\Delta y} & d_{z,0}&=\frac{z_{k+1}-z}{\Delta z}\\ d_{x,1}&=\frac{x-x_i}{\Delta x}=1-d_{x,0} & d_{y,1}&=\frac{y-y_i}{\Delta y}=1-d_{y,0} & d_{z,1}&=\frac{z-z_k}{\Delta z}=1-d_{z,0}\end{aligned} \tag{2.18}$$

where $M_{x,i,j,k}$ represents the second derivative in the x-direction at the node $(i,j,k)$. To find their values the spline can be separated in its x-, y- and z-direction. For the x-direction the local polynomial and its derivatives then become:

$$\begin{aligned} s_{x,i}(x)&=d_{x,0}u_{x,i,j,k}+d_{x,1}u_{x,i+1,j,k}+\left(d_{x,0}^{3}-d_{x,0}\right)\Delta x^{2}M_{x,i}+\left(d_{x,1}^{3}-d_{x,1}\right)\Delta x^{2}M_{x,i+1}\\ s_{x,i}'(x)&=\frac{u_{x,i+1,j,k}-u_{x,i,j,k}}{\Delta x}-\left(3d_{x,0}^{2}-1\right)M_{x,i}+\left(3d_{x,1}^{2}-1\right)M_{x,i+1}\\ s_{x,i}''(x)&=6\left(d_{x,0}M_{x,i}+d_{x,1}M_{x,i+1}\right)\end{aligned} \tag{2.19}$$

It can be seen that the second derivative is interpolated linearly between the nodes, which satisfies continuity. Also the first derivative has to be continuous, requiring that:

$$
\begin{aligned}
& s_{x,i}'(x_i) = s_{x,i-1}'(x_i) \\
& \frac{u_{x,i+1,j,k} - u_{x,i,j,k}}{\Delta x} - 2M_{x,i} - M_{x,i+1} = \frac{u_{x,i,j,k} - u_{x,i-1,j,k}}{\Delta x} + M_{x,i-1} + 2M_{x,i} \\
& M_{x,i+1} + 4M_{x,i} + M_{x,i-1} = \frac{6}{\Delta x^2}\left(u_{x,i+1,j,k} - 2u_{x,i,j,k} + u_{x,i-1,j,k}\right)
\end{aligned}
\tag{2.20}
$$

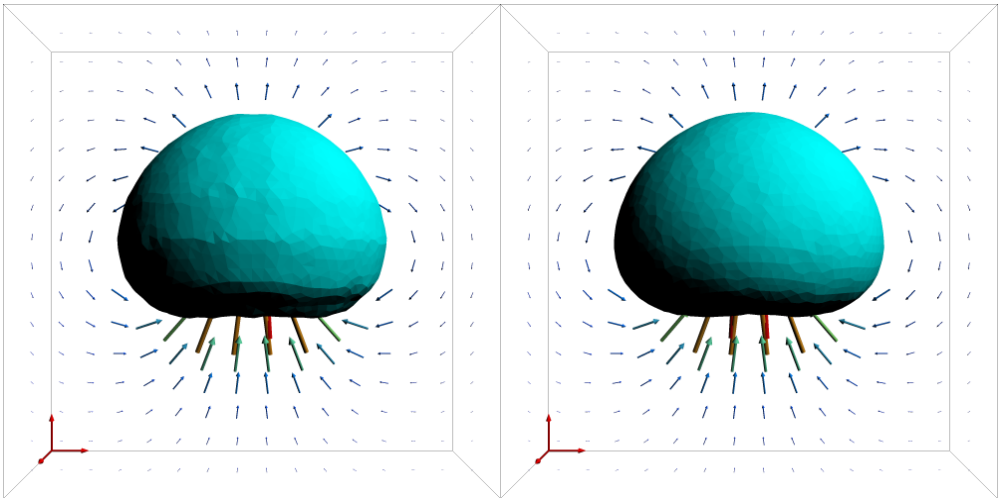

**Figure 2.4:** Qualitative effect of the velocity interpolation on the surface grid for a 2 mm air bubble in water. It can be seen that the first order velocity interpolation creates imprints on the surface grid (left), while the higher order interpolation gives a smooth result (right). All other settings are identical.

These equations are combined for the whole one-dimensional spline to obtain values for the second derivatives. Using parabolic boundary conditions ($M_1 = 2M_2 - M_3$) the system of equations becomes:

$$
\begin{bmatrix}
6 & 0 & 0 & \cdots & 0 & 0 & 0 \\
1 & 4 & 1 & \cdots & 0 & 0 & 0 \\
0 & 1 & 4 & \cdots & 0 & 0 & 0 \\
\vdots & \vdots & \vdots & \ddots & \vdots & \vdots & \vdots \\
0 & 0 & 0 & \cdots & 4 & 1 & 0 \\
0 & 0 & 0 & \cdots & 1 & 4 & 1 \\
0 & 0 & 0 & \cdots & 0 & 0 & 6
\end{bmatrix}
\cdot
\begin{bmatrix}
x_2 \\ x_3 \\ x_4 \\ \vdots \\ x_{n-3} \\ x_{n-2} \\ x_{n-1}
\end{bmatrix}
= \frac{6}{h^2}
\begin{bmatrix}
u_1 - 2u_2 + u_3 \\
u_2 - 2u_3 + u_4 \\
u_3 - 2u_4 + u_5 \\
\vdots \\
u_{n-4} - 2u_{n-3} + u_{n-2} \\
u_{n-3} - 2u_{n-2} + u_{n-1} \\
u_{n-2} - 2u_{n-1} + u_n
\end{bmatrix}
\tag{2.21}
$$

This matrix can be solved very efficiently in O(N) operations using a tridiagonal algorithm. In the case of periodic boundary conditions, two terms are added in the corners of the tridiagonal matrix:

$$\begin{bmatrix} 4 & 0 & 0 & \cdots & 0 & 0 & 1 \\ 1 & 4 & 1 & \cdots & 0 & 0 & 0 \\ 0 & 1 & 4 & \cdots & 0 & 0 & 0 \\ \vdots & \vdots & \vdots & \ddots & \vdots & \vdots & \vdots \\ 0 & 0 & 0 & \cdots & 4 & 1 & 0 \\ 0 & 0 & 0 & \cdots & 1 & 4 & 1 \\ 1 & 0 & 0 & \cdots & 0 & 0 & 4 \end{bmatrix} \cdot \begin{bmatrix} x_1 \\ x_2 \\ x_3 \\ \vdots \\ x_{n-2} \\ x_{n-1} \\ x_n \end{bmatrix} = \frac{6}{h^2} \begin{bmatrix} u_n - 2u_1 + u_2 \\ u_1 - 2u_2 + u_3 \\ u_2 - 2u_3 + u_4 \\ \vdots \\ u_{n-3} - 2u_{n-2} + u_{n-1} \\ u_{n-2} - 2u_{n-1} + u_n \\ u_{n-1} - 2u_n + u_1 \end{bmatrix} \tag{2.22}$$

When solving the periodic case, it is still desired to use the tridiagonal algorithm, because of its superior speed. This can be accomplished using the Sherman-Morrison formula, which handles the corner terms as two correction vectors:

$$\begin{aligned} &\left(\mathbf{A} + \mathbf{u} \otimes \mathbf{v}\right) \cdot \mathbf{x} = \mathbf{r} \\ &\mathbf{u} = \begin{bmatrix} -4 \\ 0 \\ \vdots \\ 0 \\ 1 \end{bmatrix}; \mathbf{v} = \begin{bmatrix} 1 \\ 0 \\ \vdots \\ 0 \\ -1/4 \end{bmatrix} \end{aligned} \tag{2.23}$$

This system can then be solved in two consecutive steps of the tridiagonal algorithm, after which the solution can be recombined from both solution vectors $\mathbf{y}$ and $\mathbf{z}$:

$$\begin{aligned} &\mathbf{A} \cdot \mathbf{y} = \mathbf{r} \\ &\mathbf{A} \cdot \mathbf{z} = \mathbf{u} \\ &\mathbf{x} = \mathbf{y} - \left( \frac{\mathbf{v} \cdot \mathbf{y}}{1 + \mathbf{v} \cdot \mathbf{z}} \right) \mathbf{z} \end{aligned} \tag{2.24}$$

Of course the spline is not determined in the whole domain, but only in a small region around the dispersed elements. It was found that when using a box around the bubble, which is extended by 10 cells in each direction, the results were indistinguishable from a global spline (Fig. 2.5).

Finally, to complement the higher order velocity interpolation, a fourth order Runge-Kutta time-integration is used, which is capable of tracking highly curved velocity fields:

$$\begin{aligned}
\mathbf{k}_0 &= \mathbf{u}\left(\mathbf{x}_0\right)\Delta t \\
\mathbf{k}_1 &= \mathbf{u}\left(\mathbf{x}_0 + \tfrac{1}{2}\mathbf{k}_0\right)\Delta t \\
\mathbf{k}_2 &= \mathbf{u}\left(\mathbf{x}_0 + \tfrac{1}{2}\mathbf{k}_1\right)\Delta t \\
\mathbf{k}_3 &= \mathbf{u}\left(\mathbf{x}_0 + \mathbf{k}_2\right)\Delta t \\
\mathbf{x} &= \mathbf{x}_0 + \frac{\mathbf{k}_0 + 2\mathbf{k}_1 + 2\mathbf{k}_2 + \mathbf{k}_3}{6}
\end{aligned} \tag{2.25}$$

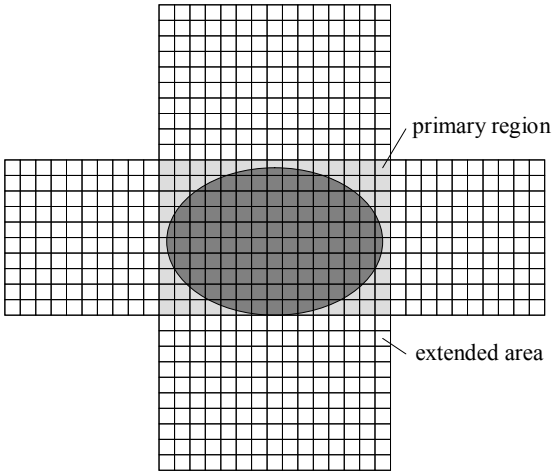


**Figure 2.5:** Local region around the dispersed phase for calculating the cubic spline.

### 2.2.7 Density and viscosity

Once the front has been moved, the phase fractions can be updated, in order to find the density and viscosity field. Traditionally the phase fractions $F_p$ are found by solving the following Poisson equation (Unverdi & Tryggvason, 1992), containing the interfacial gradient $\mathbf{G}_p$ that is calculated from the interface triangulation:

$$\begin{aligned}
\nabla^2 F_p &= \nabla \cdot \mathbf{G}_p \\
\mathbf{G}_p &= \sum_{m \in p} D(\mathbf{x} - \mathbf{x}_m)\mathbf{n}_m S_m
\end{aligned} \tag{2.26}$$

The drawback of this method is that the gradient has to be distributed to the Eulerian grid and as a consequence, the phase fractions are smeared out. Secondly, the numerical scheme creates under- and overshoots, which affect the volume of the dispersed phase and have to be filtered out. Finally, solving an additional Poisson equation is computationally demanding, especially for large numbers of bubbles.
Therefore in this work a novel method is introduced, which calculates the phase fractions directly from the location of the surface markers. It uses the triangular surface

markers to calculate the volume in each cell piece by piece (Fig. 2.6). The calculation of the volume under a marker follows straightforwardly from the location of its centre of mass in the z-direction $z_m$, the surface normal $\mathbf{n}_m$ and the surface area $S_m$:

$$\begin{aligned} V_m(i,j,k) &= (-\mathbf{e}_z \cdot \mathbf{n}_m) S_m (k\Delta z - z_{m,c}) \quad (k = k_m) \\ V_m(i,j,k) &= (-\mathbf{e}_z \cdot \mathbf{n}_m) S_m \Delta z \quad (k > k_m) \end{aligned} \tag{2.27}$$

where the integration direction is arbitrarily chosen to be the +z direction. Depending on the direction of the outwards pointing normal vector $\mathbf{n}_m$ the volume under the marker in a cell is either subtracted or added to the respective cell. After all the contributions from the markers of a bubble are added, only the volume inside the bubble remains (Fig. 2.7). Once the contribution of each marker is known, the phase fractions can be calculated by adding the contributions of all the markers in a cell belonging to phase $p$:

$$F_p(i,j,k) = \frac{1}{\Delta x \Delta y \Delta z} \sum_{m \in p} V_m(i,j,k) \tag{2.28}$$

The only remaining problem occurs when a marker occupies more than one cell. In this case the marker will have to be distributed over these respective cells, for which a 'cutting' procedure is proposed (Fig. 2.8). The basis of this method is to cut each line segment if it crosses a cell boundary, consequently creating 3 smaller triangles.

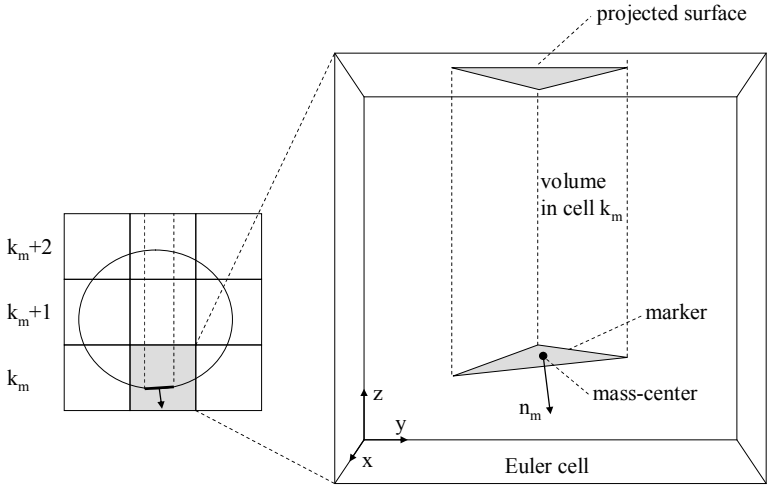


**Figure 2.6:** Volume-integration in the novel phase fraction calculation. The volume above marker m is added to or subtracted from cell $k_m$, depending on the direction of its normal vector. Other cells above that, all receive a contribution which corresponds to the surface area times the grid spacing ( $S_m \Delta z$ ).

Now that the phase fractions are known, the local density and viscosity can be calculated. For the density a standard volume-weighing method is used (Eq. 2.29), while for the viscosity harmonic averaging is employed (Eq. 2.30). According to Prosperetti (2002) the harmonic averaging significantly improves the continuity of tangential stress across the interface. Note that not only the calculation, but also the interpolation of the viscosity is carried out harmonically.

$$\rho(i,j,k) = \sum_{p=0}^{N_{ph}-1} F_p(i,j,k)\,\rho_p \tag{2.29}$$

$$\frac{\rho(i,j,k)}{\eta(i,j,k)} = \sum_{p=0}^{N_{ph}-1} F_p(i,j,k)\,\frac{\rho_p}{\eta_p} \tag{2.30}$$

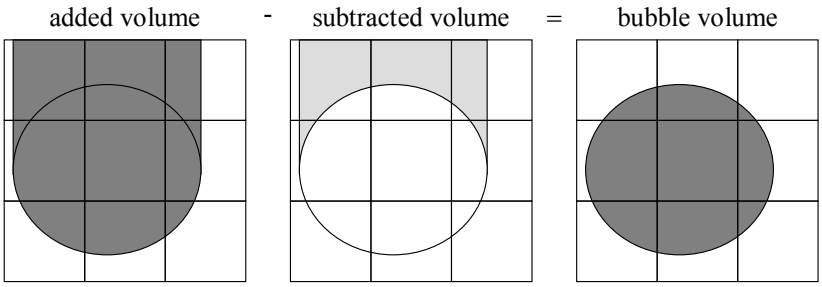


**Figure 2.7:** Situation after all the contributions of the markers for a bubble have been collected. It can be seen that for the area above the bubble, the added volume cancels the subtracted volume out, so that the correct bubble volume is obtained.

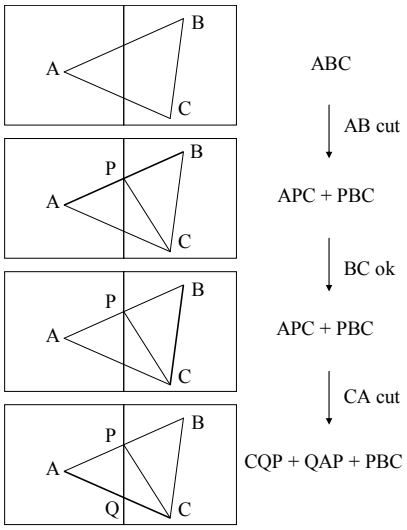


**Figure 2.8:** Marker cutting procedure, which is used for distributing markers across the different grid cells. Each line segment of the marker crossing a cell boundary divides the subtriangle in three smaller triangles.

### 2.2.8 Remeshing

The restructuring of the front consists of two elementary operations: marker addition and removal. For both operations the length of the line segments is used as the criterion: when a line segment is too small, two markers are removed (Fig. 2.9). For a line segment which is longer than a prescribed value, an additional point is placed in the middle of the line segment and two extra markers are created.

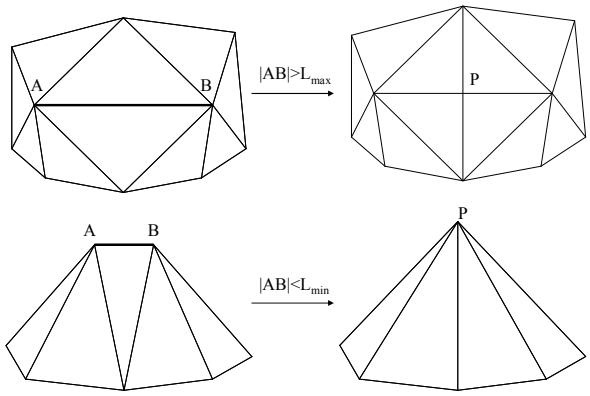


**Figure 2.9:** Surface grid remeshing procedures for line segments which are either larger (top) or smaller than a set value (bottom).

## 2.3 Test cases

This paragraph demonstrates the effect of the proposed modifications to the performance of the 3D Front Tracking model. First, the surface tension treatment is tested by comparing simulations to analytical results for a spherical, stationary bubble in a gravitationless field. This case is followed by a standard advection test, which quantifies the error introduced by moving the front. Thirdly, the discretisation of the Navier-Stokes equations is verified by simulating an oscillating bubble with viscous damping and comparing with an analytical solution. Finally, the speed-up achieved by using the optimized ICCG matrix solver is shown.

### 2.3.1 Stationary bubble

The improvement achieved by the new treatment of the pressure jump at the bubble surface is demonstrated for a spherical bubble in a zero-gravity environment. It is well-known that in this case there is an excess pressure inside the bubble, exactly counterbalancing the surface tension forces. As a result, a force balance gives the analytical value of the pressure jump:

$$\Delta p_{th} = \frac{4\sigma}{d} \tag{2.31}$$

It can be seen that both the surface tension force and interfacial pressure jump are proportional to the surface tension coefficient and the inverse bubble diameter

(curvature). This knowledge is used to define suitable dimensionless errors, which are completely independent of all physical properties and the bubble diameter. First of all, the $L_2$-error norm of the surface tension force on the individual markers is defined (Eq. 2.32). Secondly, the error in the pressure jump can be directly compared to its theoretical counterpart (Eq. 2.33). Fig. 2.10 (left) clearly shows that the surface tension $L_2$-error norm decreases with order ½, which can be explained by the fact that the accuracy of the pull-forces varies with the tangent length ( $\sim N_m^{-1/2}$ ). On the other hand, the relative error in the pressure jump is several orders of magnitude lower and depends linearly on the number of markers, because it is a surface force.

$$E_\sigma = \sqrt{\frac{1}{N_m}\sum_{m=1}^{N_m}\frac{\left|\mathbf{F}_{\sigma,m} - \Delta p_{th} S_m \mathbf{n}_m\right|^2}{\left(\Delta p_{th} S_m\right)^2}} \tag{2.32}$$

$$E_p = \frac{\Delta p_{sim} - \Delta p_{th}}{\Delta p_{th}} \tag{2.33}$$

The mismatch between the surface tension force and interfacial pressure jump results in false momentum, which can also be quantified in a dimensionless form:

$$E_{momentum} = \frac{\left|\rho \mathbf{u}\right|_{\max}}{\left|\rho \mathbf{u}\right|_{th,\max}} = \frac{\Delta x}{\Delta t}\frac{\rho \left|\mathbf{u}\right|_{\max}}{\Delta p_{th}} \tag{2.34}$$

Figure 2.10 (right) shows that with the conventional treatment of the pressure jump the error is constant at approximately 4%. This proves that in traditional FT models, the treatment of the pressure jump using the Euler grid is the limiting factor and not the computation of the surface tension forces. Only with the new implementation to account directly for the pressure jump, does the error decrease first order with the number of markers. Note that the difference in errors between cases where the bubble diameter is equal to 10 and 20 Euler cells is related to the smaller width of the distribution function at higher resolution. The error can be reduced again by using a larger stencil for mapping, however at the expense of the 'sharp-interface' philosophy. It can be concluded that the typical improvement is about two orders of magnitude, which has been realized without the additional computational costs of a higher order pressure discretisation (Scardovelli and Zaleski, 1999).

Finally, the steady-state magnitude of the spurious currents with viscous damping can be compared to literature values for full 3D simulations. The two sources found in literature (Table 2.2) show a rough estimate of this error in the form of a dimensionless capillary number, evaluated for a limited range of Laplace numbers:

$$Ca = \frac{\eta \left| \mathbf{u} \right|_{\max}}{\sigma}$$
$$La = \frac{\rho \sigma d}{\eta^2} \tag{2.35}$$

**Table 2.2:** Literature values for the maximum steady-state spurious currents around a perfect sphere.

| Source | $d / \Delta x$ | La | Ca |
|---|---|---|---|
| de Sousa et al. (2004) | 12.5 | 250 | $O(10^{-3})$ |
| | 25 | | $O(10^{-4})$ |
| Singh & Shyy (2007) | - | 250 - 12000 | $O(10^{-4})$ |
| This work | ≥10 | 1 - 10000 | $<2.2 \cdot 10^{-5}$ |

Our simulations, which have been carried out over a wide range of Laplace numbers, show a similar error of $O(10^{-3})$ for the classic Eulerian treatment of the pressure jump (Fig. 2.11, left). The improvement by means of the new method to account for the pressure jump reduces this error by two orders of magnitude (Fig. 2.11, right), which agrees with the instantaneous error in the momentum (Fig. 2.10, right).

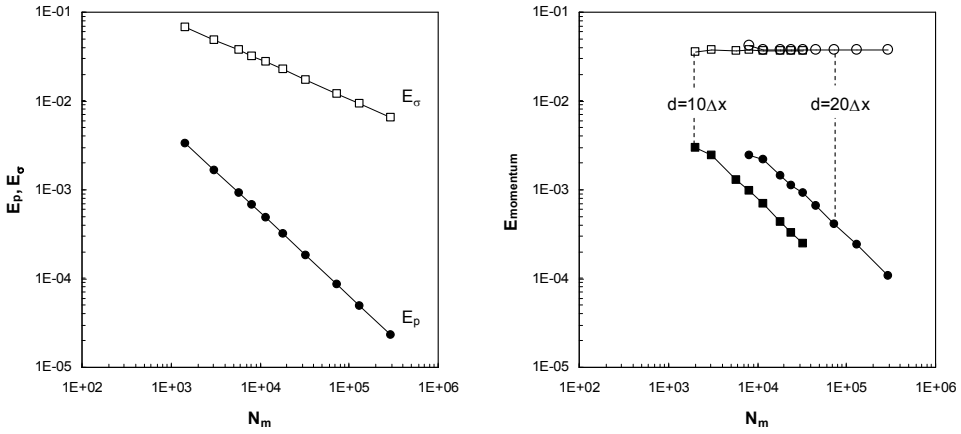


**Figure 2.10:** $L_2$-error norm for the surface tension force on a single marker and the interfacial pressure jump (left) as a function of the number of markers. Dimensionless false momentum as a result of the mismatch between surface tension forces and interfacial pressure jump (right), as a function of the number of markers.

Secondly, it was found that when using the traditional Eulerian treatment of the pressure jump, the error depends only on the Eulerian grid size and not on the number of markers. This is conclusive evidence that the main problem of the traditional FT implementation is in the treatment of the pressure jump and not the accuracy of the surface tension model, as was first pointed out by Scardovelli & Zaleski (1999). By

using the new and more accurate treatment of the pressure jump at the interface FT can significantly outperform other models, which makes it possible to run calculations with very high surface tension forces on relatively coarse grids.
Next to a quantitative difference, there is also a qualitative difference in the spurious currents around the bubble, as illustrated in Fig. 2.12 (velocity vectors not on the same scale). It can be seen that the traditional implementation gives erratic velocity vectors at the interface, while the improved version has a clear circulation pattern inside the bubble, indicating superior stability.

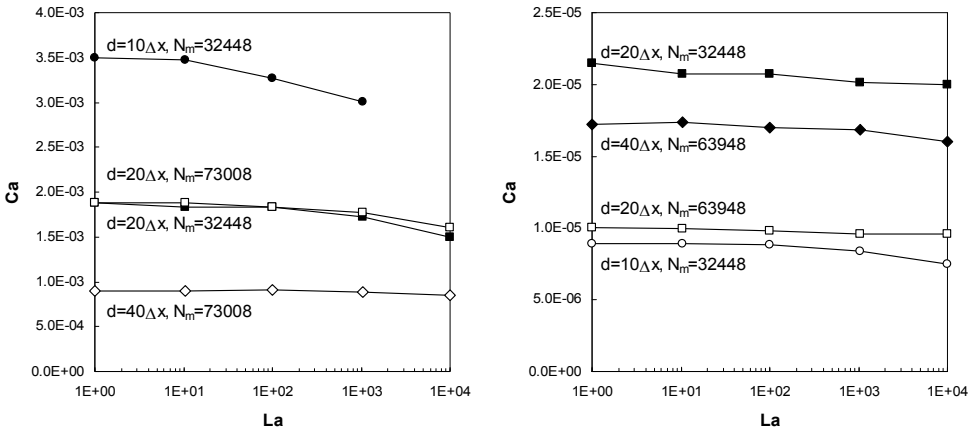


**Figure 2.11:** Steady-state capillary number for a spherical bubble as a function of the Laplace number. It can be seen that the error using the traditional FT implementation (left) is three orders of magnitude higher than the improved model to account for the pressure jump at the bubble interface (right).

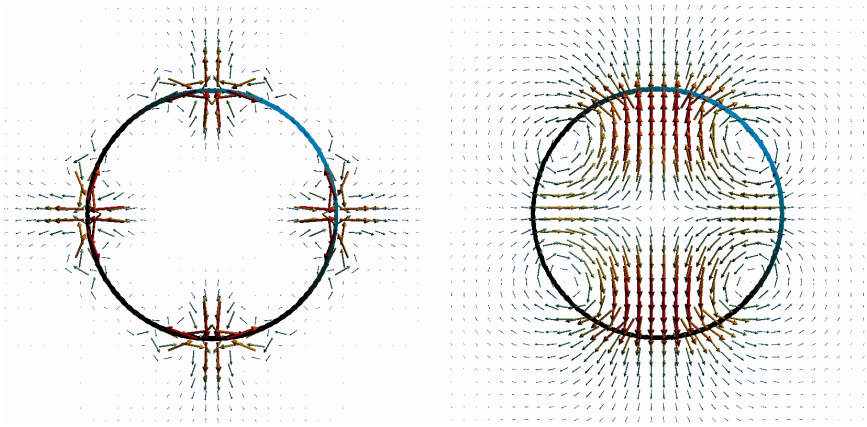

**Figure 2.12:** Spurious vector field (not on the same scale) around the central slice of a spherical bubble. It can be seen that the standard Eulerian pressure treatment (left) gives many erratic vectors at certain locations on the interface, while the new implementation to account for the pressure jump at the interface (right) yields a much smaller and symmetric circulation pattern.

### 2.3.2 Standard advection test

The advection of the interface is studied using a standard advection test (following Rider & Kothe, 1998), which involves a bubble with radius ¼ at a dimensionless position (½, ½, ¾) in a rotational velocity field given by:

$$\mathbf{u}(y,z) = \left(0, -2\sin^2(\pi y)\sin(\pi z)\cos(\pi z), 2\sin^2(\pi z)\sin(\pi y)\cos(\pi y)\right) \quad (2.36)$$

In this case a computational domain consisting of 40x40x40 cells is used with 200 time steps of 0.01 s. Because the velocity field is divergence free, the bubble volume should always be conserved. Secondly, after reversing the velocity field halfway (after 1 s), the bubble should return exactly to its starting position. However, due to the finite accuracy of the numerical schemes used, there can be an error in the volume, location and shape of the bubble. The errors in the location and volume of the bubble are analyzed quantitatively in Table 2.3. The results show that the Runge-Kutta time integration reduces all errors by a factor of one million, regardless of the method for the velocity interpolation used. However, a higher order velocity interpolation (3rd order spline) is still important in order to keep the bubble surface smooth (Fig. 2.4). With the addition of remeshing, the error rises significantly, but it can be seen that the higher order advection still improves the volume conservation. Last but not least, the shape of the bubbles, together with the flow field is shown in Fig. 2.13. It can be seen that for the standard Euler time integration with linear interpolation, the bubble shape at the end of the test is far from spherical, while for the higher order interpolation and time-stepping the error is negligible.

**Table 2.3:** Errors in the standard advection test for different advection schemes (V = bubble volume; x = dimensionless bubble position).

| Numerical scheme | | | t = 1 s | t = 2 s | |
|---|---|---|---|---|---|
| Interpolation | Time stepping | Remeshing | $(V-V_0)/V_0$ | $(V-V_0)/V_0$ | $x-x_0$ |
| Linear | Euler | - | $-9.71\cdot10^{-3}$ | $-3.36\cdot10^{-2}$ | $6.93\cdot10^{-2}$ |
| Linear | Runge-Kutta | - | $-8.51\cdot10^{-4}$ | $1.48\cdot10^{-8}$ | $2.03\cdot10^{-9}$ |
| Spline | Euler | - | $-9.88\cdot10^{-3}$ | $-3.41\cdot10^{-2}$ | $6.99\cdot10^{-2}$ |
| Spline | Runge-Kutta | - | $-8.55\cdot10^{-4}$ | $1.44\cdot10^{-8}$ | $2.03\cdot10^{-9}$ |
| Linear | Euler | X | $-1.37\cdot10^{-2}$ | $-4.27\cdot10^{-2}$ | $6.92\cdot10^{-2}$ |
| Spline | Runge-Kutta | X | $-4.76\cdot10^{-3}$ | $-8.92\cdot10^{-3}$ | $2.72\cdot10^{-4}$ |

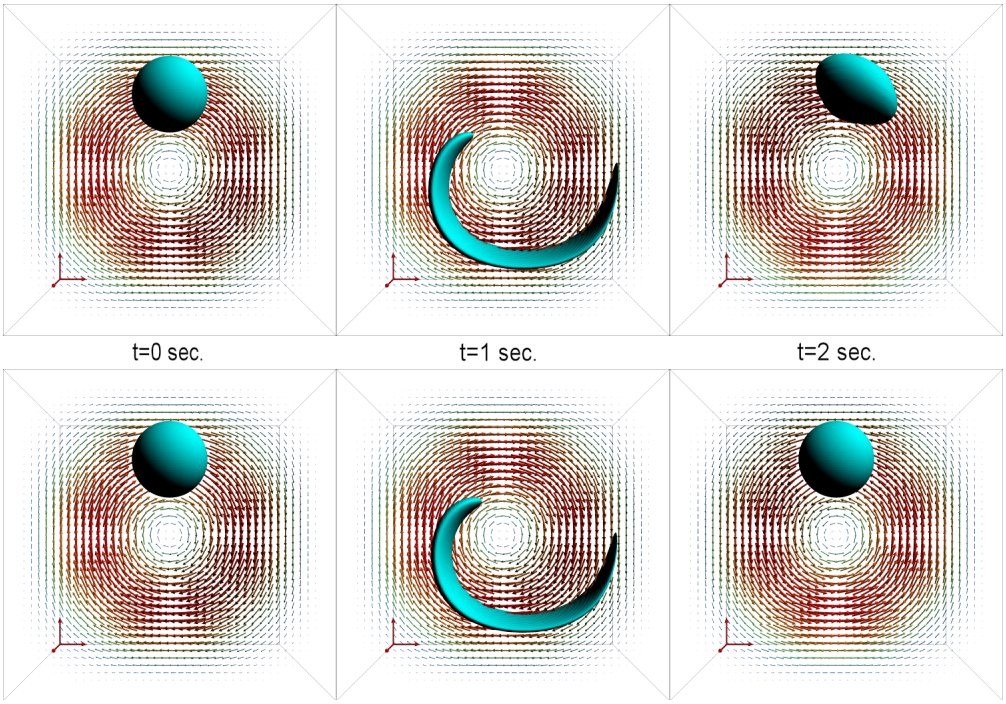


**Figure 2.13:** Visualization of the bubble interface and the velocity profile during the standard advection test. The top row uses 1st order velocity interpolation and 1st order Euler time stepping, while the bottom row uses a 3rd order spline velocity interpolation and Runge-Kutta time stepping. It can be seen that the 1st order approach yields a considerable error in both the position and the shape of the bubble, while for the higher order case the error is unnoticeably small.

### 2.3.3 Oscillating drop with viscous damping

In order to verify the correct interchange between the surface tension force and momentum, an oscillating drop is simulated. For an inviscid drop the analytical solution for the frequency of the lowest mode is given by Eq. 2.37 (Lamb, 1932), while the viscous damping of the initial amplitude $a_0$ can be described by Eq. 2.38 and 2.39.

$$\omega^2 = \frac{3\sigma}{\left(3\rho_d + 2\rho_f\right)d^3} \tag{2.37}$$

$$a(t) = a_0 \exp\left(-\frac{t}{\tau}\right) \tag{2.38}$$

$$\tau = \frac{\rho_d d}{10\eta_d} \tag{2.39}$$

This leads to the following overall equation for the drop diameter as a function of time:

$$d(t) = d_0 + a_0 \exp\left(-\frac{t}{\tau}\right)\cos(\omega t) \tag{2.40}$$

To be able to compare the model results with this analytical solution, a system is selected with a relatively low viscosity for the continuous phase (Table 2.4). A typical resolution of the drop ( $d = 20\Delta x$ ) is used and the properties of the continuous phase are chosen such that they do not affect the solution: the density and kinematic viscosity ratio are both ~1000. It can be seen from Fig. 2.14 that there is an excellent agreement between the numerical results and the analytical solution. The period of the oscillation is perfectly reproduced and the error in the amplitude is only approximately 3%.

**Table 2.4:** Physical and numerical settings for the oscillating drop case.

| Property (dimensionless) | Value |
|---|---|
| Domain size | 40x40x40 |
| Grid size, $\Delta x$ | 0.1 |
| Time step, $\Delta t$ | 0.05 |
| Equivalent drop diameter, $d_0$ | 1 |
| Initial amplitude, $a_0$ | 0.025 |
| Dispersed phase density, $\rho_d$ | 100 |
| Dispersed phase viscosity, $\eta_d$ | 0.35 |
| Continuous phase density, $\rho_d$ | 0.1 |
| Continuous phase viscosity, $\eta_d$ | $1 \cdot 10^{-6}$ |
| Surface tension coefficient, $\sigma$ | 10 |

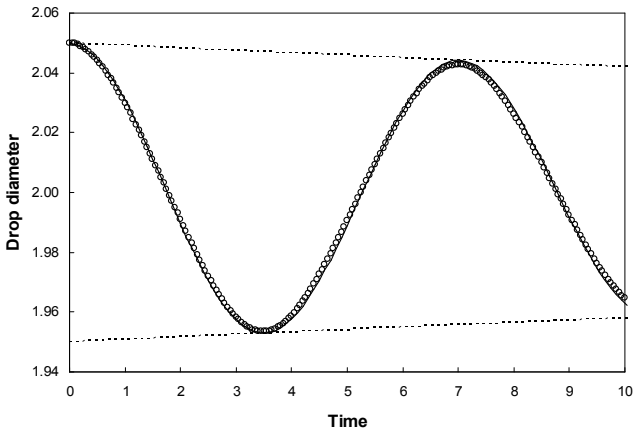


**Figure 2.14:** Bubble diameter for an oscillating drop with viscous damping. The symbols represent the numerical simulation, while the solid line is the analytical solution. The dashed line indicates the maximum and minimum drop diameter (amplitude).

### 2.3.4 Matrix solver speed-up

The optimized ICCG matrix solver was tested on a variety of popular computer hardware running at equal clock speed; both professional and consumer grade (Table 2.5). The first test case is a single bubble in an 'infinite' liquid, for which a 4 mm air bubble in water was selected. The cubic domain corresponds to 5 bubble diameters and free-slip boundaries are used for all walls. Figure 2.15 (left) shows that both the reduction of the number of bands and the matrix scaling yield a consistent improvement, which depends somewhat on the type of hardware. Overall, there is a consistent improvement by a factor of 1.4 to 2.4 for typical simulations ($>10^6$ nodes). Since the matrix solver typically accounts for more than 90% of the wall time, this is also the speed-up of an entire FT simulation.
Secondly, a case with periodic boundary conditions was tested, in which the domain is two bubble diameters wide (Figure 2.15, right). This case is typical for researching swarm effects, in which much higher gas hold-ups are of interest. Naturally, it was found that reducing the number of bands from thirteen to four yields a much larger improvement than for the free-slip case. However – as expected – the effect of matrix scaling is less, since there are significantly less continuous phase cells. Nevertheless, the overall speed-up is significantly higher at 1.8 to 3.8, depending on the computer architecture.

**Table 2.5:** Different computer systems used to benchmark the optimized ICCG matrix solver.

| Processors | Cores | Clock (GHz) | Memory |
|---|---|---|---|
| AMD Athlon 64X2 4600+ | 2 | 2.4 | 2x1 GB DDR2-800 (dual channel) |
| AMD Opteron 280 (2x) | 4 | 2.4 | 8x1 GB DDR-400 (quad channel) |
| Intel Core2Duo E6600 | 2 | 2.4 | 2x1 GB DDR2-533 (dual channel) |
| Intel Xeon X5355 (2x) | 8 | 2.66 | 8x1 GB FBD-667 (quad channel) |

Now that it is clear that the improvement realized by optimizing the matrix solver is highly dependent on the type of computer used, it is interesting to compare their performance at identical clock speed (Fig. 2.16). It can be seen that after optimization, the differences in performance between different processors and different boundary conditions have become surprisingly small for a single serial job. However, when multiple simulations are run, there are significant differences in the overall performance. Fig. 2.17 shows that - compared to a single simulation - the performance is reduced by 25 to 70% depending on the computer hardware. For instance when utilizing all eight processor cores on the dual Intel Xeon, the efficiency drops to around 30%, which is caused by a lack of memory band width. On the other hand, the AMD AthlonX2 processor performs relatively well, which can be attributed to its integrated memory controller and support for very high memory clock speeds.

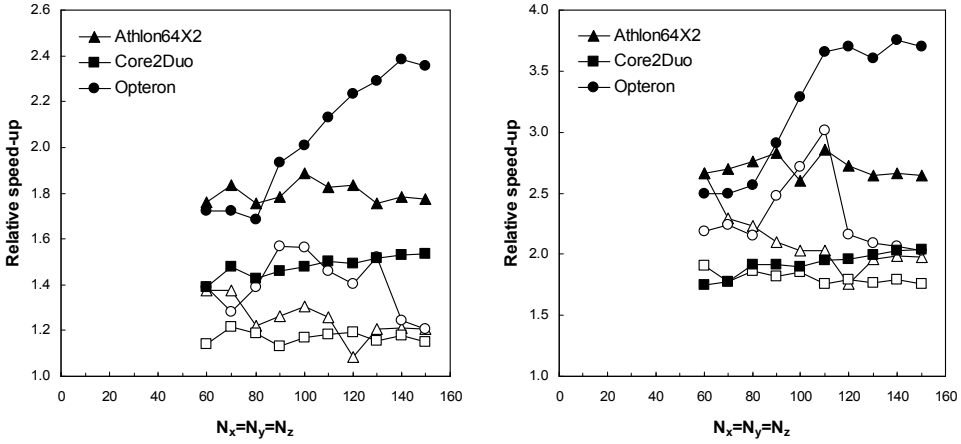


**Figure 2.15:** Matrix solver speed-up for the simulation of a single air bubble in water using a cubic domain with free-slip boundaries (left) and a periodic domain (right). Open symbols: reduction in the number of bands; closed symbols: band reduction and matrix scaling.

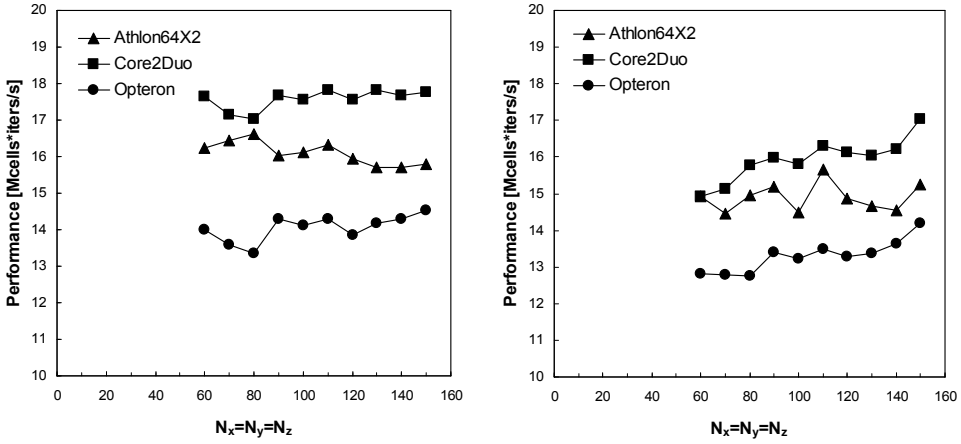


**Figure 2.16:** Relative performance after optimization for a single serial calculation, using a cubic domain with free-slip boundaries (left) and a periodic domain (right). It can be seen that the difference in performance between the different processors at identical clock frequencies is quite small.

The effect of the memory clock speed has been highlighted in Fig. 2.18: the performance depends linearly on the memory clock speed, which leads to the surprising conclusion that at full load not the CPU but the RAM is the bottleneck. This conclusion has been verified by using a 3.0 GHz processor, which is faster for a single simulation but gives the same performance for two simulations. Note that the slight depression between 533 and 667 MHz is caused by a change in memory latency from 4 to 5, which shows that not only the memory clock speed but also the access time plays an important role.

Now that the effects of both the CPU and the memory are understood, this can be taken into account when investing in computer hardware. Based on the very low cost and superior performance, a serial computer cluster was commissioned consisting of 47 dual-core AMD Athlon64X2 2.4 GHz processors, each with 4 GB of DDR2-800 memory (Fig. 2.19).

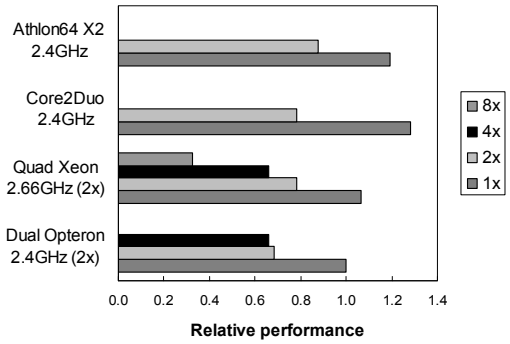


**Figure 2.17:** Relative performance running up to eight serial calculations (each $80^3$ cells) on different multi-core multi-processor systems.

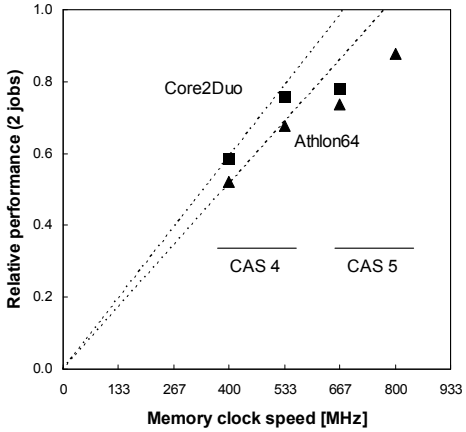


**Figure 2.18:** Relative performance at different memory clock speeds under full load (two identical simulations with $80^3$ grid cells). The performance depends linearly on the memory clock speed, which implies that memory rather than CPU speed is the bottleneck.

**Figure 2.19:** Serial computer cluster containing 94 processor cores, specifically selected for 3D Front Tracking calculations.

## 2.4 Conclusions

In this chapter, the improvements made to the 3D Front Tracking code have been described and their effects benchmarked. First a new method to account for the pressure jump is described and it has been shown that this method reduces the spurious currents by two orders of magnitude and solves volume loss issues for small bubbles with high surface tension forces. Secondly, the interface advection has been improved (higher order velocity interpolation and time stepping), resulting in less volume conservation errors and a noticeably smoother interface. Thirdly, the timestep constraint for viscous liquids was overcome by using a semi-implicit treatment of the stress tensor in the Navier-Stokes equations. Finally, the computational efficiency of the model has been improved by a factor of two to four by using a custom-made ICCG matrix solver. When combined, these improvements make it possible to simulate a wide range of bubble sizes in various fluids at reasonable computational cost.

## Symbols

| | | |
|---|---|---|
| $a$ | Amplitude | m |
| $\mathbf{A}$ | Matrix | - |
| $Ca$ | Capillary number | - |
| $d$ | Equivalent bubble diameter | m |
| $d_x, d_y, d_z$ | Distribution functions in one direction | - |
| $D$ | Volume weighing distribution kernel | - |
| $\mathbf{e}_z$ | Unit vector in the z-direction | - |
| $E$ | Error | - |
| $F$ | Force | N |
| $F_p$ | Phase fraction | - |
| $\mathbf{g}$ | Gravitational acceleration | $m \cdot s^{-2}$ |
| $\mathbf{G}_p$ | Gradient of the phase fraction | - |
| $h$ | Mesh width | m |
| $H$ | Heaviside function | - |
| $\mathbf{k}_i$ | Location estimates used in the Runge-Kutta time-stepping method | m |
| $La$ | Laplace number | - |
| $M_{i,j}$ | Second derivate of the spline | $m \cdot s^{-1}$ |
| $\mathbf{n}$ | Unit normal vector | - |
| $N$ | Number of cells | - |
| $N_m$ | Number of markers | - |
| $N_{ph}$ | Number of phases | - |
| $p$ | Pressure | Pa |
| $s$ | Spline (used for velocity interpolation) | m/s |
| $S$ | Surface area | $m^2$ |
| $\mathbf{t}$ | Tangent vector | m |
| $t$ | Time | s |
| $\mathbf{u}$ | Continuous phase velocity | $m \cdot s^{-1}$ |
| $\mathbf{u}, \mathbf{v}$ | Correction vectors in the Sherman-Morrison formula | - |
| $\mathbf{v}$ | Bubble velocity | $m \cdot s^{-1}$ |
| $V$ | Volume | $m^3$ |
| $x, y, z$ | Cartesian coordinates | m |
| $\mathbf{x}$ | Position | m |
| $\mathbf{x}$ | Solution vector | - |
| $\mathbf{y}, \mathbf{z}$ | Solution vectors in the Sherman-Morrison formula | - |
| $\delta p$ | Pressure correction | Pa |
| $\Delta p$ | Pressure jump | Pa |
| $\Delta t$ | Time step | s |
| $\Delta x, \Delta y, \Delta z$ | Grid spacing | m |

| | | |
|---|---|---|
| $\eta$ | Dynamic viscosity | Pa·s |
| $\rho$ | Density | $kg \cdot m^{-3}$ |
| $\sigma$ | Surface tension coefficient | $N \cdot m^{-1}$ |
| $\tau$ | Characteristic time | s |
| $\boldsymbol{\tau}$ | Stress tensor | $N \cdot m^{-2}$ |
| $\omega$ | Oscillation period | $s^{-1}$ |

Sub-/superscripts:

| | |
|---|---|
| $d$ | Dispersed phase |
| $f$ | Continuous phase |
| $i, j, k$ | Grid indices in the x-, y- and z-direction respectively |
| $m$ | Marker |
| $max$ | Maximum |
| $momentum$ | Momentum |
| $n$ | Current time-level |
| $n*, n**$ | Intermediate time-level |
| $n+1$ | Future time-level |
| $p$ | Phase |
| $th$ | Theoretical |
| $x, y, z$ | Cartesian directions |
| 0 | Initial value |
| $\sigma$ | Surface tension |

## References


1. J. Centrella and J. Wilson, Planar numerical cosmology. II. The difference equations and numerical tests, *Astroph. J. Suppl. Series* **54** (1984), 229.
2. N.G. Deen, M. van Sint Annaland, and J.A.M. Kuipers, Multi-scale Modeling of Dispersed Gas-Liquid Two-Phase Flow, *Chem. Eng. Sci.* **59** (2004), 1853.
3. W. Dijkhuizen, E.I.V. van den Hengel, N.G. Deen, M. van Sint Annaland, and J.A.M. Kuipers, Numerical investigation of closures for interface forces acting on single air-bubbles in water using volume of fluid and front tracking models; *Chem. Eng. Sci.* **60** (2005), 6169.
4. H. Lamb, Hydrodynamics, 6th edition, Cambridge University Press, London (1932).
5. R. Palaparthi, D.T. Papageorgiou and C. Maldarelli, Theory and experiments on the stagnant cap regime in the motion of spherical surfactants-laden bubbles, *J. Fluid Mech.* **559** (2005), 1-44.
6. C.S. Peskin and B.F. Printz, Improved volume conservation in the computation of flows with immersed elastic boundaries, *J. Comp. Ph.* **105** (1993), 33.
7. S. Popinet and S. Zaleski, A front-tracking algorithm for the accurate representation of surface tension, *Int. J. Numer. Meth. Fluids* **30** (1999), 775.
8. A. Prosperetti, Navier-Stokes numerical algorithms for free-surface flow computations: an overview, Drop-surface interaction **237** (2002).

9. W.J. Rider and D.B. Kothe, Reconstructing volume tracking, *J. Comp Ph.* **141** (1998), 112.
10. R. Scardovelli and S. Zaleski, Direct numerical simulation of free-surface and interfacial flow, *Annu. Rev. Fluid Mech.* **31** (1999), 567.
11. S. Shin and D. Juric, Modeling Three-Dimensional Multiphase Flow Using a Level Contour Reconstruction Method for Front Tracking without connectivity, *J. Comp. Ph.* **180** (2002), 427.
12. R. Singh and W. Shyy, Three-dimensional adaptive Cartesian grid method with conservative, interface restructuring and reconstruction, *J. Comp. Ph.* **224** (2007), 150-167.
13. M. van Sint Annaland, N.G. Deen and J.A.M. Kuipers, Multi-level modeling of dispersed gas-liquid two-phase flows, series: Heat and mass transfer (eds. M. Sommerfeld and D. Mewes), Springer, Berlin (2003).
14. M. van Sint Annaland, W. Dijkhuizen, N.G. Deen and J.A.M. Kuipers, Numerical simulation of gas bubbles behaviour using a 3D front tracking method, *AIChE J.* **52** (2006), 99.
15. F.S. de Sousa, N. Mangiavacchi, L.G. Nonato, A. Castelo, M.F. Tomé, V.G. Ferreira, J.A.Cuminato and S. McKee, A front-tracking/front-capturing method for the simulation of 3D multi-fluid flows with free surfaces, *J. Comp. Ph.* **198** (2004), 469.
16. G. Tryggvason, B. Bunner, A. Esmaeeli, D. Juric, N. Al-Rawahi, W. Tauber, J. Han, S. Nas and Y.-J. Jan, A front-tracking method for the computations of multiphase flows, *J. Comp. Ph.* **169** (2001), 708.
17. M. Uhlmann, An immersed boundary method with direct forcing for the simulation of particulate flows, *J. Comp. Ph.* **209** (2005), 448-476.
18. S.O. Unverdi and G. Tryggvason, A front tracking method for viscous, incompressible, multi-fluid flows, *J. Comp. Ph.* **100** (1992), 25.
19. S. Zaleski, Interface Tracking – VOF, *VKI lecture series*, Von Karman Institute for Fluid Mechanics, Belgium (2005).

# 3

# Drag force


## Abstract

The drag force is one of the most important forces encountered in bubbly flows, since it dominantly controls the rise velocity of the bubbles and the momentum transfer to the liquid phase. There are many factors that affect it, like the bubble size and shape, physical properties and even the purity of the liquid. In this chapter DNS has been used to derive closures for the drag force exerted on a single rising bubble in an 'infinite', initially stagnant liquid. For comparison, experiments using a high-speed camera have been carried out for air bubbles with different volume, injected in various water/glycerine mixtures. The simulations show a good correspondence to existing drag closures for spherical bubbles in pure liquids, but a large discrepancy was found for deformed bubbles. Therefore, a new drag closure for ultrapure liquids is introduced, which is valid for spherical as well as deformed bubbles. Also it has been demonstrated that DNS can be used to predict zigzagging and helical path instabilities for sufficiently large bubbles in inviscid liquids (i.e. air-water).

The (contaminated) experiments show a good comparison with the numerical simulations for systems with higher liquid viscosities, but for low viscosity liquids the measured drag force coefficient can be as much as seven times higher than computed with DNS, attributed to the effect of contaminants. Moreover, it is concluded that especially in this last case the experimentally observed bubbles are much less deformed, which may be related to the significantly lower measured rise velocity.

## 3.1 Introduction

This chapter deals with the drag force, which is unmistakably one of the most important forces in dispersed gas-liquid flows, requiring closure equations. The objective is to investigate a wide range of bubble diameters rising in liquids with very different viscosities. This is accomplished by exploiting the unique ability of our FT model to handle true physical properties, even at very high density and viscosity ratios, between the dispersed and continuous phases. The numerical simulations are compared to new experiments, performed using exactly the same physical properties, which will provide some validation and allows us to demonstrate the effect of contaminants, that are almost unavoidably present in our experiments, but which are not accounted for in the numerical simulations.

In this chapter, first the most important drag force correlations from literature are described. Secondly, based on a simple force balance for a discrete bubble, an equation is derived to obtain the drag force coefficient from the bubble rise velocity. In the remainder of this chapter the experimental set-up and numerical aspects are described, followed by a discussion of the results.

### 3.1.1 Existing drag closures

The first drag closure was derived analytically by Stokes (1851) and is valid for rigid spheres at low Reynolds numbers (Eq. 3.1), including bubbles with an immobile interface (contaminated liquids). A popular correction factor extends the Stokes solution to larger Reynolds numbers (Eq. 3.2), which makes it suitable for use in practical situations.

$$C_D = \frac{24}{\mathrm{Re}} \qquad \mathrm{Re} \ll 1 \qquad (3.1)$$

$$C_D = \frac{24}{\mathrm{Re}}\left(1 + 0.15\,\mathrm{Re}^{0.687}\right) \qquad (3.2)$$

The analytical method developed by Stokes was also used by Hadamard (1911) and Rybcszynski (1911) to compute the drag for spheres with a mobile interface (pure liquids), obtaining a solution of 2/3$^{rd}$ of that exerted on a rigid sphere (Eq. 3.3). Levich (1949) has estimated the drag force coefficient in the limit of high Reynolds numbers, assuming that there is no flow separation, which was later corrected by Moore (1963) for the existence of a thin boundary layer and narrow wake (Eq. 3.4). Finally, Mei et al. (1994) presented an empirical drag law that matches both limits (Eq. 3.5). For a more extensive review of the different aspects of bubbles at high Reynolds numbers, the interested reader is referred to Magnaudet & Eames (2000).

$$C_D = \frac{16}{\mathrm{Re}} \qquad \mathrm{Re} << 1 \qquad (3.3)$$

$$C_D = \frac{48}{\mathrm{Re}}\left(1 - \frac{2.21}{\mathrm{Re}^{0.5}}\right) \qquad \mathrm{Re} >> 1 \qquad (3.4)$$

$$C_D = \frac{16}{\mathrm{Re}}\left(1 + \frac{2}{1 + \frac{16}{\mathrm{Re}} + \frac{3.315}{\mathrm{Re}^{0.5}}}\right) \qquad (3.5)$$

The previous solutions are all limited to spherical bubbles, while industrial applications studied with CFD almost always contain deformed bubbles. For these applications one of the most widely used correlations is the one proposed by Tomiyama (1998), because it is relatively simple and holds for spherical as well as deformed bubbles. There are two closures, one for pure and one for contaminated liquids (Eqn. 3.6 and 3.7), in line with the Stokes and Hadamard-Rybcszynski limiting solutions. It is important to recall that Tomiyama's correlation for 'pure' liquids has been derived from experiments using demineralized water, rather than ultrapurified water, which is known to give a higher drag force (Veldhuis, 2007). This effect will be shown in detail in the results section.

$$C_D = \max\left[\min\left[\frac{16}{\mathrm{Re}}\left(1 + 0.15\,\mathrm{Re}^{0.687}\right), \frac{48}{\mathrm{Re}}\right], \frac{8}{3}\frac{Eo}{Eo + 4}\right] \quad \text{('pure' liquids)} \qquad (3.6)$$

$$C_D = \max\left[\frac{24}{\mathrm{Re}}\left(1 + 0.15\,\mathrm{Re}^{0.687}\right), \frac{8}{3}\frac{Eo}{Eo + 4}\right] \quad \text{(contaminated liquids)} \qquad (3.7)$$

### 3.1.2 Derivation of the drag force coefficient

The drag coefficient for a bubble rising in an initially quiescent liquid can be obtained from a steady-state force balance in the vertical direction (Eq. 3.8). A spherical-equivalent bubble diameter is used, to facilitate its application in discrete bubble and Euler-Euler models, which typically do not contain information regarding the shape of the bubble. As a consequence, the effect of the bubble shape is implicitly lumped in the drag force coefficient, yielding a practical and elegant closure.

$$\begin{aligned} 0 &= F_B + F_D \\ 0 &= V\left(\rho_L - \rho_G\right)g - C_D A \frac{\rho_L}{2}\left|v_z - u_z\right|\left(v_z - u_z\right) \\ 0 &= \frac{\pi}{6}d^3\left(\rho_L - \rho_G\right)g - \frac{\pi}{8}d^2\rho_L C_D\left(v_z - u_z\right)^2 \end{aligned} \qquad (3.8)$$

For bubbles in the wobbling regime, which may exhibit different kinds of path- or shape-instabilities, time-averaging is required to compute the drag coefficient. This can be done in two slightly different ways: using the square of the average velocity or the average of the velocity squared. The liquid macro-scale circulation patterns in a bubble column depend crucially on the momentum exchange between the two phases, the second approach using the average drag force is employed throughout this chapter (Eq. 3.9).
Alternatively, the square of the average velocity can be used, if the bubble velocity (e.g. residence time in a bubble column) is more important than momentum transfer. The difference between both approaches has been calculated for air bubbles rising in water (0.3 - 7 mm), for which the largest effect can be expected, and found to be negligibly small (<0.5%).

$$\begin{aligned} 0 &= \langle F_B \rangle + \langle F_D \rangle \\ 0 &= \frac{\pi}{6} d^3 \left(\rho_L - \rho_G\right) g - \frac{\pi}{8} d^2 \rho_L C_D \left\langle \left(v_z - u_z\right)^2 \right\rangle \\ C_D &= \frac{4d\left(\rho_L - \rho_G\right) g}{3\rho_L \left\langle \left(v_z - u_z\right)^2 \right\rangle} \end{aligned} \tag{3.9}$$

## 3.2 Experimental set-up

The experimental set-up consists of a square polycarbonate column with a steel bottom section containing a long thin tube, through which bubbles can be injected by means of two syringes (Fig. 3.1). The first syringe is used to inject a specific amount of air in a hose filled with liquid, after which the second syringe – filled with liquid – forces the bubble through the nozzle. Typically, the bubble is pushed through the injection tube at a rate of 0.01 m/s. It was found that this indirect injection technique enables a reproducible injection of the bubbles, allowing for a wide range of bubble diameters, without bubble break-up or excessive disturbances of the liquid in the column. Experiments with different water/glycerine mixtures were performed.

A high speed camera is used to track the motion of the bubbles at 100 Hz, using backlighting from a single 500 Watt halogen light. The back of the column is covered with white paper to give a diffuse lighting, thereby eliminating any reflections via the bubble surface or the column walls. The bubble dimensions and its centre of mass are determined at three points: after it enters, in the middle and before it leaves the field of view of the camera. Since the scale on the syringes used to inject air was not sufficiently accurate and there is an effect of the change in hydrostatic pressure as a function of the vertical position in the column, the equivalent bubble diameter is calculated from the measured horizontal and vertical bubble diameter:

$$d = \left( d_h^2 d_v \right)^{1/3} \tag{3.10}$$

The physical properties of the water/glycerine mixtures (Table 3.2) were measured at exactly the same temperature as was used in the experiments, using the same thermometer (0.1°C accuracy). The measurement devices and settings used to obtain the physical properties are listed in Table 3.3. After each measurement series the glycerine was diluted with demineralised water to obtain a new liquid with a viscosity approximately two times lower.

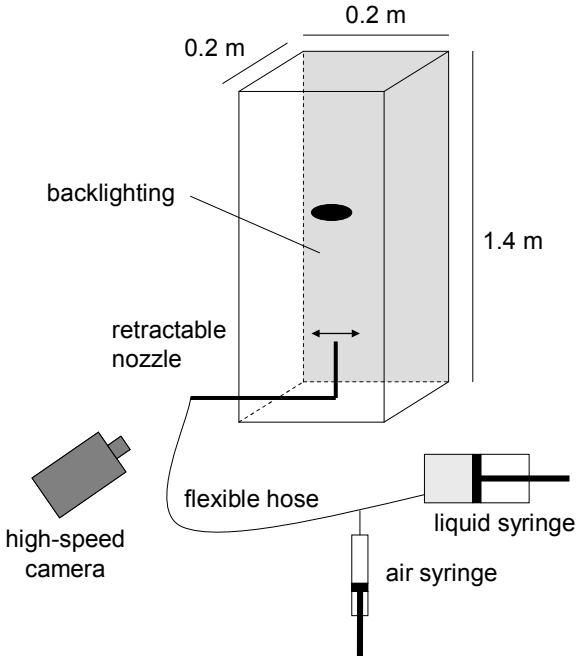


**Figure 3.1:** Schematic overview of the experimental set-up.

**Table 3.1:** Equipment used for the high-speed imaging experiments.

| Equipment | Details |
|---|---|
| Column | Polycarbonate walls, steel bottom section (0.20 x 0.20 x 1.40 m) |
| High-speed camera | Imager Pro HS CMOS camera<br>10 bits, 1280*1024 Pixels, Pixel size 12*12 μm<br>Max. 625 frames/s, 50 mm camera lens<br>Field-of-view: 0.068 x 0.108 m (w x h) |
| Backlighting | 500 Watt halogen light and white 80 grams paper covering the back wall of the column |
| Computer | Dual Xeon 2.66 GHz<br>Programmable Timing Unit |

**Table 3.2:** Physical properties for the water/glycerine mixtures used in the experiments and numerical simulations.

| | Viscosity [mPa·s] | Density [kg·m$^{-3}$] | Surface tension [mN·m$^{-1}$] | Morton number (Mo) |
|---|---|---|---|---|
| I | 153 | 1228 | 65 | $1.57 \cdot 10^{-2}$ |
| II | 81.8 | 1217 | 66 | $1.25 \cdot 10^{-3}$ |
| III | 45.7 | 1202 | 66 | $1.24 \cdot 10^{-4}$ |
| IV | 25.4 | 1185 | 67 | $1.14 \cdot 10^{-5}$ |
| V | 12.3 | 1163 | 68 | $6.05 \cdot 10^{-7}$ |
| VI | 5.04 | 1122 | 69 | $1.71 \cdot 10^{-8}$ |
| VII | 2.23 | 1071 | 69 | $6.87 \cdot 10^{-10}$ |
| VIII | 0.899 | 998 | 72 | $1.72 \cdot 10^{-11}$ |

**Table 3.3:** Measurements devices used to obtain the physical properties of the water/glycerin mixtures.

| Quantity | Measurement device | Error |
|---|---|---|
| Density | PAAR DMA 58 | 0.1 kg·m$^{-3}$ |
| Viscosity | Tamson thermostatic bath. Ubbelohde viscometers 65280 (I, II), 68145 (III-IV), 67365 (V, VI) and 6401 (VII, VIII). | 1% |
| Surface tension | KRÜSS K9 with platinum plate | 1 mN·m$^{-1}$ |

## 3.3 Numerical aspects

The numerical simulations have all been carried out with the improved 3D FT model, for a cubic computational domain consisting of one million cells with free-slip boundaries. The initially spherical bubble is centred horizontally and placed at 60% height of the computational domain, in order to provide some extra space for the wake structure. A moving window concept (Deen et al., 2004) is used to keep the bubble's position approximately constant inside the computational domain, so that the resolution around the bubble is always optimal. It was found that the typical simulation time is about one week, depending on the number of time steps required (~20000).

As an example, the determination of the procedure for obtaining the drag force coefficient and aspect ratio from a FT simulation is shown here for a 6 mm air bubble in water. Fig. 3.2 shows that the bubble takes about 0.1 second to get its approximate shape and drag force, after which it starts wobbling. The bubble takes one second to reach its steady state motion, which can then be used to determine the drag force coefficient and aspect ratio.

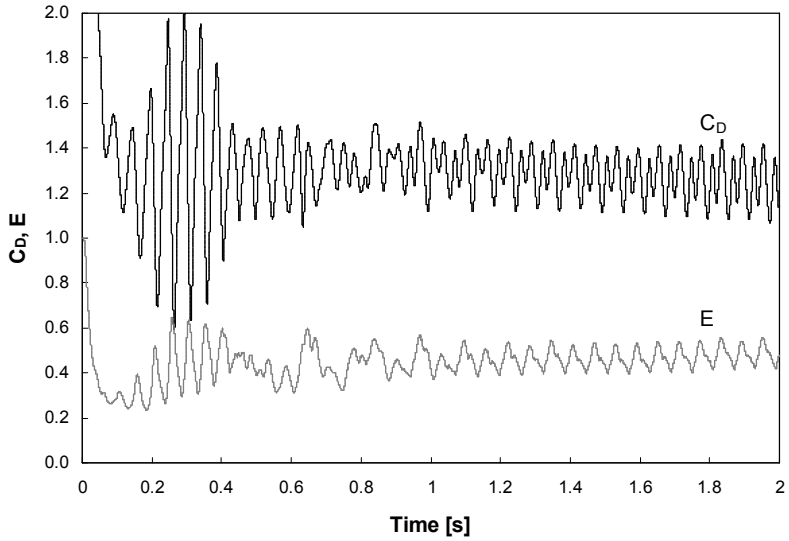


**Figure 3.2:** Drag force coefficient and bubble aspect ratio for a 6 mm air bubble in water, which rises along a zigzag path with shape oscillations.

For the most viscous liquids, the domain size is of paramount importance, while at higher Reynolds numbers the complex interface dynamics push the requirements towards more resolution. Therefore viscous liquids (I-III) are treated with an initial bubble diameter equal to 10 Eulerian cells (case A) and 20 cells (case B) on a bubble diameter are used for the less viscous cases (IV-VIII). The following paragraph will show this grid and resolution dependency in more detail, followed by a discussion of the influence of the computational time-step. Finally, the influence of the initial bubble shape on the results is shown in the last section.

**Table 3.4:** Numerical settings

| Property | Value |
|---|---|
| Mesh width | 15 - 800 μm (d=10dx / d=20dx) |
| Number of cells | 100x100x100 |
| Time step | $1.0 \cdot 10^{-5}$ - $1.0 \cdot 10^{-4}$ s |
| Simulation time | 0.1 - 2.0 s |
| Gas density | 1.21 kg·m$^{-3}$ |
| Gas viscosity | $1.52 \cdot 10^{-5}$ Pa·s |
| Liquid properties | same as experiments (Table 3.2) |

### 3.3.1 Grid dependency

The dependency of the drag force coefficient on the size of the computational domain is studied by comparing the results obtained using type A, B and C domains, detailed in

Fig. 3.3 for three data sets. First, Fig. 3.4 shows that for the most viscous liquid (I), the drag force approaches the Hadamart-Rybcszynski solution (16/Re) better when using the largest domain (type A). It can be seen that there is a small overshoot of the aspect ratio (E) using the lowest interface resolution, which is caused by some small disturbances of the triangulated interface. Secondly, the simulations using the moderately viscous liquid (Fig. 3.5) show similar results for all three cases, making it possible to switch to the highest resolution which is capable of handling larger higher bubble diameters as well. Finally, the air-water system (Fig. 3.6) shows that a higher resolution is required to get the proper drag force (Fig. 3.6). A lower resolution (case C) is simply not capable of accurately capturing the bubble shape dynamics, which is confirmed by discrepancies in the bubble aspect ratio.

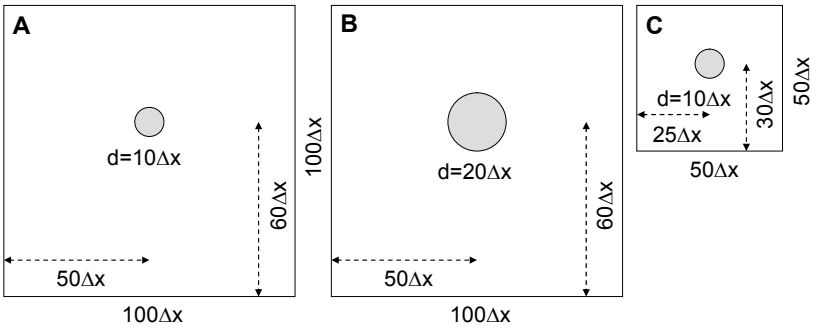


**Figure 3.3:** Numerical domains used for the drag force simulations. For viscous liquids domain size takes precedence (A), while the more complex bubble dynamics found in lower viscosity liquids depend more on bubble resolution (B). Domain type C is only used to study the domain size and grid dependency.

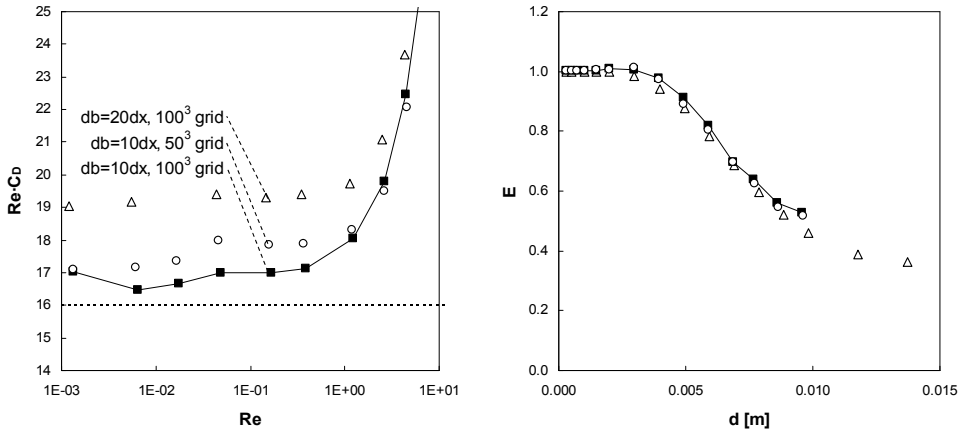


**Figure 3.4:** Drag force coefficient and bubble aspect ratio at different resolutions and domain sizes for a single air bubble in liquid I.

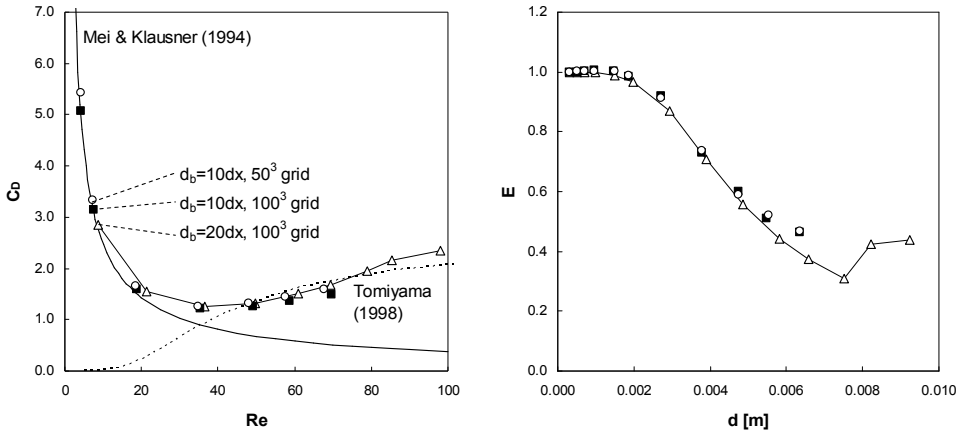


**Figure 3.5:** Drag force coefficient and bubble aspect ratio at different resolutions and domain sizes for a single air bubble in liquid IV.

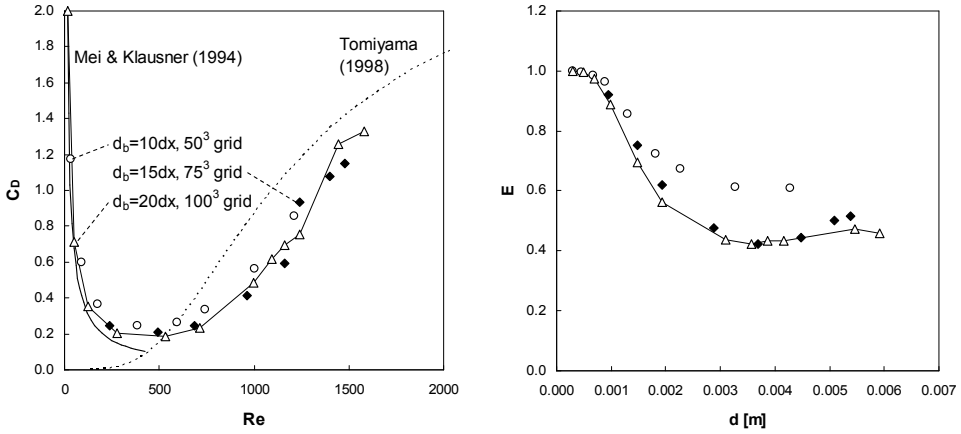


**Figure 3.6:** Drag force coefficient and bubble aspect ratio at different resolutions for a single air bubble in water.

## 3.3.2 Time-step dependency

It is well-known from literature that large bubbles can exhibit complex shape oscillations. Our simulations have shown that it may take no less than two seconds of simulation time for the bubble to reach its final state, meaning that simulation times of up to three seconds are necessary. Therefore, larger time-steps are desired, in order to limit the wall-time required. The effect of increasing the time-step tenfold ($10^{-4}$ vs. $10^{-5}$ s) will be shown here as an illustration, for a 10 mm air bubble in liquid IV. Fig. 3.7 shows that the only difference is a small shift of the results, which is caused by a slightly larger bubble volume-loss at the smaller time-step (although still acceptably small for both cases), due to the higher number of bubble translations.

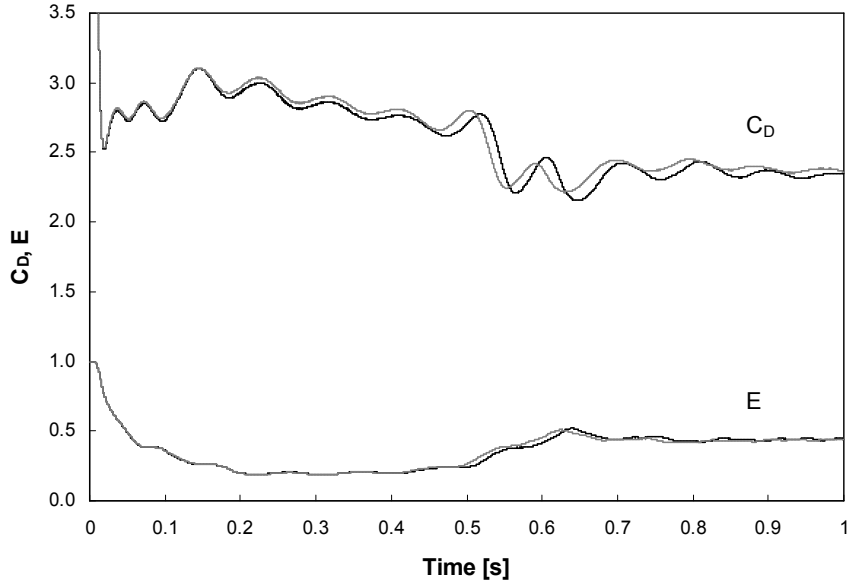


**Figure 3.7:** Drag coefficient ($C_D$) and bubble aspect ratio (E) for a 10 mm air bubble in a moderately viscous liquid (IV), using two different time-steps ($10^{-4}$, grey line; $10^{-5}$, black line). The only difference is a small lag for the smallest time-step, associated with the slightly larger bubble volume-loss.

### 3.3.3 Effect of initial condition

The influence of the initial condition has been checked by simulating a 10 mm air bubble in liquid IV, using prolate and oblate ellipsoids as a starting condition, instead of the regular sphere. Fig. 3.8 shows that during the initial bubble deformation there are differences in both the shape and drag force, which disappear quickly after only 0.1 second. Then after 0.4 seconds the transition to path instability sets in, which takes place in three distinctly different ways. However, the final state is identical and therefore it can be concluded that the initial condition has no effect on the steady-state drag force or bubble shape.

## 3.4 Results

This paragraph shows the results of the experiments and numerical simulations of a single air bubble rising in different liquids. First of all, the numerical results for the drag force on bubbles are compared to the existing correlations and experiments in ultrapure liquids. Secondly, the effect of contaminants is highlighted, using our experiments ('contaminated' liquid) and finally the differences in bubble shapes are pointed out.

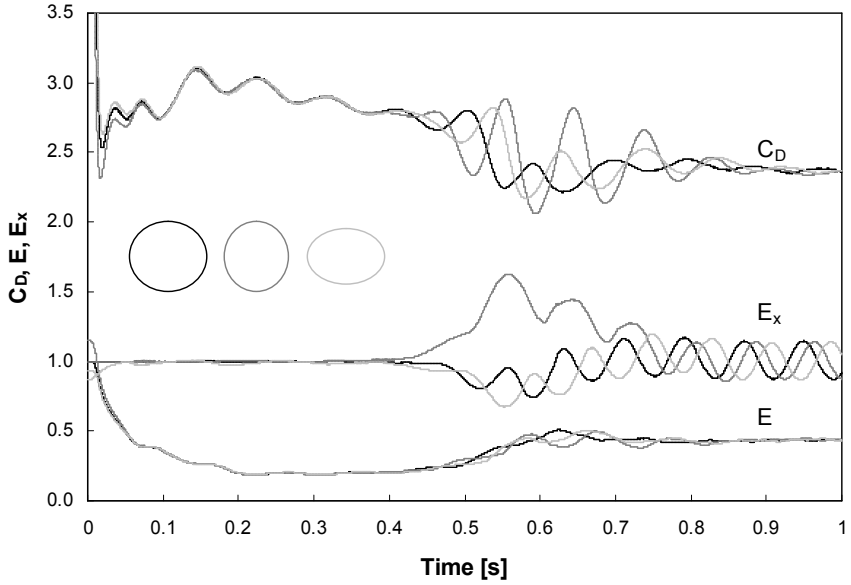


**Figure 3.8:** Drag coefficient ($C_D$), horizontal ($E_x$) and vertical aspect ratio (E) for a 10 mm air bubble in a moderately viscous liquid (IV), using different initial bubble shapes.

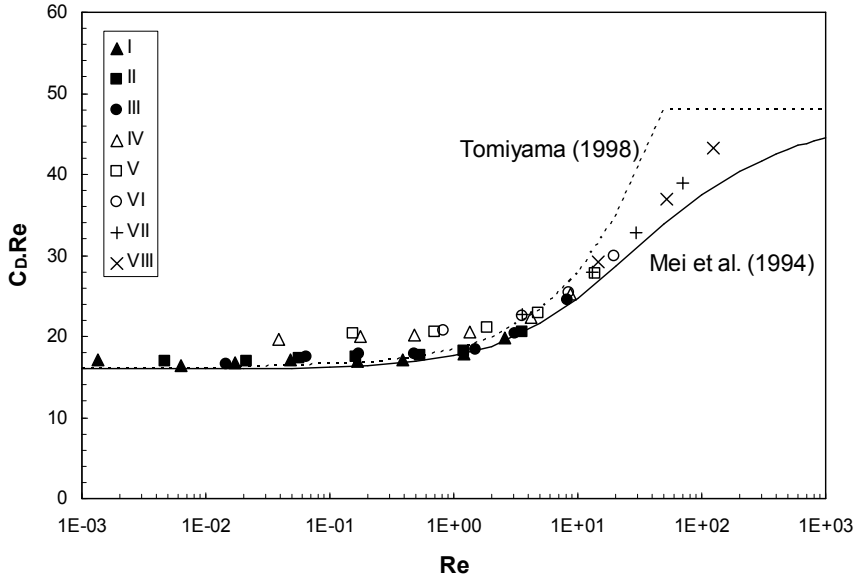


**Figure 3.9:** Drag coefficient multiplied by the Reynolds number for (nearly) spherical bubbles (E>0.95) in 'pure' liquids.

### 3.4.1 Drag force for pure liquids

First, the results for spherical bubbles in pure liquids are compared to the popular drag correlations by Mei et al. (Eq. 3.5) and Tomiyama (Eq. 3.6). Fig. 3.9 shows that the numerical simulations match closely with the correlation by Mei et al., which differs from the correlation proposed by Tomiyama at higher Reynolds numbers, due to the fact that it gives a smooth transition between both asymptotic solutions for low and high Reynolds numbers. The simulations overestimate the drag force slightly at higher Reynolds numbers, which is most likely caused by a combination of bubble deformation and wall-effects in the computational domain.

For deformed bubbles the drag force coefficient can be correlated with the Eötvös number. All simulations show a smooth transition when going from spherical to deformed bubbles, which is confirmed by experiments using ultrapurified liquids (Duineveld, 1994; Veldhuis, 2007). To achieve this, it is proposed to combine the Reynolds and Eötvös dependent parts of the drag closure as follows:

$$C_D = \sqrt{C_D\left(\mathrm{Re}\right)^2 + C_D\left(Eo\right)^2} \qquad \text{(pure)} \qquad (3.11)$$

The Reynolds dependent part, which can be well described by the correlation, proposed by Mei et al. (see Fig. 3.9) can now be subtracted and the remaining Eövös dependent part of the drag force is fitted using a simple equation. Fig. 3.10 shows that there is a significant difference between the correlation by Tomiyama (Eq. 3.6) and our fit (Eq. 3.12), especially at low Eötvös numbers. This difference is more clearly shown in Fig. 3.11 for air bubbles in water, where the correlation by Tomiyama consistently overestimates the drag force for Reynolds numbers above 500. Secondly, it can be seen that there is a very good agreement between the experiments in ultrapurified water (Duineveld, 1994; Veldhuis, 2007), the FT simulations and the newly proposed correlation.

$$C_D(Eo) = \frac{4Eo}{Eo + 9.5} \qquad \text{(pure liquids)} \qquad (3.12)$$

For sufficiently large bubbles in the less viscous liquids, zigzagging and helical path instabilities were observed in the results of the numerical simulations (Table 3.5). Fig. 3.12 shows an example of the zigzagging and helical motion of air bubbles in water. Since the path instability is very subtle and the selected numerical domain was only five bubble diameters wide, it cannot be excluded that the results may have been somewhat affected by the free-slip boundary conditions. Nevertheless, it would be interesting to study these phenomena in more detail using DNS. However, this study is outside the scope of this thesis.

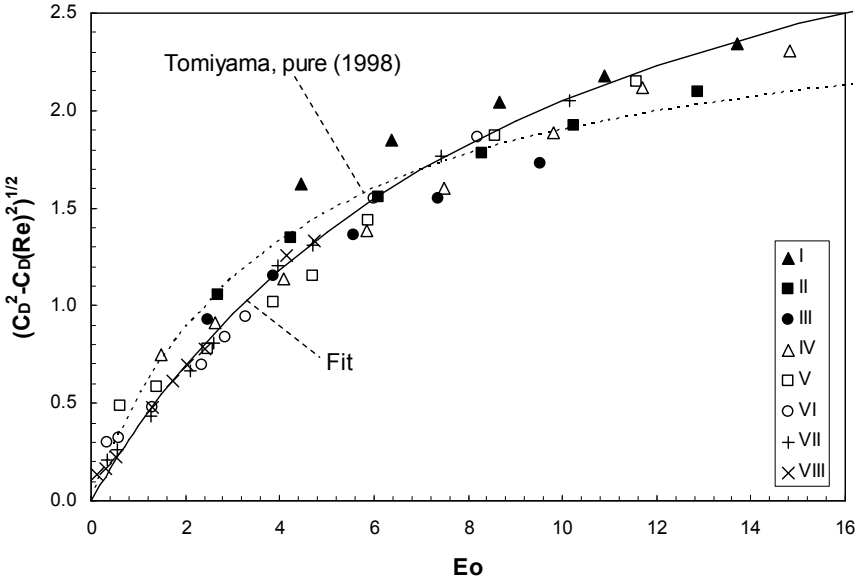


**Figure 3.10:** Eötvös dependent part of the drag coefficient for deformed bubbles in 'pure' liquids (E<0.95).

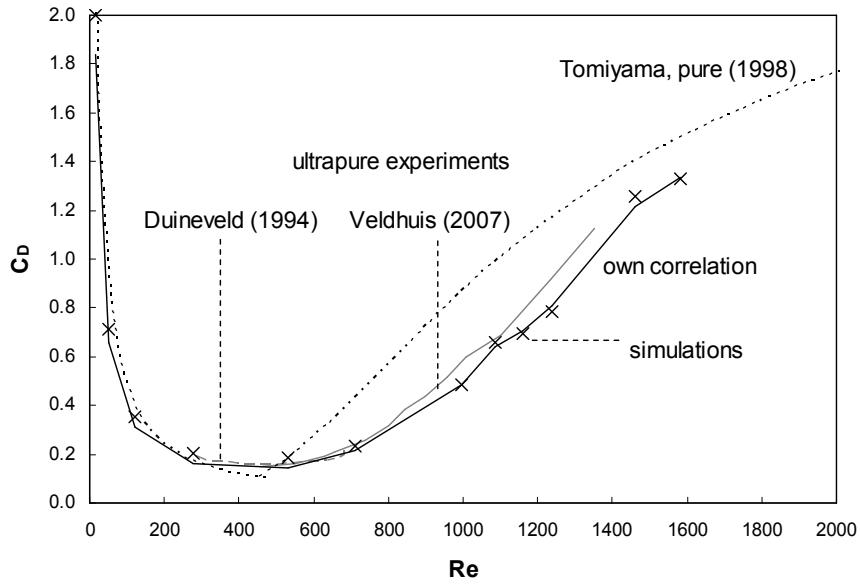


**Figure 3.11:** Drag coefficient versus Reynolds number for air bubbles rising in ultrapurified water.

**Table 3.5:** Classification of path instabilities obtained with DNS.

| Liquid | d [mm] | Path |
|---|---|---|
| IV | 8-10 | Helix |
| V | 6-9 | Helix |
| VI | 5-6 | Zigzag |
| | 7-8 | Helix |
| VII | 1.5-3 | Helix |
| | 4-6 | Zigzag |
| | 7-9 | Helix |
| VIII | 1.5-3 | Chaotic |
| | 3.5-5 | Helix |
| | 6 | Zigzag |
| | 7 | Helix |

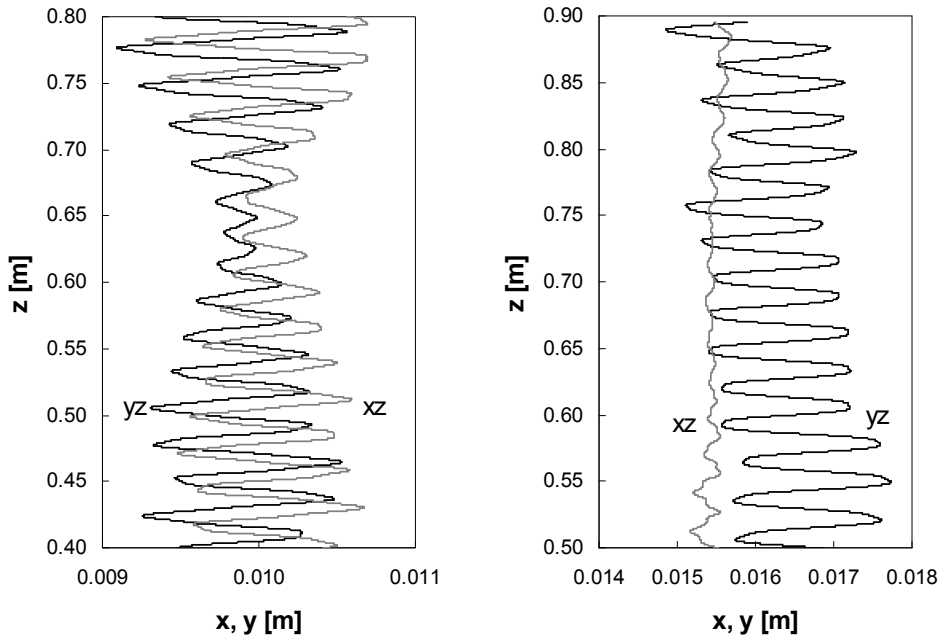


**Figure 3.12:** Bubble trajectory for a helical (left) and zigzagging path instability (right) of 4 and 6 mm air bubbles in water.

## 3.4.2 Influence of contaminants

Now that the drag force for bubbles in ultrapure liquids has been clarified, the influence of contaminants is studied using experiments. Due to the presence of a moving belt (see Chapter 4) and PIV tracer particles in the liquid, these experiments can definitely be classified as fully contaminated.

First of all, the drag coefficient is plotted versus the Reynolds number for (nearly) spherical bubbles (Fig. 3.13), showing a good agreement with the modified Stokes law (Eq. 3.2). Only the results for air bubbles in water deviate somewhat and show a significant amount of scatter. It should be stressed here that this scatter is quite common for experiments with the contaminated air-water system and the results are well within the range of rise velocities obtained by Tomiyama (2004).

Secondly, the remaining experimental data for deformed bubbles (E<0.95) are compared as a function of the Eötvös number in Fig. 3.14. It can be seen that on average the drag force coefficient determined from our experiments is somewhat higher than the predictions by Tomiyama (Eq. 3.7) and the DNS-based correlation, which may be related to the influence of contaminations.

To show that it is possible to obtain a good agreement between experiments and numerical simulations, a separate set of measurements has been carried out using a fresh batch of glycerine mixed with demineralised water. Also larger and smaller nozzles have been used in these experiments, so that the bubble diameter could be varied over a much larger range. Fig. 3.15 shows that the smallest experimental bubbles correlate better with the contaminated line, but slightly larger bubbles already overcome the effect of contaminations and show a good agreement with the numerical simulations.

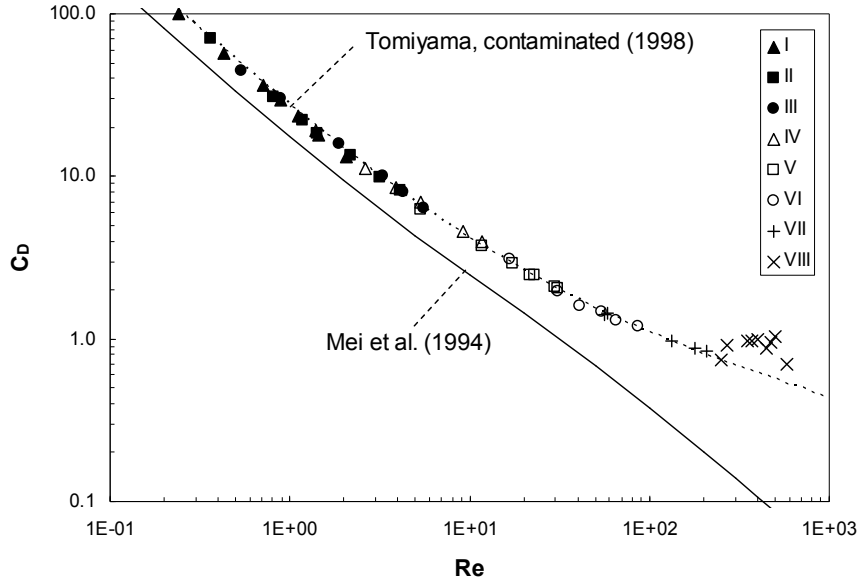


**Figure 3.13:** Drag coefficient versus Reynolds number for (nearly) spherical bubbles (E>0.95) for 'contaminated' liquids.

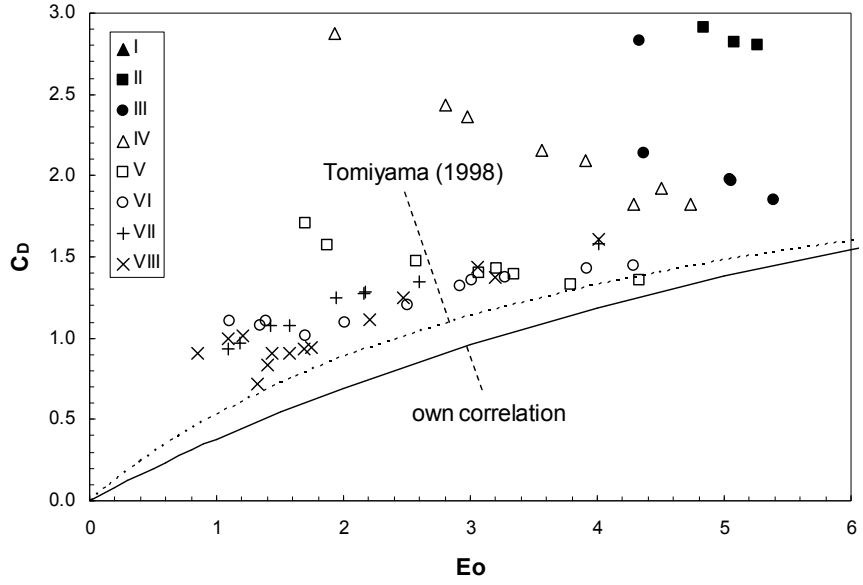


**Figure 3.14:** Contaminated drag coefficient versus Eötvös number for deformed bubbles (E<0.95).

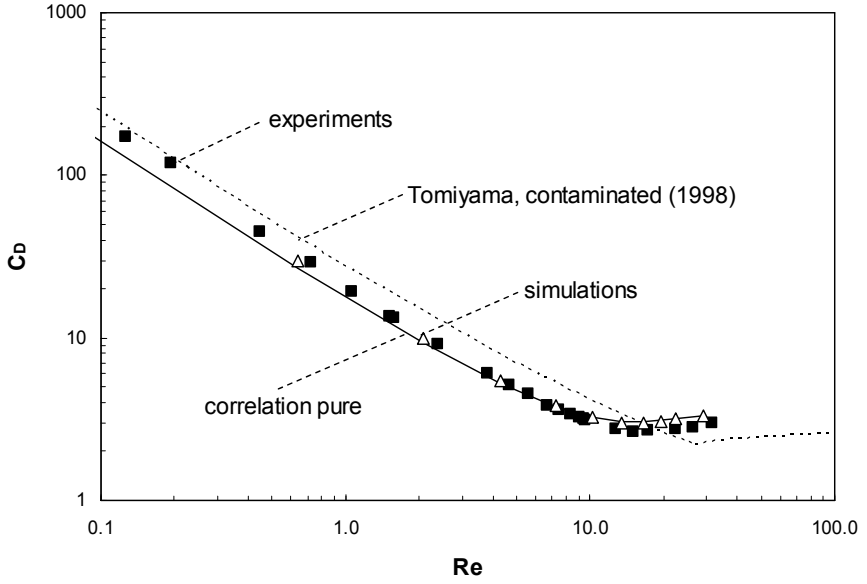


**Figure 3.15:** Drag coefficient versus Reynolds number for a relatively pure viscous liquid (η=0.110 Pa·s).

Finally, the difference in the drag force for the important air-water system is highlighted (Fig. 3.16), showing that contaminations can lead to a drag force coefficient that is up to a factor of seven higher. Now that the effect of contaminants have been outlined, unfortunately it is not yet possible to link DNS results to real-life liquids, since there is no clear way of measuring the amount and type of contaminants and it is not even totally clear how the contaminants affect the flow conditions at the bubble interface. This should definitely be studied in future research, so that the current results can be extended to systems relevant in industrial environments.

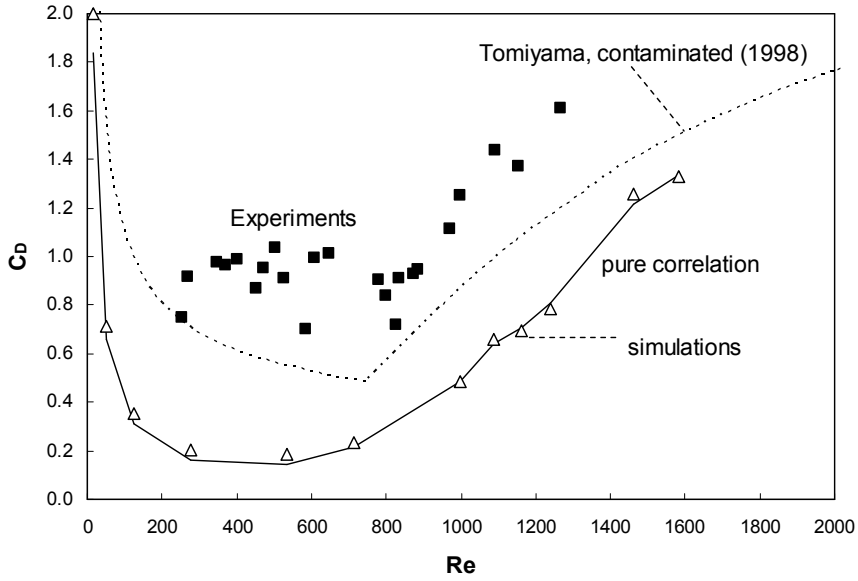


**Figure 3.16:** Drag coefficient versus Reynolds number for air bubbles rising in water.

### 3.4.3 Bubble shape

The bubble shape can be characterized quantitatively using the bubble aspect ratio:

$$E = \frac{d_v}{d_h} = \frac{d_z}{\sqrt{d_x d_y}} \tag{3.13}$$

It can be seen that in the numerical simulations (Fig. 3.17, left) the bubbles become more deformed at smaller bubble diameters when the viscosity of the liquid decreases (going from liquid I to VIII). From the simulations it follows that at an aspect ratio of about 0.4 there is a minimum in the aspect ratio, after which the aspect ratio increases again. For bubbles in a viscous liquid this coincides with the transition to spherical cap bubbles, while for the less viscous liquids this is related to the wobbling motion of bubbles.

While the aspect ratio in the experiments (Fig. 3.17, right) resembles the numerical results for the most viscous liquid (I), the bubble deformation is clearly smaller for the less viscous liquids. This difference may be explained by the significantly lower rise velocity of contaminated bubbles, thereby giving a lower deformation.
A quantitative comparison between the bubble shapes for a viscous liquid (Fig. 3.18), shows that, overall, there is a good agreement between our experiments and numerical simulations. The larger bubbles in the simulations are slightly less deformed than was observed in the experiments, which is attributed to the relatively narrow computational domain (5 bubble diameters).

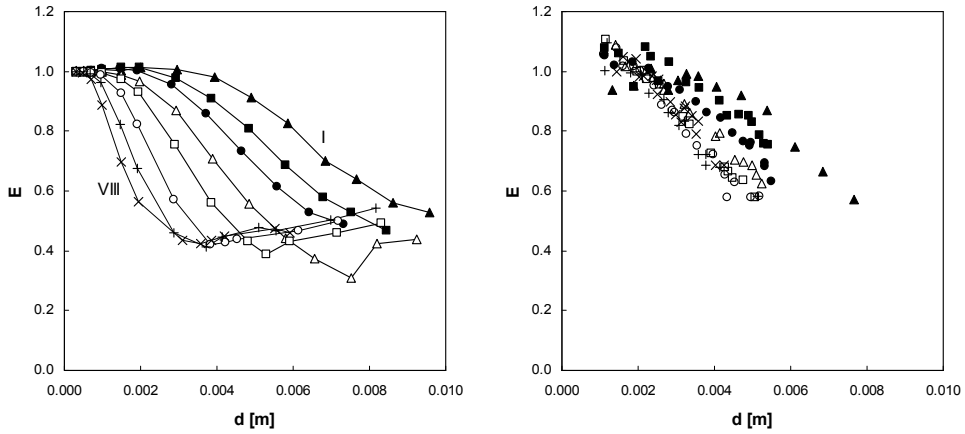


**Figure 3.17:** Aspect ratio versus bubble diameter for the numerical simulations (left) and the experiments (right).

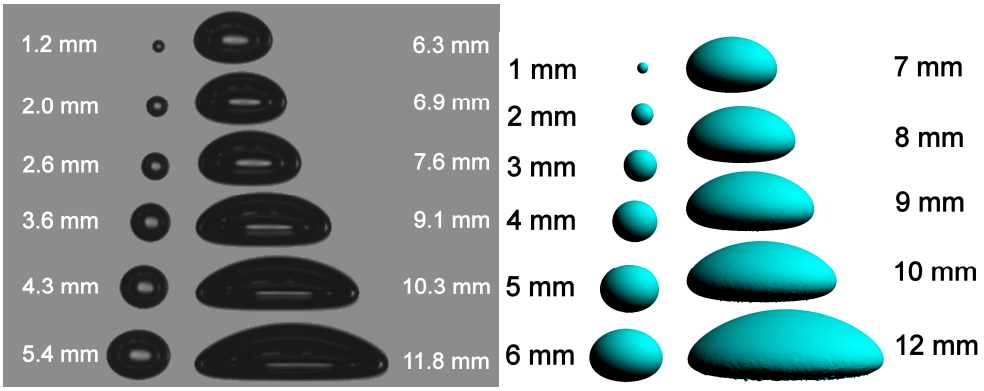


**Figure 3.18:** Measured (left) and computed (right) images of bubbles of different sizes in a relatively pure viscous liquid (η=0.110 Pa·s).

## 3.5 Conclusions

The drag force on single air bubbles rising in initially quiescent liquids ranging from dilute glycerine to water has been studied using DNS and experiments. Numerical simulations show a good agreement with existing drag closures for spherical bubbles in 'pure' liquids, however for deformed bubbles there is a large discrepancy with the popular closure by Tomiyama (1998). Therefore, a new drag closure – valid for both spherical and deformed bubbles – has been proposed that matches very well with the simulations and experiments in ultrapure liquids. Finally, it has been shown that the FT model is capable of predicting subtle path instabilities that occur for bubbles in low viscosity liquids (i.e. water).

Experiments have been carried out and the overall trend is a higher drag force than for pure systems, attributed to contaminants. For viscous liquids there is a good agreement with (pure) numerical simulations, but for less viscous liquids (i.e. water) the drag force coefficient can be up to a factor of seven higher. Secondly, in these low viscosity liquids a bubble of the same diameter can rise at different velocities, which gives a large scatter in the measured drag coefficient. Finally, it can be concluded that bubbles in contaminated systems are much less deformed, which may be explained by the lower rise velocity.

## Symbols

| | | |
|---|---|---|
| $A$ | Cross-sectional area of the bubble | $m^2$ |
| $C$ | Coefficient | - |
| $d$ | Equivalent bubble diameter | m |
| $E$ | Bubble aspect ratio | - |
| $Eo$ | Eötvös number ( $Eo = g\left(\rho_L - \rho_G\right)d^2\sigma^{-1}$ ) | - |
| $F$ | Force | N |
| $g$ | Gravitational constant | $m{\cdot}s^{-2}$ |
| $h$ | Height | m |
| $Mo$ | Morton number ( $Mo = g\eta_L^4\left(\rho_L - \rho_G\right)\rho_L^{-2}\sigma^{-3}$ ) | - |
| Re | Reynolds number ( $\mathrm{Re} = \rho_L\left\|\mathbf{v}-\mathbf{u}\right\|d\eta_L^{-1}$ ) | - |
| $t$ | Time | s |
| $w$ | Width | m |
| $v, \mathbf{v}$ | Bubble velocity | $m{\cdot}s^{-1}$ |
| $V$ | Bubble volume | $m^3$ |
| $u, \mathbf{u}$ | Continuous phase velocity | $m{\cdot}s^{-1}$ |
| $\Delta x$ | Grid spacing | m |
| $\mu$ | Viscosity | Pa·s |
| $\rho$ | Density | $kg{\cdot}m^{-3}$ |
| $\sigma$ | Surface tension coefficient | $N{\cdot}m^{-1}$ |

Subscripts:

| | |
|---|---|
| $B$ | Buoyancy |
| $D$ | Drag force |
| $G$ | Gas phase |
| $h$ | Horizontal direction |
| $L$ | Liquid phase |
| $v, z$ | Vertical direction |
| $x, y$ | Horizontal directions |

## References


1. N.G. Deen, M. Van Sint Annaland and J.A.M. Kuipers, Multi-scale Modeling of Dispersed Gas-Liquid Two-Phase Flow, *Chem. Eng. Sci.* **59** (2004), 1853-1861.
2. P.C. Duineveld, Bouncing and coalescence of two bubbles in water, Ph.D. thesis, University of Twente, The Netherlands (1994).
3. J. Hadamard, Movement permanent lent d'une sphere liquide et visqueuse dans un liquide visqueux, *Comptes Rendus* **152** (1911), 1735.
4. V.G. Levich, Bubble motion at high Reynolds numbers. *Zh. Eksp. Teoret. Fiz.* **19** (1949), 18-24.
5. J. Magnaudet and I. Eames, The Motion of High-Reynolds-Number Bubbles in Inomogeneous Flows, *Ann. Rev. Fluid Mech.* (2000), 659-708.
6. R. Mei, C.J. Lawrence and J.F. Klausner, A note on the history force on a spherical bubble at finite Reynolds number. *Phys. Fl.* **6** (1994), 418-420.
7. D.W. Moore, The boundary layer on a spherical gas bubble, *J. Fluid Mech.* **16** (1963), 749-766.
8. W. Rybcszynski, Über die fortschreitende Bewegung einer flüssigen Kugel in einem zähen Medium, *Bull. Acad. Sci. Cracovie A* **40** (1911).
9. G.G. Stokes, On the effect of the internal friction of fluids on the motion of pendulums, *Trans. Camb. Phil. Soc.* **9**, Part II (1851), 8-106.
10. A. Tomiyama, I. Kataoka, I. Zun, T Sakaguchi, Drag Coefficients of Single Air bubbles under normal and micro gravity conditions, *JSME Int. J. Series B* **41** (1998), 472-479.
11. C. Veldhuis, Leonardo's Paradox: Path and Shape Instabilities of Particles and Bubbles. Ph.D. thesis, University of Twente, The Netherlands (2007).

# 4

# Lift force


## Abstract

This chapter deals with the lift force, which is known to be responsible for the segregation of small and large (deformed) bubbles in bubbly flows through pipes and bubble columns. Both numerical simulations using the improved FT model and experiments have been performed for air bubbles rising through water/glycerine mixtures, where the bubble diameter, liquid viscosity and linear shear rate were varied. The numerical simulations show a good agreement with the correlation by Legendre and Magnaudet (1998) for spherical bubbles at sufficiently high Reynolds numbers. For large deformed bubbles a good agreement with the correlation by Tomiyama (2002) was found, although the computed lift force was always slightly lower. Finally, it was shown that the shear rate has no influence on the drag and lift coefficient.

An experimental set-up (similar to the one used by Tomiyama) was constructed using a running belt submerged in a liquid, consisting of a glycerine-water mixture of varying viscosity. PIV measurements have been used to calibrate the linear shear field and to obtain the flow profile around the bubbles. Contrary to the numerical simulations, the experimental data show a very strong influence of the shear rate on the lift force coefficient. This may be attributed to the rigid behaviour of the contaminated bubble surface, which changes the shear stress at the bubble interface.

## 4.1 Introduction

This chapter focuses on the lift force, which is responsible for segregation of small and large bubbles in bubbly flows through pipes and bubble columns: small spherical bubbles move to the wall, while large deformed bubbles move towards the core region (Fig. 4.1). It has been demonstrated numerically (Legendre & Magnaudet, 1998) that for spherical bubbles at low Reynolds numbers, the lift force results from both viscous and pressure effects. For spherical bubbles at high Reynolds numbers, the pressure effect dominates and the sign of the lift force coefficient is positive. On the other hand, for large deformed bubbles it is well-known that the sign of the lift force coefficient becomes negative. Very little is known about the mechanism of this lift inversion, which may be caused by a combination of effects related to the bubble shape, its orientation and modification of the wake structure.

In this paragraph, first the most important lift force correlations from literature are described and their applicability is discussed. Secondly, based on a force balance for a discrete bubble in a shear flow, equations are derived to obtain the drag and lift force coefficients. In the remainder of this chapter, the experimental set-up and numerical aspects are described, followed by a combined description of the results.

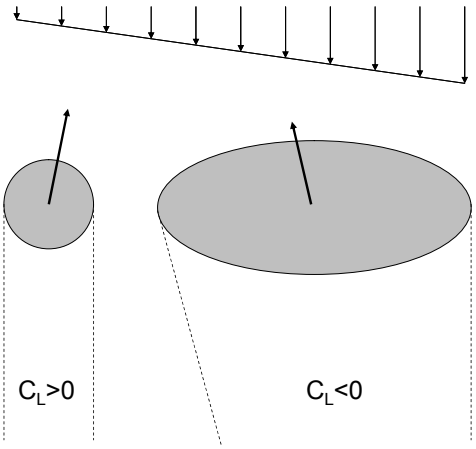


**Figure 4.1:** Two limiting cases of the lift force: small spherical bubbles move to the high negative velocity side, while large deformed bubbles move in the opposite direction.

### 4.1.1 Existing lift correlations

Equations for the lift force for the two limiting cases of low and high Reynolds numbers have been analytically derived for spherical bubbles. Saffman (1965) was the first to derive an expression for the lift force acting on a slowly rotating sphere in the limit of zero Reynolds number and infinite shear ratio (Sr). This result was extended to arbitrary shear rates by McLaughlin (1991), which allows it to be used for practical purposes (Eq. 4.1). It can be seen that the lift coefficient at low Reynolds numbers is strongly dependant on both the Reynolds number (Re) as well as the shear ratio (Sr).

$$C_L = 1.37 \frac{J(\mathrm{Re}, Sr)}{\sqrt{\mathrm{Re}\, Sr}} \qquad \mathrm{Re} << 1 \qquad (4.1)$$

$$\mathrm{Re} = \frac{\rho |\mathbf{v} - \mathbf{u}| d}{\eta} \qquad (4.2)$$

$$Sr = \frac{\omega d}{|\mathbf{v} - \mathbf{u}|} \qquad (4.3)$$

Mei & Klausner (1994a) showed – using the same methodology as McLaughlin – that the lift force for a bubble is simply 2/3rd of that of a rigid particle. Unfortunately, Legendre & Magnaudet (1997) found an error in their derivation and derived that the lift force coefficient for a bubble should be 4/9th of the rigid sphere solution:

$$C_L = \left(\frac{2}{3}\right)^2 C_{L,McLaughlin} = \frac{6}{\pi^2} \frac{J(\mathrm{Re}, Sr)}{\sqrt{\mathrm{Re}\, Sr}}$$
$$J(\mathrm{Re}, Sr) = \frac{2.255}{\left(1 + 0.2 \frac{\mathrm{Re}}{Sr}\right)^{3/2}} \qquad \mathrm{Re} << 1 \qquad (4.4)$$

At the high Reynolds limit, Auton (1987) showed that the lift coefficient of a spherical bubble or particle is equal to a constant value of 1/2. Legendre & Magnaudet (1998) bridged the gap between these two limiting analytical solutions (Eq. 4.5) by simulating spherical bubbles in a weak linear shear field at Reynolds numbers between 0.1 and 500. Especially the low Reynolds limit proved to be very challenging, because of the strong influence of the size o the computational domain. Their empirical correlation reduces to the analytical solutions at both extremes and is valid for all Reynolds numbers.

$$C_L = \sqrt{\left(\frac{6J(\mathrm{Re}, Sr)}{\pi^2 \sqrt{\mathrm{Re}\, Sr}}\right)^2 + \left(\frac{1}{2} \frac{\mathrm{Re} + 16}{\mathrm{Re} + 29}\right)^2} \qquad Sr << 1 \qquad (4.5)$$

Results for the lift force on deformed bubbles on the other hand are extremely scarce, since the level of complexity increases substantially. Analytically, the analysis by Auton was extended to ellipsoidal bubbles moving along their minor axis by Naciri (1992), who found a positive lift coefficient, demonstrating that deformation by itself does not change the direction of the lift force.

Experimentally, the most significant work has been carried out by Tomiyama et al. (2002), who used a linear shear field in viscous liquids ($10^{-5.5} < \mathrm{Mo} < 10^{-2.8}$). The corresponding closure for the lift force (Eq. 4.6) is based on a modified Eötvös number

(Eq. 4.7) and reduces to zero for very small bubbles. Hibiki & Ishii (2007) combined the experimental data by Tomiyama et al. with Eq. 4.5, aiming at extending the range of applicability of this correlation (Eq. 4.8). Unfortunately, in their paper they have to conclude that there is no literature data available to test the validity at higher Reynolds numbers (i.e. air-water system).

$$C_L = \begin{cases} MIN\left(0.288\tanh\left(0.121\,\mathrm{Re}\right), f\left(Eo_H\right)\right) & Eo_H < 4 \\ f\left(Eo_H\right) = 0.00105Eo_H^3 - 0.0159Eo_H^2 - 0.0204Eo_H + 0.474 & 4 \le Eo_H < 10.7 \end{cases} \tag{4.6}$$

$$Eo_H = \frac{\left(\rho_l - \rho_g\right) g d_H^2}{\sigma} \tag{4.7}$$

$$C_L = \left[2 - \exp\left(0.136Eo^{1.11}\right)\right] \sqrt{\left(\frac{6J\left(\mathrm{Re}, Sr\right)}{\pi^2\sqrt{\mathrm{Re}\,Sr}}\right)^2 + \left(\frac{1}{2}\frac{\mathrm{Re}+16}{\mathrm{Re}+29}\right)^2} \qquad 3.68 \le \mathrm{Re} \le 78.8 \tag{4.8}$$

Numerically, Bothe et al. (2006) obtained lift coefficients slightly lower than predicted by the correlation by Tomiyama, using similar viscous liquids. Secondly, they conclude by cubic extrapolation that the lift force coefficient at low Eötvös numbers approaches 0.5, which is the analytical solution for a spherical bubble at high Reynolds numbers. It would be interesting to see whether the lift coefficient also approaches ½ for the case of a much lower viscosity liquid (i.e. water). For more viscous liquids, there should be no limiting value for the lift coefficient, as it depends strongly on the Reynolds number (Eq. 4.5).

### 4.1.2 Derivation of the force coefficients

The drag and lift coefficients for a bubble in a linear shear flow (Fig. 4.2) can be obtained from a steady-state force balance (Eq. 4.9), including buoyancy ($\mathbf{F}_B$), drag ($\mathbf{F}_D$) and lift ($\mathbf{F}_L$) forces. A spherical-equivalent bubble diameter is used, so that the resulting closures can be applied without any additional equations, such as e.g. for the actual bubble shape.

$$\begin{aligned} 0 &= \mathbf{F}_B + \mathbf{F}_D + \mathbf{F}_L \\ 0 &= V\left(\rho_L - \rho_G\right)\mathbf{g} - C_D A\frac{\rho_L}{2}\left|\mathbf{v}-\mathbf{u}\right|\left(\mathbf{v}-\mathbf{u}\right) - C_L V\rho_L\left(\mathbf{v}-\mathbf{u}\right)\times\left(\nabla\times\mathbf{u}\right) \\ 0 &= \frac{\pi}{6}d^3\left(\rho_L - \rho_G\right)\mathbf{g} - \frac{\pi}{8}d^2\rho_L C_D\left|\mathbf{v}-\mathbf{u}\right|\left(\mathbf{v}-\mathbf{u}\right) - \frac{\pi}{6}d^3\rho_L C_L\left(\mathbf{v}-\mathbf{u}\right)\times\left(\nabla\times\mathbf{u}\right) \end{aligned} \tag{4.9}$$

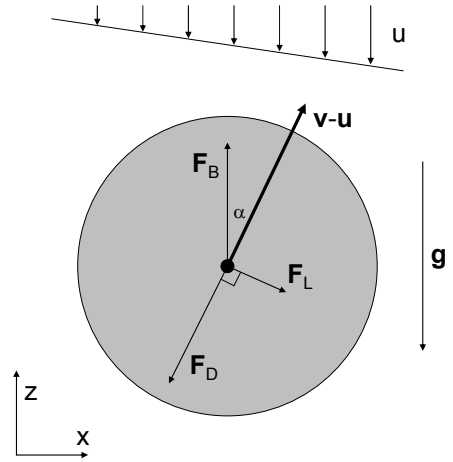


**Figure 4.2:** Force balance on a bubble rising in a linear shear field, indicating the direction of the buoyancy, lift and drag forces (in clockwise order).

For bubbles experiencing path-instability, time-averaging is necessary to compute the drag and lift coefficients. Similar to the derivation of the drag coefficient described in the previous chapter, the time-averaged forces are chosen as a basis, so that the time-averaged momentum exchange between the bubbles and the liquid phase is correct:

$$\begin{aligned} 0 &= \langle \mathbf{F}_B \rangle + \langle \mathbf{F}_D \rangle + \langle \mathbf{F}_L \rangle \\ 0 &= \frac{\pi}{6} d^3 \left(\rho_L - \rho_G\right)\mathbf{g} - \frac{\pi}{8} d^2 \rho_L C_D \left\langle \left|\mathbf{v}-\mathbf{u}\right|\left(\mathbf{v}-\mathbf{u}\right)\right\rangle - \frac{\pi}{6} d^3 \rho_L C_L \left\langle \left(\mathbf{v}-\mathbf{u}\right)\times\left(\nabla\times\mathbf{u}\right)\right\rangle \end{aligned} \tag{4.10}$$

Because the drag and lift forces are perpendicular to each other, they can easily be separated. First of all, the drag coefficient follows from the component in the direction of motion:

$$\begin{aligned} 0 &= \left(\mathbf{F}_B + \mathbf{F}_D\right)\cdot\left(\sin\alpha, 0, \cos\alpha\right) \\ 0 &= \frac{\pi}{6} d^3 \left(\rho_L - \rho_G\right) g \left\langle \cos\alpha \right\rangle - \frac{\pi}{8} d^2 \rho_L C_D \left\langle \left|\mathbf{v}-\mathbf{u}\right|\left(\mathbf{v}-\mathbf{u}\right)\right\rangle \\ C_D &= \frac{4d\left(\rho_L - \rho_G\right) g}{3\rho_L \left\langle \left|\mathbf{v}-\mathbf{u}\right|\left(\mathbf{v}-\mathbf{u}\right)\right\rangle} \left\langle \cos\alpha \right\rangle = \frac{4d\left(\rho_L - \rho_G\right) g}{3\rho_L \left\langle \left|\mathbf{v}-\mathbf{u}\right|\left(\mathbf{v}-\mathbf{u}\right)\right\rangle} \left\langle \frac{v_z - u_z}{\left|\mathbf{v}-\mathbf{u}\right|} \right\rangle \end{aligned} \tag{4.11}$$

It can be seen that this equation reduces to Eq. 3.9, when a bubble rises vertically ($\langle \cos\alpha \rangle = 1$). Secondly, the lift coefficient can be derived from the transverse component of the force balance:

$$0 = \left(\mathbf{F}_B + \mathbf{F}_L\right)\cdot\left(\cos\alpha, 0, -\sin\alpha\right)$$
$$0 = -\frac{\pi}{6}d^3\left(\rho_L - \rho_G\right)g\left\langle\sin\alpha\right\rangle - \frac{\pi}{6}d^3\rho_L C_L\frac{du_z}{dx}\left\langle\left|\mathbf{v}-\mathbf{u}\right|\right\rangle \tag{4.12}$$
$$C_L = -\frac{\left(\rho_L - \rho_G\right)g}{\rho_L\dfrac{du_z}{dx}\left\langle\left|\mathbf{v}-\mathbf{u}\right|\right\rangle}\left\langle\sin\alpha\right\rangle = -\frac{\left(\rho_L - \rho_G\right)g}{\rho_L\dfrac{du_z}{dx}\left\langle\left|\mathbf{v}-\mathbf{u}\right|\right\rangle}\left\langle\frac{v_x}{\left|\mathbf{v}-\mathbf{u}\right|}\right\rangle$$

Alternatively, the instantaneous drag and lift coefficient can be averaged, but since the relative velocity ( $\mathbf{v}-\mathbf{u}$ ) hardly fluctuates the difference is very small. This was verified for air bubbles rising in water and the absolute difference in both the drag and lift coefficient was found to be less than 0.008.

## 4.2 Experimental set-up

The experimental set-up consists of a square polycarbonate column with a steel bottom section containing a long thin tube, through which bubbles can be injected by means of two syringes (Fig. 4.3). Details about the bubble injection, physical properties and the bubble tracking can all be found in paragraph 3.2. The main difference with the set-up described in the previous chapter is the addition of a 15 cm wide running belt, which is suspended in the liquid. Its function is to generate a linear shear field, so that the lift force can be studied. A gap between the wall and the belt of 6 cm is used, twice the distance used by Tomiyama et al. (2002), in order to reduce wall-effects. The direction of the belt is such that the bubbles experience counter flow, which helps to keep them in the field of view as long as possible.

For the measurement of the velocity field, a commercial PIV set-up is used, consisting of a double-pulsed Nd-YAG laser and high-speed camera (Table 4.1). Before each set of measurements, the linear shear field is calibrated using PIV. The velocity profile across the centre of the field of view (Fig. 4.4) was analyzed every 5 seconds for 35 seconds, which yields the shear rate and its standard deviation. Different water/glycerine mixtures were used (indicated by liquids I to IV), the properties of which were measured and are listed in Table 3.2. Stable linear shear rates in the range of 1-4 $s^{-1}$ were obtained in this set-up.

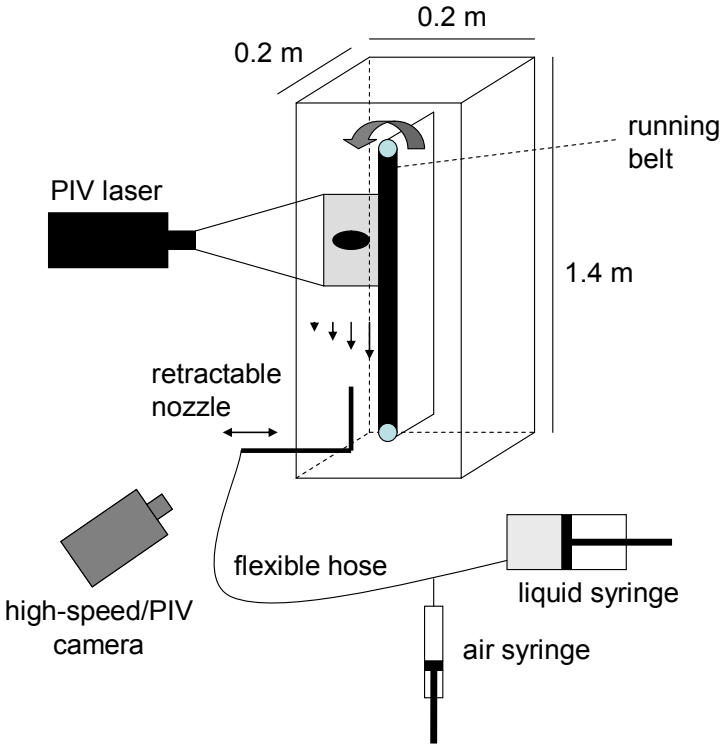


**Figure 4.3:** Schematic overview of the experimental set-up.

**Table 4.1:** Equipment used for the high-speed imaging and PIV experiments.

| Equipment | Details |
|---|---|
| Column | Polycarbonate walls, steel bottom section (0.20 x 0.20 x 1.40 m) |
| PIV laser | Double pulsed Nd-YAG laser New Wave Solo IV PIV 2*50mJ@532 nm, f=50Hz |
| Camera (both PIV and high-speed imaging) | Imager Pro HS CMOS camera<br>10 bits, 1280*1024 Pixels, Pixel size 12*12 μm<br>Max. 625 frames/s, 50 mm camera lens<br>Field-of-view: 0.068 x 0.108 m (w x h) |
| PIV tracer particles | Dantec 50 μm polyamide, 0.1 %vol |
| Backlighting (high-speed imaging) | 500 Watt halogen light and white 80 grams paper covering the back wall of the column |
| Computer | Dual Xeon 2.66 GHz<br>Programmable Timing Unit |
| PIV software | LaVision DaVis 7.1.1.44 |

**Table 4.2:** Stable linear shear rates obtained in liquids I-IV.

| Liquid | Linear shear rates [$s^{-1}$] |
|---|---|
| I | 2.0, 4.0 |
| II | 1.5, 2.0, 3.0 |
| III | 1.5, 2.0 |
| IV | 1.0 |

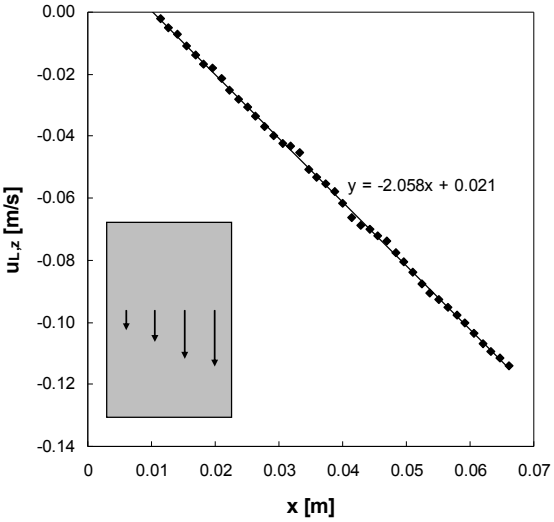


**Figure 4.4:** Example of the linear shear field calibration. The dots represent the vertical component of the velocity in the middle of the camera view. A linear fit is used to obtain the shear rate and the position of the wall.

## 4.3 Numerical aspects

The numerical simulations have been carried out with the improved FT model (see Chapter 2) using a cubic computational domain consisting of one million cells, which yields good resolution at reasonable calculation time (typically two weeks). The initially spherical bubble is placed horizontally in the center of the computational domain and a window shifting technique assures that it keeps this position. Depending on the viscosity of the liquid, the bubble diameter is equal to 15 or 20 Eulerian cells, which is the best trade-off between acceptable domain size and required resolution. The top, left and right boundaries enforce the linear shear field, using inflow and no-slip boundary conditions respectively. They are supplemented by a prescribed pressure boundary at the bottom, where the liquid is free to exit the domain, and free-slip boundaries at the front and rear.

### 4.3.1 Time-averaging

As an example, the determination of the drag and lift force coefficients from a numerical simulation is shown for an 8 mm air bubble in liquid VI. The instantaneous

drag and lift coefficient (Fig. 4.5) are used to determine the appropriate period for the time-averaging. In this particular case, the bubble takes about 0.7 seconds to move along a stable helical path, which is responsible for the periodic fluctuations in the drag and lift force. The time-averaging was carried out excluding this initial period. Because the magnitude of the oscillation ($-6 < C_L < 5$) is much larger than the average ($C_L = -0.66$), this interval is adjusted so that the time-averaging starts and stops with the bubble in the same state. Also a sufficient number of oscillation periods was used (typically 5-10), in order to give an accurate value.

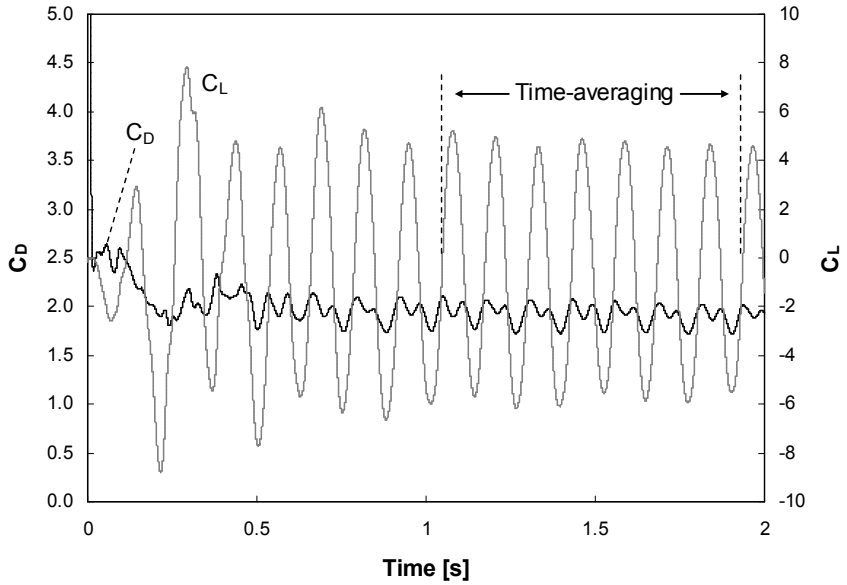


**Figure 4.5:** Example of the time-averaging of the drag and lift forces for an 8 mm air bubble in liquid VI.

## 4.3.2 Grid dependency

The influence of the domain size and interface resolution is studied by simulating two points (2 and 6 mm bubbles) of each data set using different computational grids (Fig. 4.6). Legendre and Magnaudet (1998) have shown that the lift force on a spherical bubble is very sensitive to wall effects, especially at low Reynolds numbers. For instance, at a Reynolds number of 0.1 they find that a domain size of 50 bubble diameters is still insufficient to completely exclude wall effects. Fortunately, at the same time they conclude that at these conditions the lift force is negligible compared to the drag force, which allows us to shift focus to moderate and low viscosity systems (Re>1). On the other hand, from our experience the complex interface dynamics at higher Reynolds numbers require a higher interface resolution.

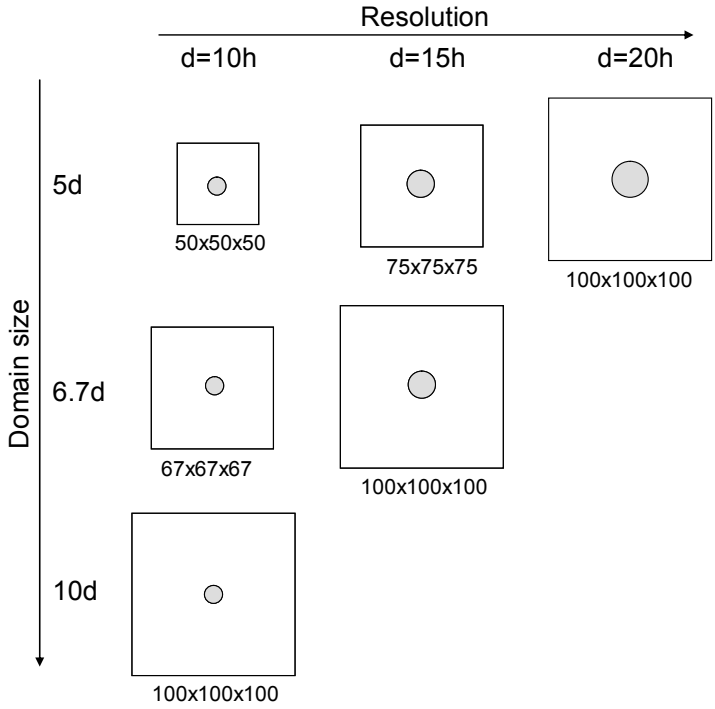


**Figure 4.6:** Simulation domains used for the lift force simulations, which are tuned to the viscosity of the liquid. Highly viscous liquids require a large domain (bottom left), while inviscid liquids require more interface resolution (top right).

First, Table 4.3 shows that for small bubbles in liquid I and II the drag and lift coefficient vary considerably when the domain size is increased (top to bottom). For less viscous liquids or larger bubbles this effect is significantly smaller because of the higher Reynolds numbers. This is more clearly demonstrated in Fig. 4.7, showing that the effect of resolution and box size wears off very quickly for larger bubbles.
Secondly, it can be observed that the effect of resolution (left to right in Table 4.3) is quite small, because of the relatively simple interface dynamics and flow profile. Nevertheless, the intermediate resolution (d=15dx) is preferred, because it gives considerably less numerical noise and errors related to volume loss.
For the three least viscous liquids (VI-VIII) it was found that the highest resolution (d=20dx) has to be used to obtain accurate results, because coarser grids give too much errors due to volume loss for the wobbling bubbles to reach a steady state. Also, the bubble shape is more accurately described when using a higher interface resolution.

**Table 4.3:** Effect of the domain size and interface resolution on the drag and lift coefficient for a bubble in a linear shear field. An asterisk (*) marks excessively noisy results.

| Liquid | d [mm] | Domain size | $C_D$ d=10h | $C_D$ d=15h | $C_D$ d=20h | $C_L$ d=10h | $C_L$ d=15h | $C_L$ d=20h |
|---|---|---|---|---|---|---|---|---|
| I | 2 | 5d | 54.5 | 55.0 | | -0.03 | -0.24 | |
| | | 6.7d | 47.5 | 48.6 | | 0.00 | 0.08 | |
| | | 10d | 42.6 | | | 0.59 | | |
| | 6 | 5d | 4.06 | 4.15 | | -0.41 | -0.46 | |
| | | 6.7d | 3.84 | 3.92 | | -0.46 | -0.50 | |
| | | 10d | 3.87 | | | -0.45 | | |
| II | 2 | 5d | 18.14 | 17.80 | | 0.40 | 0.43 | |
| | | 6.7d | 16.16 | 15.89 | | 0.58 | 0.54 | |
| | | 10d | 15.06 | | | 0.58 | | |
| | 6 | 5d | 2.45 | 2.48 | | -0.21 | -0.26 | |
| | | 6.7d | 2.35 | 2.37 | | -0.24 | -0.28 | |
| | | 10d | 2.35 | | | -0.18 | | |
| III | 2 | 5d | 7.20 | 6.82 | 6.76 | 0.36* | 0.37 | 0.40 |
| | | 6.7d | 6.59 | 6.34 | | 0.34* | 0.36 | |
| | | 10d | 6.33 | | | 0.37* | | |
| | 6 | 5d | 1.82 | 1.84 | 1.85 | -0.24 | -0.27 | -0.29 |
| | | 6.7d | 1.74 | 1.77 | | -0.23 | -0.28 | |
| | | 10d | 1.71 | | | -0.25 | | |
| IV | 2 | 5d | 3.30 | 3.05 | 2.99 | 0.33* | 0.33 | 0.33 |
| | | 6.7d | 3.12 | 2.92 | | 0.29* | 0.33 | |
| | | 10d | 3.08 | | | 0.26* | | |
| | 6 | 5d | 1.48 | 1.52 | 1.54 | -0.33 | -0.37 | -0.40 |
| | | 6.7d | 1.43 | 1.46 | | -0.30 | -0.36 | |
| | | 10d | 1.40 | | | -0.30 | | |
| V | 2 | 5d | | 1.31 | 1.26 | | 0.40 | 0.38 |
| | | 6.7d | | 1.30 | | | 0.39 | |
| | 6 | 5d | | 1.03 | 1.27 | | -0.13 | -0.36 |
| | | 6.7d | | 1.02 | | | -0.13 | |

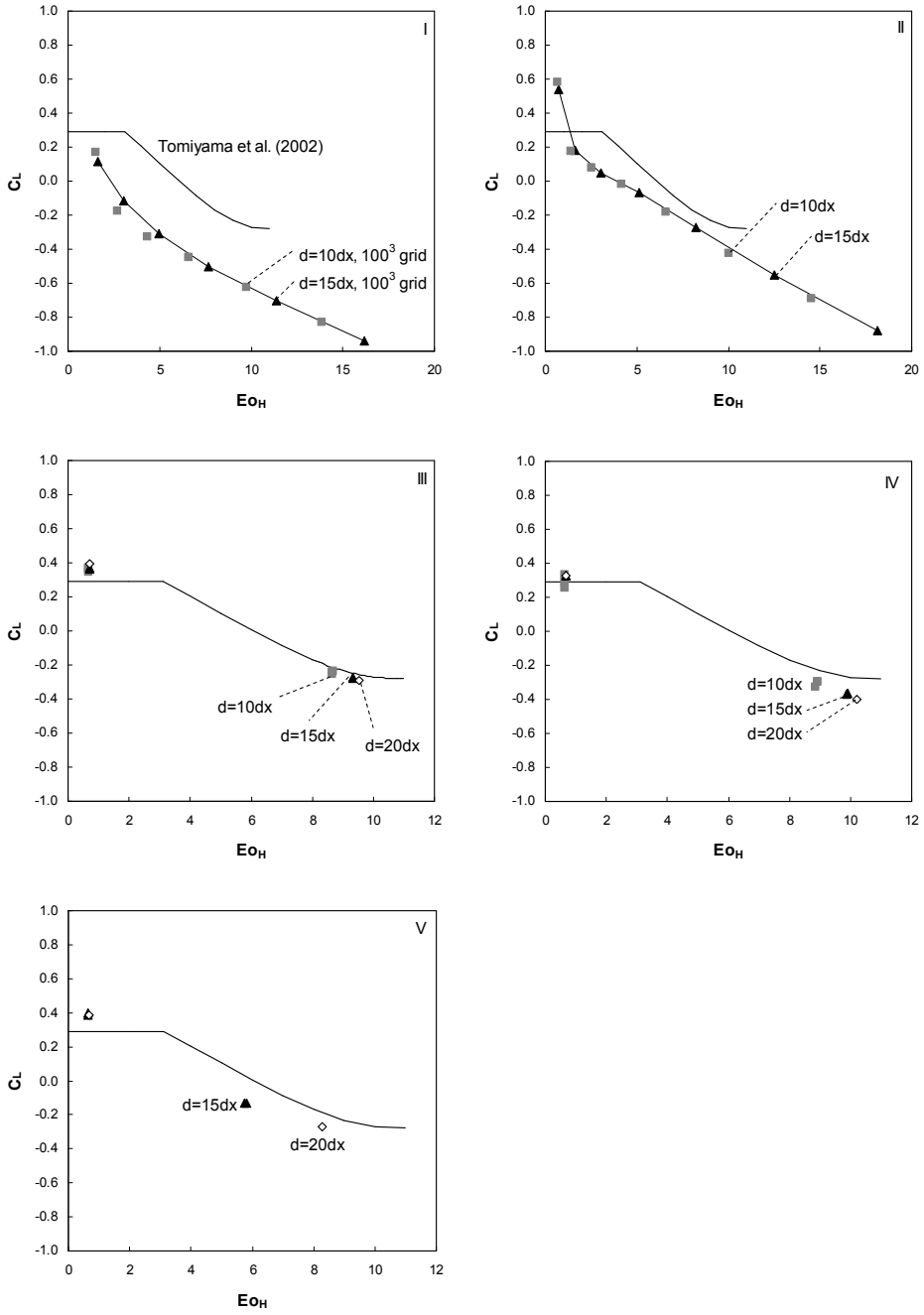


**Figure 4.7:** Lift force coefficients at different grid settings for liquid I-V (from left to right). For less viscous liquids (VI-VIII) only the finest grid (d=20dx) is used, to limit volume loss and to be able to describe complex shape oscillations. The solid line indicates the prediction by the correlation by Tomiyama et al. (2002).

## 4.4 Results

### 4.4.1 Lift force for bubbles in pure liquids

First, the influence of the linear shear field on the drag force and bubble shape is compared to the results obtained in Chapter 3 for an initially quiescent liquid. As an example, the results for the most viscous and least viscous liquids are shown in Fig. 4.8. All simulated points have been checked and it can be concluded that there is no influence whatsoever of the shear field on the drag coefficient and bubble aspect ratio, which is not surprising considering the low shear ratio (Sr<0.12) and sufficiently high Reynolds numbers (Re>1) investigated. Even when doubling the shear rate, there is still no discernible effect.

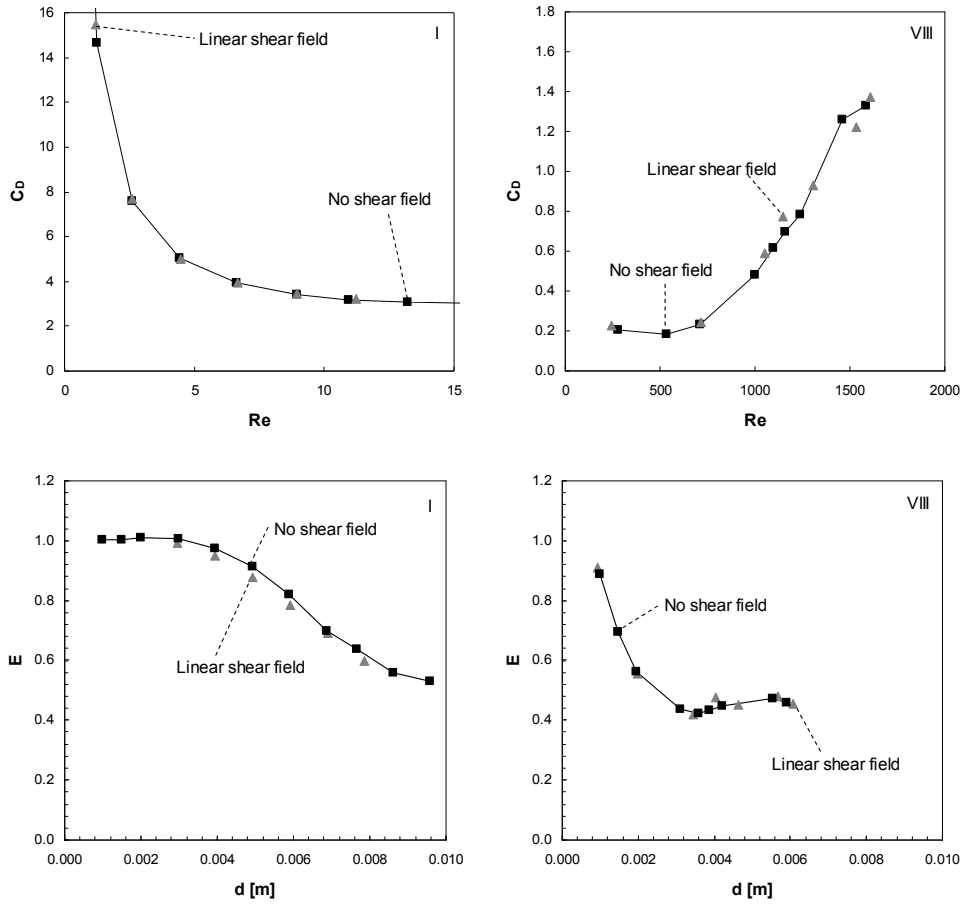


**Figure 4.8:** Drag force coefficient (top) and aspect ratio (bottom) for bubbles in the highest (left) and lowest viscosity pure liquid (right) with and without a linear shear field.

Since it is clear that the shear field does not influence the drag force, it is possible to focus on the lift force independently. Fig. 4.9 shows that for (nearly) spherical bubbles (E>0.95) there is a good agreement with the equation by Legendre & Magnaudet (1998), provided that the liquid is not too viscous (see §4.3.2). Fortunately, the lift force is relatively unimportant at low Reynolds numbers (Legendre & Magnaudet, 1998) and Eq. 4.5 works well in this region, so that these differences are not very important. Also, it can be seen that there is a significant difference with the Reynolds-dependent part of the correlation by Tomiyama et al. (2002), which is not surprising as this does not reduce to the analytical solution at neither low nor high Reynolds numbers.

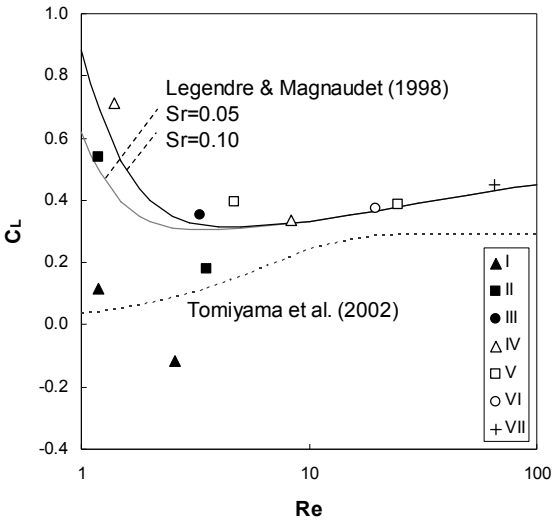


**Figure 4.9:** Lift force coefficient for spherical bubbles (E>0.95) in pure liquids in a linear shear field, showing that the simulations agree well with the correlation by Legendre & Magnaudet (1998) at higher Reynolds numbers.

For deformed bubbles, the numerical results are compared to the Eötvös-dependent part of the correlation by Tomiyama (Eq. 4.6). Fig. 4.10 shows that for the most viscous liquid (I) the simulation results are quite different from the correlation and the other simulation results, which may be related to the low Reynolds numbers, similar to the minimum of the lift force for spherical bubbles around Re=1. However, more simulations (using a very large domain size) at low Reynolds number have to be conducted in order to investigate this phenomenon further.
At similar conditions as Tomiyama used (II-IV) and beyond, a good agreement with his correlation is found, although the lift force is always slightly lower in the numerical simulations. The small scatter in the numerical data points is mainly caused by path-instability or wobbling motion of the bubbles, which cause the lift force coefficient to oscillate with very large amplitude (see Fig. 4.5). This makes a very accurate determination of its average value extremely challenging, moreover because it can take a very long time to reach a steady state.

Finally, the effect of increasing the shear rate from 2.0 to 4.0 $s^{-1}$ was determined for bubbles in 'pure' liquids. It was found that there is no influence of the shear rate on the drag and lift force coefficient, except – as expected – at very low Reynolds numbers. As an example, Fig. 4.11 shows that for liquid IV both the drag and lift force coefficients for both shear rates are very close.

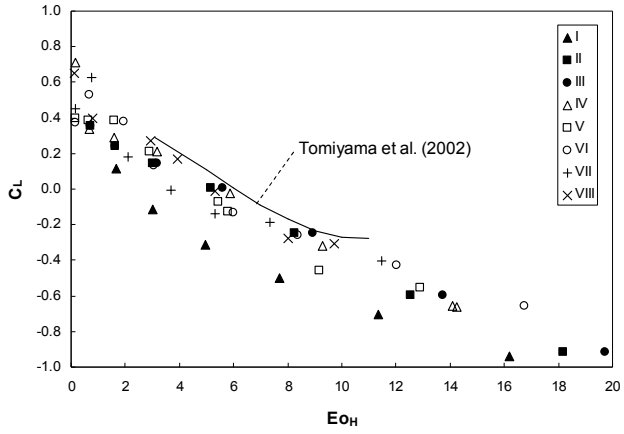


**Figure 4.10:** Lift force coefficient for pure deformed bubbles in a linear shear field at different liquid viscosities. The symbols used are identical to those in Fig. 4.9.

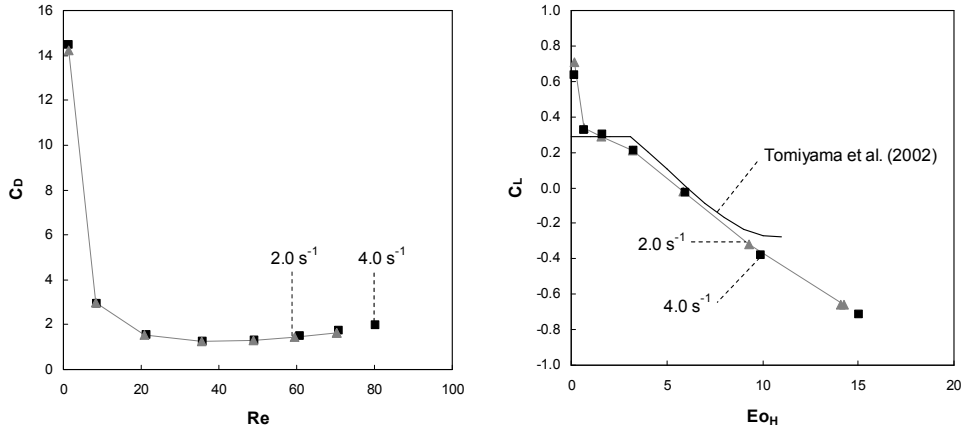


**Figure 4.11:** Influence of the shear rate (2.0 and 4.0 $s^{-1}$) on the drag and lift force coefficients for bubbles in a moderately viscous liquid (IV).

## 4.4.2 Lift force for bubbles in contaminated liquids

In the previous chapter it has been already demonstrated that the drag force measured in the experiments can strongly deviate from the results obtained from numerical simulations, attributed to contaminations affecting the slip conditions at the bubble

surface. Fig. 4.12 shows that this is also the case in the presence of a linear shear field. It can be seen that the linear shear field has no consistent effect on the drag coefficient, meaning that also the lift force for contaminated bubbles can be treated independently from the other forces. There is some scatter in the results – especially for the larger bubbles – because of disturbances during the bubble injection and fluctuations in the linear shear field. Also it was verified that the bubbles had the same aspect ratio as in the previous chapter without the linear shear field.

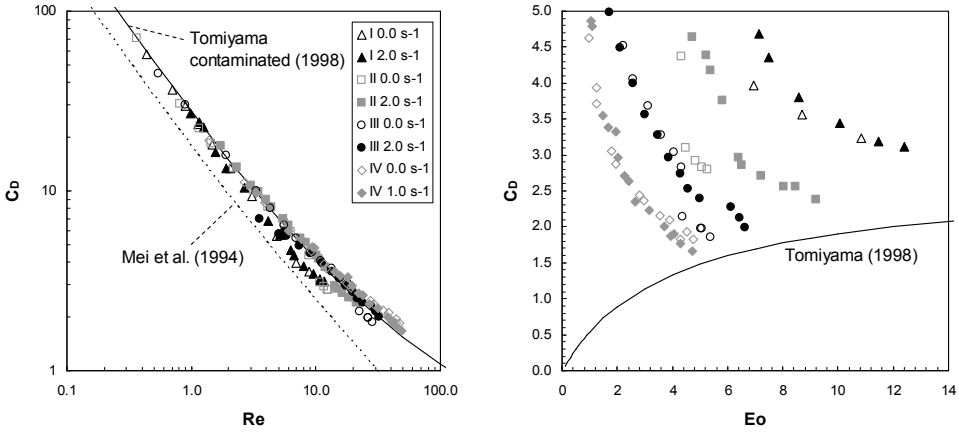


**Figure 4.12:** Drag force coefficient vs. Reynolds (left) and Eötvös numbers (right) for bubbles in a contaminated liquid. The solid and dashed lines represent the predictions by the correlations by Tomiyama (1998) and Mei et al. (1994) respectively.

Secondly, the lift force coefficient can be studied from Fig. 4.13, at different liquid viscosities and shear rates. Surprisingly, this shows that the shear rate does have an important effect on the lift force coefficient when the liquid is contaminated, which is likely related to the modified shear stress at the bubble surface.

### 4.4.3 Wake structure

From literature it was found that large deformed bubbles have a slanted wake structure, which may be a key factor in explaining the negative lift force coefficient. Fig. 4.14 shows that as soon as the lift coefficient turns negative (6 mm air bubble in liquid II) in the numerical simulations, there is still no (or hardly any) asymmetric wake structure. Only when the bubble diameter is increased to 8 mm, the slanted wake appears. On the other hand, in the experiments (Fig. 4.15) the slanted wake is already quite pronounced at a bubble diameter of 6 mm in liquid II. These discrepancies are again attributed to the effects of contaminants.

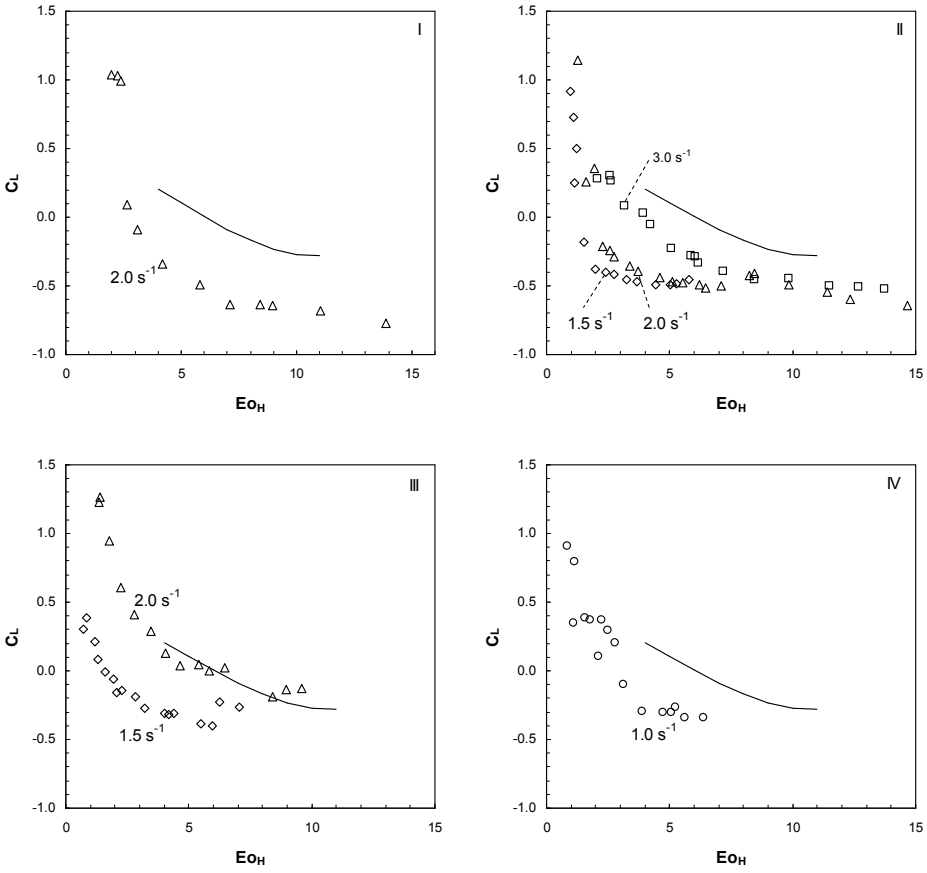


**Figure 4.13:** Lift force coefficient at different shear rates for air bubbles in contaminated liquids (I-IV).

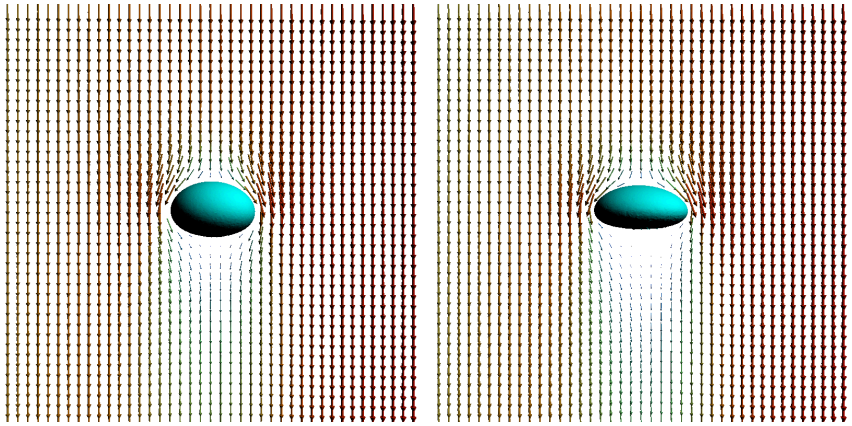

**Figure 4.14:** Flow profile around a 6 mm (left) and 8 mm (right) air bubble in liquid II, obtained from the numerical simulations. Both bubbles have a negative lift coefficient, but only the larger bubble has a slanted wake.

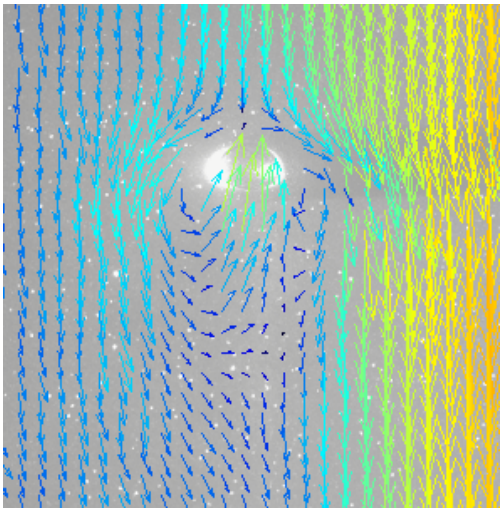

**Figure 4.15:** Flow profile around a 6 mm air bubble in liquid II, obtained using PIV from the experiments. It can be seen that the slanted wake is much more developed than in the numerical simulations.

## 4.5 Conclusions

In this chapter the lift force has been studied using numerical simulations and experiments, which represent pure and contaminated liquids respectively. The numerical simulations have been carried out at Reynolds numbers above 1, because of the very strong effect of the walls at lower Re numbers. The results show a good agreement with the correlation by Legendre & Magnaudet (1998) for spherical bubbles at sufficiently high Reynolds numbers, contradicting the Reynolds-dependent part of Tomiyama's closure (2002). For larger bubbles there is a good agreement with the correlation by Tomiyama, although the lift coefficient was consistently somewhat lower. Finally, it was shown that the shear rate has no influence on the drag and lift coefficients.

For the experiments a set-up was constructed consisting of a running belt submerged in a column of liquid. PIV measurements have been used to validate the linearity of the shear field and to calibrate the shear rate. The experimental data show that in a contaminated liquid there is a very strong effect of the shear rate on the lift force and consequently the results are totally different from the numerical simulations and experiments by Tomiyama (2002).

For future research, it is recommended to focus first on the measurement of the type and concentration level of contaminations, because currently there is no clear way of determining the extent of contaminations in the experiments. Once this is clarified, experiments can be done using different levels of contaminations, to study their effect. Also it would be worthwhile to perform some numerical simulations using the same bubble shape as in the Front Tracking simulations, but now with a rigid surface mimicking contaminated bubbles. This may prove indirectly whether the observed effects can indeed be attributed to contaminants.

## Symbols

| | | |
|---|---|---|
| $A$ | Cross-sectional area of the bubble | $m^2$ |
| $C$ | Coefficient | - |
| $d$ | Equivalent bubble diameter | m |
| $dx$ | Grid size | m |
| $Eo$ | Eötvös number ( $Eo = g\left(\rho_L - \rho_G\right)d^2\sigma^{-1}$ ) | - |
| $Eo_H$ | Horizontal Eötvös number ( $Eo = g\left(\rho_L - \rho_G\right)d_H^2\sigma^{-1}$ ) | - |
| $\mathbf{F}$ | Force | N |
| $g, \mathbf{g}$ | Gravitational constant/vector | $m \cdot s^{-2}$ |
| $h$ | Height | m |
| $J$ | Function of the Reynolds number and the shear ratio | - |
| Re | Reynolds number ( $\mathrm{Re} = \rho_L \left\|\mathbf{v} - \mathbf{u}\right\| d\eta_L^{-1}$ ) | - |
| $Sr$ | Shear ratio ( $Sr = \omega d \left\|\mathbf{v} - \mathbf{u}\right\|^{-1}$ ) | - |
| $t$ | Time | s |
| $\mathbf{u}$ | Continuous phase velocity | $m \cdot s^{-1}$ |
| $\mathbf{v}$ | Bubble velocity | $m \cdot s^{-1}$ |
| $V$ | Bubble volume | $m^3$ |
| $w$ | Width | m |
| $\alpha$ | Angle of the bubble direction of motion with the vertical normal | rad |
| $\eta$ | Viscosity | Pa·s |
| $\rho$ | Density | $kg \cdot m^{-3}$ |
| $\sigma$ | Surface tension coefficient | $N \cdot m^{-1}$ |
| $\omega$ | Shear rate | $s^{-1}$ |

Subscripts

| | |
|---|---|
| $B$ | Buoyancy |
| $D$ | Drag force |
| $G$ | Gas |
| $H$ | Horizontal |
| $L$ | Liquid, lift force |
| $x$ | Horizontal direction |
| $z$ | Vertical direction |

## References


1. T.R. Auton, The lift force on a spherical body in a rotational flow, *J. Fluid Mech.* **183** (1987), 199-218.
2. D. Bothe, M. Schmidtke and H.-J. Warnecke, VOF-Simulation of the Lift Force for Single Bubbles in a Simple Shear Flow, *Chem. Eng. Technol.* **29** (2006), 1048-1053.

3. T. Hibiki and M. Ishii, Lift force in bubbly flow systems, *Chem. Eng. Sci.***62** (2007), 6457-6474.
4. D. Legendre and J. Magnaudet, A note on the lift force on a spherical bubble or drop in a low-Reynolds-number shear flow, *Phys. Fluids* **9** (1997), 3572-3574.
5. D. Legendre and J. Magnaudet, The lift force on a spherical bubble in a viscous linear shear flow, *J. Fluid Mech.* **368** (1998), 81-126.
6. J.B. McLaughlin, Inertial migration of a small sphere in linear shear flows, *J. Fl. Mech.* **224** (1991), 261-274.
7. R. Mei, C.J. Lawrence and J.F. Klausner, A note on the history force on a spherical bubble at finite Reynolds number. *Phys. Fl.* **6** (1994), 418-420.
8. R. Mei and J.F. Klausner, Shear lift force on spherical bubbles, *Int. J. Heat and Fluid Flow* **15** (1994a), 62-65.
9. M.A. Naciri, Contribution à l'etude des forces exercées par un liquide sur une bulle de gaz: portance, masse ajouté. Ph.D. thesis, L'école Centrale de Lyon, France (1992).
10. P.G. Saffman, The lift on a small sphere in a slow shear flow, *J. Fluid Mech.* **22** (1965), 385-400.
11. A. Tomiyama, I. Kataoka, I. Zun, T Sakaguchi, Drag Coefficients of Single Air bubbles under normal and micro gravity conditions, *JSME Int. J. Series B* **41** (1998), 472-479.
12. A. Tomiyama, H. Tamai, I. Zun and S. Hosokawa, Transverse migration of single bubbles in simple shear flows, *Chem. Eng. Sci.* **57** (2002), 1849-1858.

# 5

# Virtual mass


## Abstract

In this chapter the virtual mass force was studied with a 3D Front Tracking model. With numerical simulations it was demonstrated that the virtual mass force coefficient does not depend on the physical properties of the dispersed and continuous phases, nor on the bubble diameter. Only the bubble shape and its orientation to the gravitational force are important and the numerical results show an excellent agreement with the analytical correlation by Tomiyama (2004) for ellipsoidal bubbles. Finally, this analytical correlation, which expresses the virtual mass coefficient (a function of the bubble aspect ratio), was combined with numerical results for the bubble aspect ratio for air bubbles in (ultra-pure) water, to arrive at a single integrated closure for the virtual mass coefficient as a function of the equivalent bubble diameter.

## 5.1 Introduction

In bubbly flows the density of the continuous phase is usually much higher than the density of the dispersed phase, so that the bubble resistance to acceleration is mainly determined by the mass of the displaced liquid, rather than the mass of the bubble. Since bubbly flows are almost always intrinsically unsteady (as e.g. in bubble columns), it is very important to account for the virtual (or added) mass force. The virtual mass force can be included in a force balance for the bubbles by adding a term in the momentum accumulation:

$$\left(\rho_G + C_{VM}\rho_L\right)V\frac{\partial\left(\mathbf{v}-\mathbf{u}\right)}{\partial t} = \sum_i \mathbf{F}_i \tag{5.1}$$

Eq. 5.1 introduces the virtual mass coefficient, which is defined as the liquid volume relative to the bubble volume that is displaced. It is well-known that the analytical value of the virtual mass coefficient for a (hard) sphere is equal to ½, meaning that half of the bubble volume in liquid has to be accelerated. Lamb (1932) has derived an expression for ellipsoidal bubbles, which was rearranged by Tomiyama (2004) in terms of the bubble aspect ratio ( $E$ ):

$$C_{VM} = \begin{cases} \dfrac{E\cos^{-1}E - \sqrt{1-E^2}}{E^2\sqrt{1-E^2} - E\cos^{-1}E} & E<1 \\ \dfrac{E\tanh^{-1}\left(E^{-1}\sqrt{E^2-1}\right) - \sqrt{E^2-1}}{E^2\sqrt{1-E^2} - E\tanh^{-1}\left(E^{-1}\sqrt{1-E^2}\right)} & E\geq 1 \end{cases} \tag{5.2}$$

In this chapter, a 3D Front Tracking model is used to confirm this correlation and provide additional validation of the model.

## 5.2 Numerical aspects

The numerical set-up used consists of a cubic domain of $100^3$ cells, with free-slip boundaries, in which an ellipsoidal bubble is centred, all initially at rest. The simulation is performed with only 10 time steps of 10 μs, enough to determine the virtual mass coefficient and the bubble deformation is still negligible. The virtual mass coefficient can be calculated from the bubble acceleration via a force balance without drag and lift forces, which are still negligible at this very early moment:

$$\left(\rho_G + C_{VM}\rho_L\right)V\frac{dv_z}{dt} = \left(\rho_L - \rho_G\right)Vg$$
$$C_{VM} = \frac{\rho_L - \rho_G}{\rho_L}\frac{g}{\frac{dv_z}{dt}} - \frac{\rho_G}{\rho_L} \tag{5.3}$$

It was found that the domain size and the numerical resolution inside the bubble determine the accuracy of the simulation results. Fig. 5.1 shows that for every box size there is an optimum resolution (= number of Eulerian cells on the equivalent bubble diameter), corresponding to a computational domain of approximately 4-5 bubble diameters. Also, it can be concluded that the standard setting of a $100^3$ grid with a bubble diameter of 20 Eulerian cells yields a virtual mass coefficient that is just 3% higher than the analytical value for a spherical bubble.

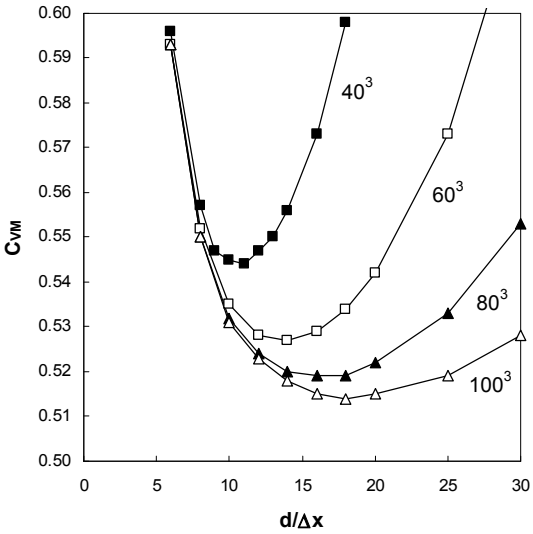


**Figure 5.1:** Virtual mass coefficient as a function of bubble resolution and the number of grid cells for a density ratio $\rho_G/\rho_L$ of 0.001.

## 5.3 Results

In this paragraph the influence of the physical properties and bubble diameter will be shown first, after which the effect of the bubble shape and its orientation on the virtual mass coefficient are studied.

### 5.3.1 Influence of physical properties and bubble diameter

The influence of all relevant physical properties (Table 5.1) on the virtual mass coefficient has been investigated over a wide range. First, it was confirmed that the dynamic viscosity of neither the dispersed nor the continuous phase has any effect on

the virtual mass coefficient, as expected. Secondly, the surface tension and bubble size have no effect, because the time-scale for bubble deformation (typically in the order of 0.1 second) is much longer than the simulated time.
It was found that with increasing density ratio of the gas and liquid phase virtual mass coefficient increases (Fig. 5.2). However, further research has shown that this was caused by the selected bubble resolution: at higher density ratios, a higher resolution in the bubble is required, because the flow patterns inside the bubble become important. Even for these high density ratios, the virtual mass coefficient shows first order convergence to the analytical value of ½ (see Fig. 5.3), and therefore it can be concluded that the density ratio also has no effect on the virtual mass coefficient.

**Table 5.1:** Physical properties and numerical settings for the virtual mass simulations.

| Property | Standard value | Simulated range |
|---|---|---|
| Liquid density [kg·m$^{-3}$] | 1000 | 1000 – 2000 |
| Liquid viscosity [Pa·s] | $1.0 \cdot 10^{-3}$ | $1.0 \cdot 10^{-3} – 1.0 \cdot 10^{-0}$ |
| Gas density [kg·m$^{-3}$] | 1 | 1 – 1000 |
| Gas viscosity [Pa·s] | $1.8 \cdot 10^{-5}$ | $1.0 \cdot 10^{-6} – 1.0 \cdot 10^{0}$ |
| Surface tension [N·m$^{-1}$] | $1.0 \cdot 10^{-2}$ | $0 – 1.0 \cdot 10^{-2}$ |
| Bubble size [m] | $1.0 \cdot 10^{-2}$ | $1.0 \cdot 10^{-3} – 2.0 \cdot 10^{-2}$ |
| Time step [s] | $1.0 \cdot 10^{-5}$ | |

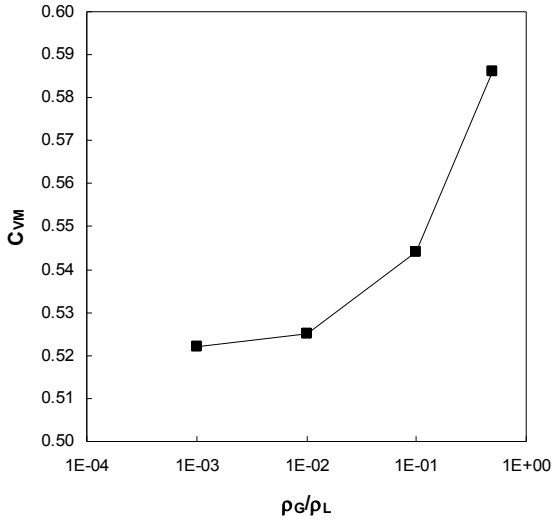


**Figure 5.2:** Virtual mass coefficient as a function of the density ratio using a $100^3$ computational grid.

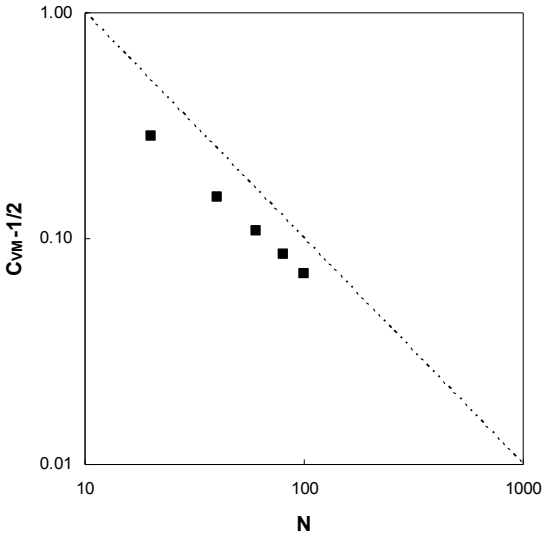


**Figure 5.3:** Convergence of the virtual mass coefficient for a density ratio of ½ (N = number of Eulerian grid cells per dimension).

### 5.3.2 Bubble shape and orientation

The bubble shape has been varied from oblate to prolate spheroids, using aspect ratios between 0.4 and 1.4. The numerical results are depicted in Fig. 5.4 and show a strong increase of the virtual mass coefficient for more oblate bubbles (lower E), simply because of the larger liquid volume that needs to be accelerated in comparison to a spherical bubble and a similar decrease in the virtual mass coefficient for prolate bubbles. An excellent agreement is achieved with the analytical correlation by Tomiyama (2004).

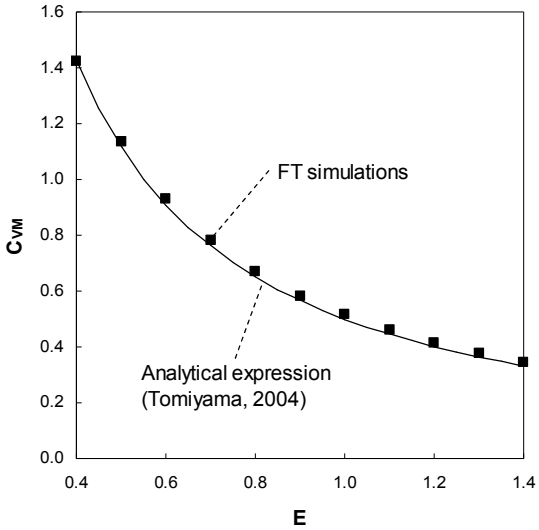


**Figure 5.4:** Virtual mass coefficient as a function of the bubble aspect ratio.

As an example, the influence of the orientation of an ellipsoid with an aspect ratio of 0.6 is shown in Fig. 5.5, which shows that the virtual mass coefficient changes smoothly from 0.9 to 0.4.

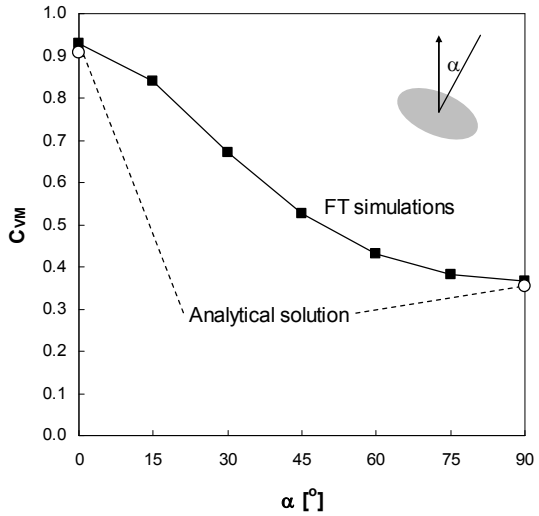


**Figure 5.5:** Virtual mass coefficient as a function of the bubble orientation for an ellipsoid with an aspect ratio of 0.6.

### 5.3.3 Application in the air-water system

Up until now, the virtual mass coefficient has been expressed as a function of the bubble aspect ratio, for which unfortunately an additional closure is required. Moreover, Zhang (2007) has shown that there are large discrepancies between a popular closure for the aspect ratio and FT simulations. This motivated us to integrate the knowledge about the aspect ratio of air bubbles in water (Chapter 3) with the correlation by Tomiyama (Fig. 5.6). A polynomial fit yields the following expression, that is easy to implement and computationally inexpensive:

$$C_{VM} = MIN\left(170435d^2 - 82d + \frac{1}{2},\ 1.25\right) \tag{5.5}$$

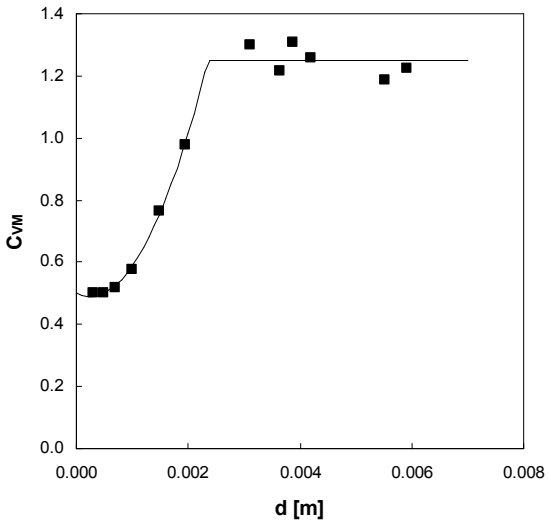


**Figure 5.6:** Virtual mass coefficient as a function of the bubble diameter for air bubbles in (ultra-pure) water.

## 5.4 Conclusions

The virtual mass force was studied with a 3D Front Tracking model. With numerical simulations it was shown that the virtual mass coefficient does not depend on the physical properties of the dispersed and continuous phases and the bubble size. Only the bubble shape and its orientation affected the virtual mass coefficient and the obtained numerical results agreed excellently with the analytical correlation by Tomiyama (2004). Finally, numerical results for the virtual mass coefficient have been combined with results for the bubble aspect ratio to obtain a single expression for the virtual mass force as a function of the equivalent bubble diameter for the important (ultra-pure) air-water system.

## Symbols

| | | |
|---|---|---|
| $C_{VM}$ | Virtual mass coefficient | - |
| $d$ | Equivalent bubble diameter | m |
| $E$ | Bubble aspect ratio | - |
| $\mathbf{F}_i$ | Force acting on the bubble | N |
| $g$ | Gravitational acceleration constant | $m \cdot s^{-2}$ |
| $N$ | Number of cells in each direction | - |
| $t$ | Time | s |
| $\mathbf{u}$ | Continuous phase velocity | $m \cdot s^{-1}$ |
| $\mathbf{v}$ | Bubble rise velocity | $m \cdot s^{-1}$ |
| $V$ | Bubble volume | $m^3$ |
| $\alpha$ | Angle between bubble normal and the vertical normal vector | $^o$ |
| $\rho$ | Density | $kg \cdot m^{-3}$ |

Subscripts

| | |
|---|---|
| $G$ | Gas phase |
| $L$ | Liquid phase |
| $z$ | Vertical direction |

## References

1. A. Tomiyama, Drag, lift and virtual mass forces acting on a single bubble, Third international symposium on two-phase flow modeling and experimentation, Pisa (2004).
2. H. Lamb, Hydrodynamics, 6th ed., Cambridge University Press, Cambridge (1932).
3. D. Zhang, Eulerian modeling of reactive gas-liquid flow in a bubble column, Ph.D. Thesis, University of Twente, The Netherlands (2007).

# 6

# Swarm effects


## Abstract

In this chapter the effect of the presence of neighbouring bubbles on the drag force has been investigated with DNS with full periodic boundary conditions. Air bubbles rising in a viscous liquid and water have been studied to examine this effect at low and high Reynolds numbers respectively. For both cases the drag force increases considerably when the gas fraction is raised to about 14%, although this effect is somewhat less at higher Reynolds numbers. At the same time, it has been observed that deformed bubbles become more elongated at higher gas fractions, which concurs with the hindrance effect. Moreover, it has been shown that the drag force exerted on spherical bubbles increases nearly linearly as a function of the gas fraction and that the relative drag increase does not depend on the Reynolds number for nearly spherical bubbles at low Reynolds numbers ($Re<1$).

## 6.1 Introduction

From literature it is known that closures derived for the drag force coefficient derived for single bubbles rising in an infinite, initially quiescent liquid are not generally applicable to describe bubbles in bubble columns with a significant gas hold-up. Moreover, dozens of empirical correlations to describe the bubble rise velocity in a swarm of bubbles have been proposed in the literature, most of which similar to the correlation of Richardson and Zaki (1954), who studied sedimentation of solid particles:

$$v_z - u_z = \left(v_{z,0} - u_{z,0}\right)\left(1-\varepsilon_G\right)^n \tag{6.1}$$

where $n$ is referred to in literature as the "Richardson and Zaki" exponent and $\varepsilon_g$ represents the local gas fraction. Exactly how much the rise velocity of a bubble in a swarm changes is still very much an open question, where many variables are involved, especially for large deformed bubbles. Nevertheless, qualitatively most literature agrees on the mechanisms involved: for small bubbles and low gas fractions the presence of neighbouring bubbles hinders the fluid flow and consequently the drag force is increased (Ishii and Zuber, 1979). Also turbulence in the continuous phase can cause an increase in drag as was found by Spelt and Biesheuvel (1997). Only for large deformed bubbles and high gas fractions a combination of the wake interaction, coalescence and bubble-induced turbulence may lower the drag coefficient (Simonnet et al., 2007). In their paper it was found that for air bubbles larger than 7 mm in water the drag force increases up to a gas fraction of 15%, after which it decreases sharply.

In sharp contrast, only very few articles have been published which deal with this subject using numerical simulations, even though the unique ability to control every parameter independently makes CFD ideally suited to study swarm effects. For instance Krishna et al. (1999) studied the interaction between very large spherical cap bubbles using a 2D axisymmetric VOF model. They found an acceleration of three to six times compared to an isolated bubble. Sankaranarayanan et al. (2002) studied the bubble-bubble interaction by simulating a single bubble in a periodic box with an implicit version of the lattice-Boltzmann model. They confirmed that for relatively small bubbles hindered rise occurs, while for highly distorted bubbles cooperative rise takes place.

In this chapter swarm effects on the drag force are investigated with a 3D Front Tracking model using full periodic boundary conditions. First, some numerical aspects will be highlighted, after which results for bubbles rising in a viscous liquid (low Reynolds number) and in water (high Reynolds number) will be described and discussed.

## 6.2 Numerical aspects

Air bubbles rising in two different liquids have been investigated in this chapter, to examine the swarm effects at low and high Reynolds numbers. Density and surface tension coefficient of both liquids was given the same value as water, so that only the dynamic viscosity was varied (Table 6.1). As a reference case, a single bubble is simulated using a large domain with free-slip boundaries (see Chapter 3) and the same physical properties. To mimic swarms of bubbles, the size of the fully periodic domain is adjusted to get the appropriate gas fraction (Fig. 6.1). The initial bubble diameter is kept constant at 20 Eulerian cells, which ensures that the resolution in all the simulations is identical. Both single bubbles as well as random patterns of four and eight bubbles in a periodic box have been studied.

The drag force coefficient for a bubble swarm is defined as the average of all the time-averaged drag coefficients of the bubbles, so that the total momentum exchange between the gas and liquid phases is correctly represented. Alternatively, the average velocity of the bubbles could have been used, but it was found that with this definition virtually identical results were obtained.

$$C_D = \frac{1}{N}\sum_{i=1}^{N} \frac{4d\left(\rho_L - \rho_G\right)g}{3\rho_L \left\langle \left(v_{z,i} - u_z\right)^2 \right\rangle} \tag{6.2}$$

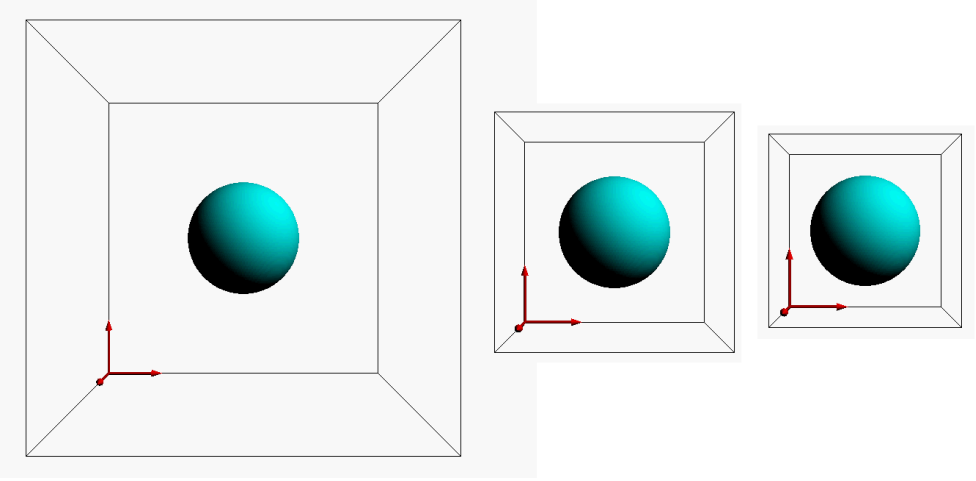

**Figure 6.1:** Initial bubble configuration for a single bubble with periodic boundaries, mimicking an infinite cubic array of bubbles. From left to right: 1.9, 8.2 and 14.0% gas fractions.

**Table 6.1:** Physical properties and numerical settings used for the simulations.

| Setting | Viscous case | Inviscid case |
|---|---|---|
| Gas density [kg·m$^{-3}$] | 1.25 | 1.25 |
| Gas viscosity [Pa·s] | $1.8 \cdot 10^{-5}$ | $1.8 \cdot 10^{-5}$ |
| Liquid density [kg·m$^{-3}$] | 1000 | 1000 |
| Liquid viscosity [Pa·s] | 0.1 | 0.001 |
| Surface tension [N·m] | 0.073 | 0.073 |
| Time step [s] | $1.0 \cdot 10^{-5}$ | $1.0 \cdot 10^{-5}$ |
| Grid size [m] | $5.0 \cdot 10^{-5} – 4.5 \cdot 10^{-4}$ | $5.0 \cdot 10^{-5} – 2.5 \cdot 10^{-4}$ |
| Number of grid cells [-] | $32^3$ - $100^3$ | $32^3$ - $100^3$ |

## 6.3 Results

First, the swarm effects will be investigated in a viscous liquid at low Reynolds numbers, where bubble induced turbulence does not play a role. The influence of the bubble diameter, gas hold-up and the Reynolds number on the drag force coefficient, bubble shape and flow profile is studied. Subsequently, the same is done for the industrially very important air-water system, i.e. high Reynolds number case.

### 6.3.1 Viscous liquid (low Re)

A viscous liquid is used first, to investigate the influence of bubble-bubble interactions at low Reynolds numbers. Figure 6.2 shows the relative drag coefficient as a function of the gas fraction, i.e. the drag coefficient for a single bubble in a periodic box compared to the drag coefficient for a single bubble in an infinite liquid. It can be seen that there is a general increase of the drag force when the gas fraction is increased, thereby confirming the experimentally observed hindrance effect at lower gas hold-ups. However, for larger bubbles the drag force coefficient decreases as a function of the gas hold-up, which is quite surprising. It should be stressed that all reference cases are grid-independent and their results do not change when using an inflow boundary condition (see Fig. 4.8). By comparing free-slip and periodic boundaries for a 9 mm bubble in a sufficiently large domain it can be seen that until 0.1 seconds the rise velocity is identical (Fig. 6.3). However, after this initial period, the bubble in the periodic domain starts to experience the wake of the ‘preceding’ bubble and the velocity increases much further until the liquid flow field becomes developed. Apparently, for large bubbles in a viscous liquid, both hindrance and wake-acceleration effects prevail. It is recommended to investigate this interesting result in more detail in future research.

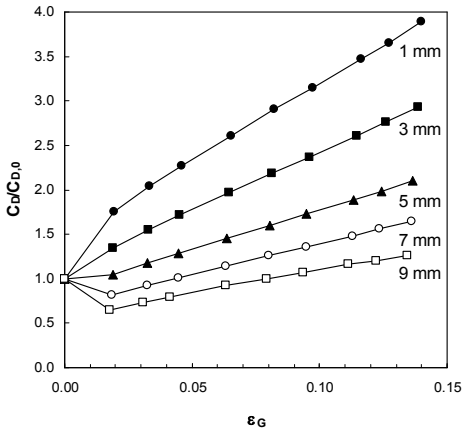


**Figure 6.2:** Relative drag coefficient versus gas fraction for a cubic array of bubbles in a viscous liquid.

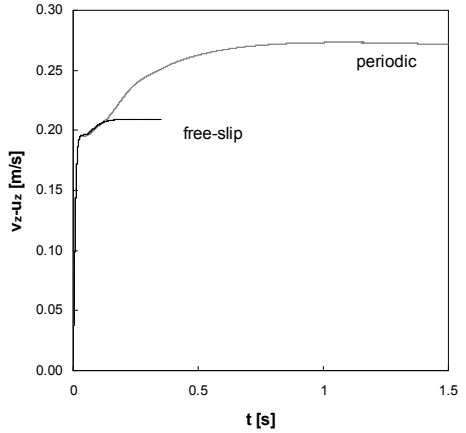


**Figure 6.3:** Bubble rise velocity for a 9 mm air bubble in a large domain, using free-slip and periodic boundary conditions.

In order to compare the shape of the bubbles, the aspect ratio (defined as height/width) is shown in Fig. 6.4. For small spherical bubbles (<3 mm) the shape is only slightly affected by its neighbours, while for larger bubbles there is a much more pronounced effect. It can be concluded that when the gas fraction is increased the bubbles become more elongated (see also Fig. 6.5 and 6.6), which is consistent with the observed hindrance effect.

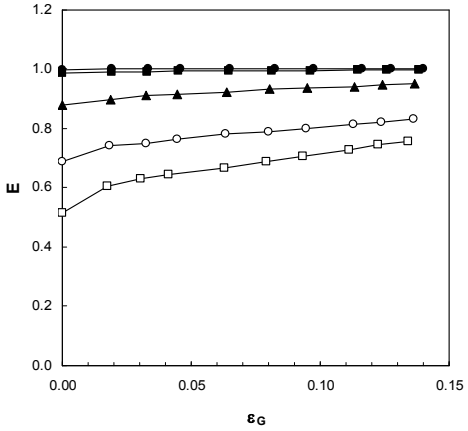


**Figure 6.4:** Bubble aspect ratio (height/width) versus gas fraction for a cubic array of air bubbles in a viscous liquid.

Now that the effects for a single bubble in a periodic box have been shown, they are compared to the case of multiple bubbles positioned randomly in a periodic box, to investigate the effect that the distance between the bubbles, and consequently the flow field and drag coefficient, can vary in time. Fig. 6.7 shows that for 1 and 5 mm bubbles there is no large difference, but – as expected – different random arrangements of bubbles result in slightly different average drag coefficients. It can also be seen that there is a large distribution in the relative drag coefficient for the individual bubbles, indicated with the error bars in Fig. 6.7. Also the bubble aspect ratio has been analyzed and Fig. 6.8 shows that there is hardly any difference between the single bubble and multiple bubble case for the small spherical bubbles, while the larger bubbles become slightly more deformed in the multiple bubble case. This is not surprising as the cubic array of bubbles (single bubble case) gives the highest resistance to deformation in the horizontal plane, while any other configuration (e.g. body centred cubic) is less restrictive in the horizontal plane, but more in other directions (multiple bubble case).
Unfortunately the simulations with multiple larger bubbles (7 and 9 mm) were not succesfull, because they all crashed once two bubbles approached each other very closely. Due to the very strong wake acceleration, the trailing bubble becomes strongly deformed in a very short period of time (see Fig. 6.9). It may very well be the very strong interface curvature compared to the grid resolution resulting in the numerical problems. In an attempt to solve this, a lower density ratio and smaller time steps have been tried without success. It is recommended for a follow-up project to investigate whether adaptive grid refinement can remediate these problems.

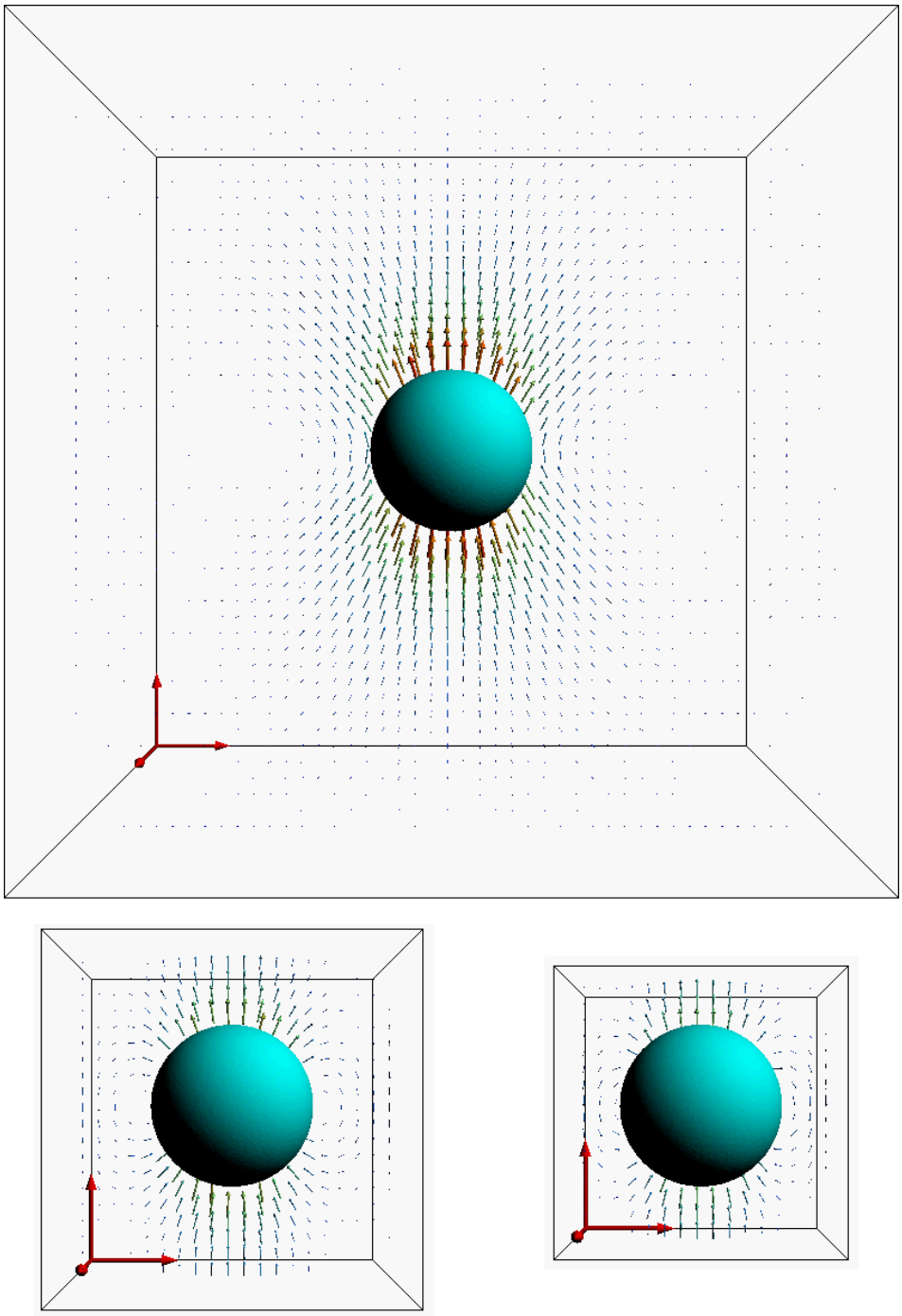

**Figure 6.5:** Flow profile around a 1 mm bubbles in the viscous liquid. Top: 'infinite' liquid; bottom: 6% and 13% gas hold-up.

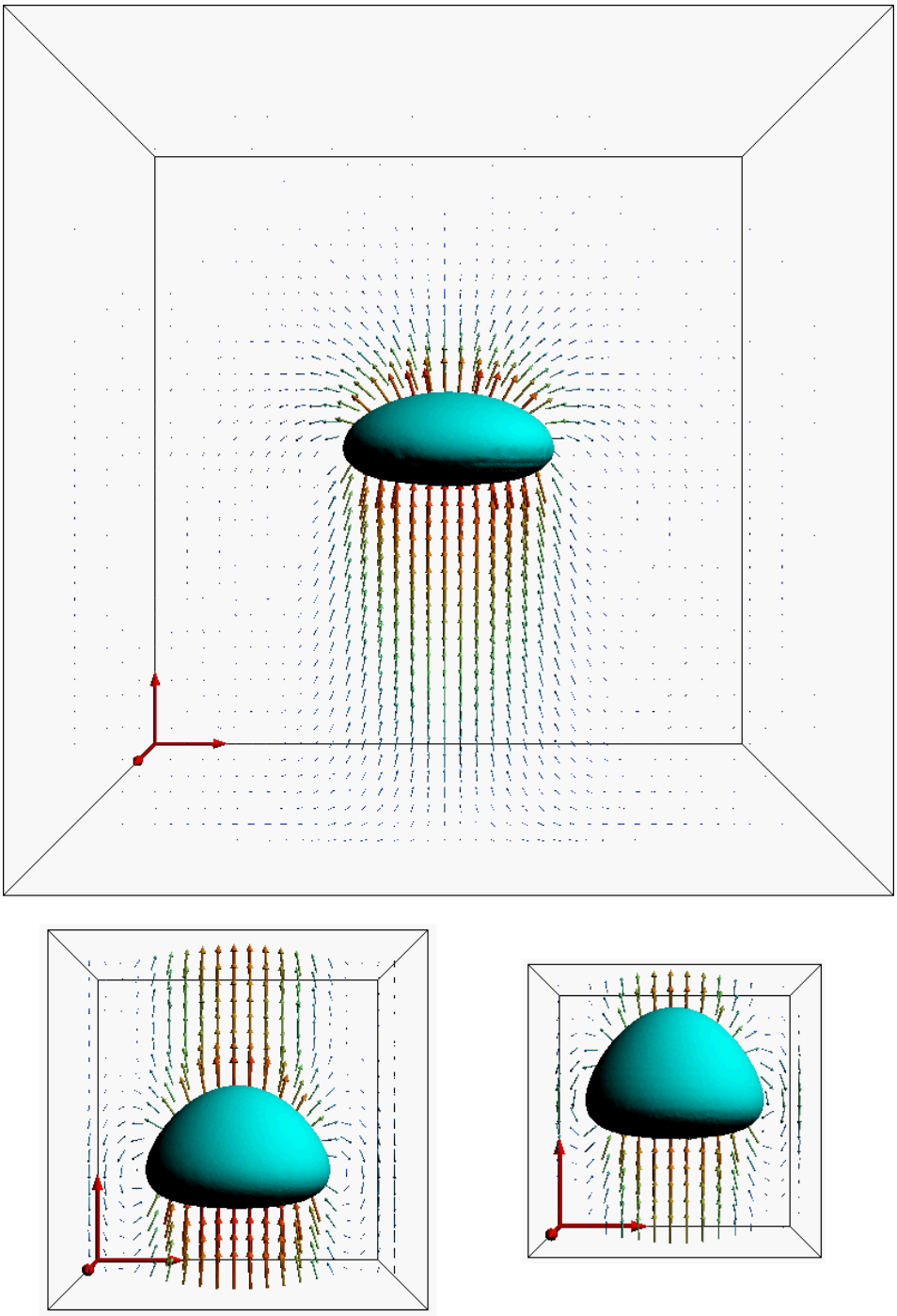

**Figure 6.6:** Flow profile around a 9 mm bubbles in the viscous liquid. Top: 'infinite' liquid; bottom: 6% and 13% gas hold-up.

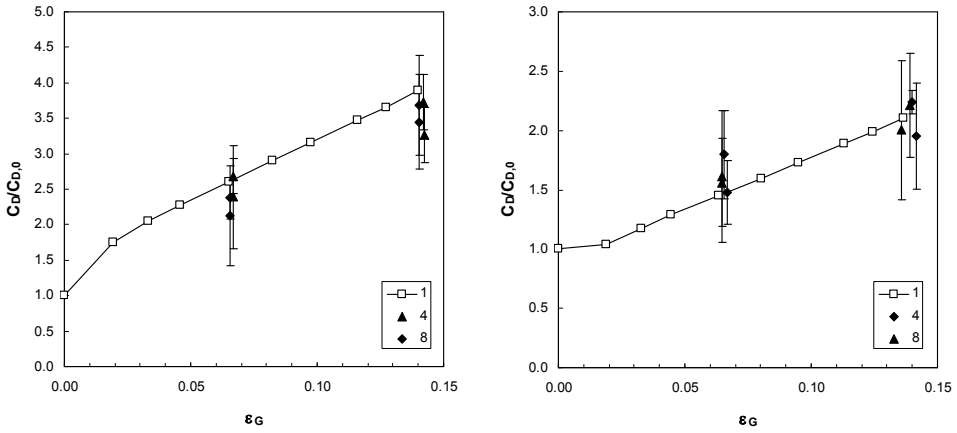


**Figure 6.7:** Comparison between the relative drag force coefficients obtained from a single bubble and random swarms consisting of 4 and 8 bubbles in a periodic box containing a viscous liquid as a function of the gas fraction. Left: 1 mm; right: 5 mm bubbles.

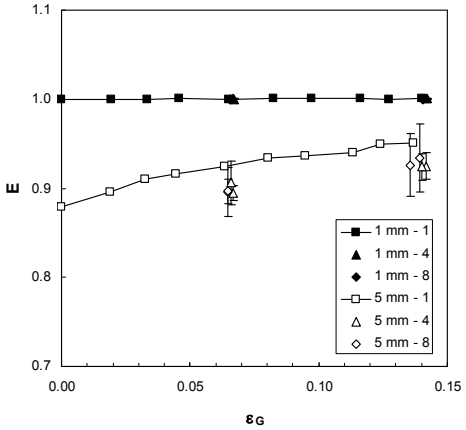


**Figure 6.8:** Comparison between the bubble aspect ratio obtained from a single bubble and random swarms consisting of 4 and 8 bubbles in a periodic box containing a viscous liquid, as a function of the gas fraction.

Finally, the influence of the Reynolds number on the relative drag coefficient is investigated separately, by only varying the liquid dynamic viscosity (0.05 – 0.80 Pa·s) for a 3 mm air bubble at 13% gas hold-up. This bubble retains a more or less its spherical shape, so that the Reynolds number can be varied independently. Fig. 6.10 shows that there is hardly any effect, even though the Reynolds number was varied over two orders of magnitude. Therefore, the conclusion is drawn that the relative increase in drag force is related to the size and shape of the bubble, i.e. Eötvös number, for Reynolds numbers up to about 1. At higher Reynolds numbers the relative drag increase diminishes with increasing Reynolds numbers.

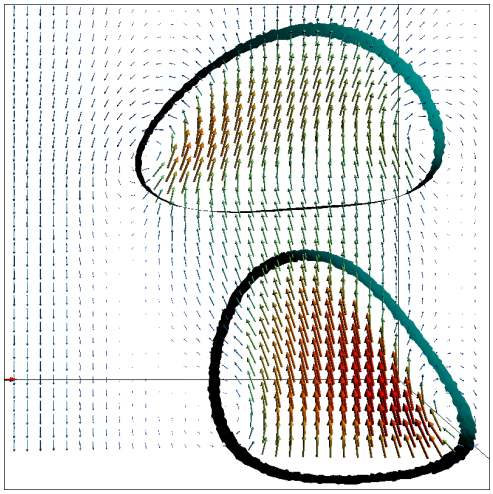

**Figure 6.9:** Strong bubble deformation due to wake-acceleration for two bubbles out of a random swarm of 9 mm bubbles, which may explain the observed numerical instability.

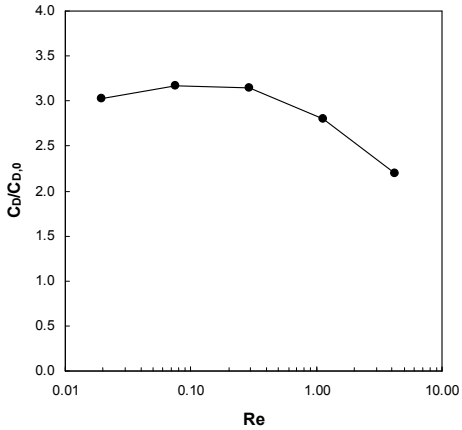


**Figure 6.10:** Relative drag coefficient versus the Reynolds number for a cubic array of nearly spherical 3 mm air bubbles rising in liquids with different viscosities.

## 6.3.2 Water (high Re)

Finally, the swarm effect on the drag force has been studied at higher Reynolds numbers (air bubbles in water). As expected, it was found that the flow is much more dynamic, also because the larger bubbles tend to oscillate and have path-instabilities. Fig. 6.11 shows that for 1–5 mm bubbles – similar to the viscous case – the drag coefficient increases with the gas fraction. This means that even with the very low viscosity of water, there is no net acceleration of the bubbles up to a diameter of 5 mm, which is in accordance with the experimental results by Simonnet et al. (2007). Contrary to the

viscous case, the drag increase is quite similar for all bubble diameters and it corresponds well to the empirical correlation by Behzadi et al. (2007).

Fig. 6.12 shows that the aspect ratio of the bubbles increases much less with the gas fraction than was observed for the viscous case and it bottoms out at a value around 0.5, which is similar to what was found to be the minimum aspect ratio in Chapter 3. Apparently, at higher Reynolds numbers the much lower hindrance effect allows bubbles to keep their shape. Finally, the velocity profiles around the bubbles are shown in Fig. 6.13 and 6.14, from which it is immediately clear that the bubble wakes are much more pronounced and there is a very dynamic bubble motion.

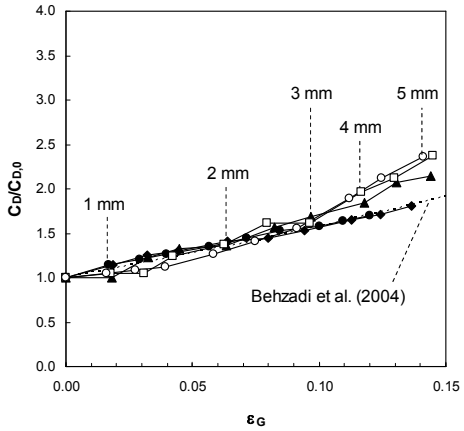


**Figure 6.11:** Relative drag coefficient versus gas fraction for a swarm of air bubbles rising in water (mimicked with a single bubble in a periodic box).

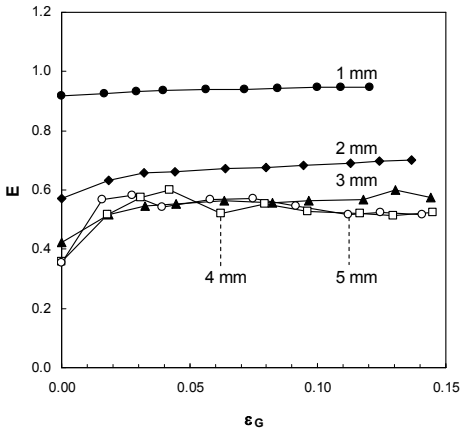


**Figure 6.12:** Bubble aspect ratio versus gas fraction for a swarm of air bubbles rising in water (mimicked with a single bubble in a periodic box).

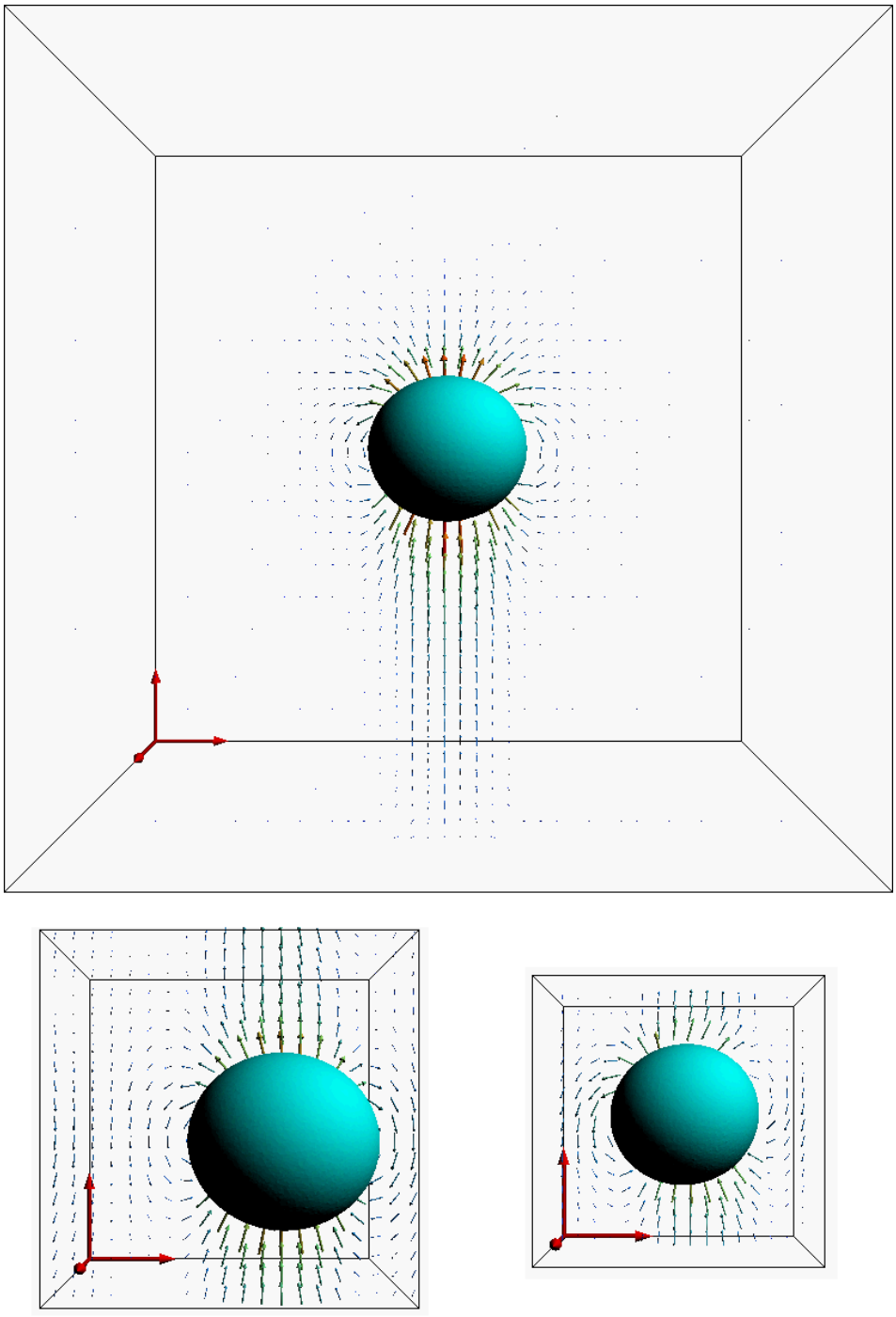

**Figure 6.13:** Flow profile around a 1 air bubble in water in a periodic box of different sizes. Top: 'infinite' liquid; bottom 6% and 13% gas hold-up.

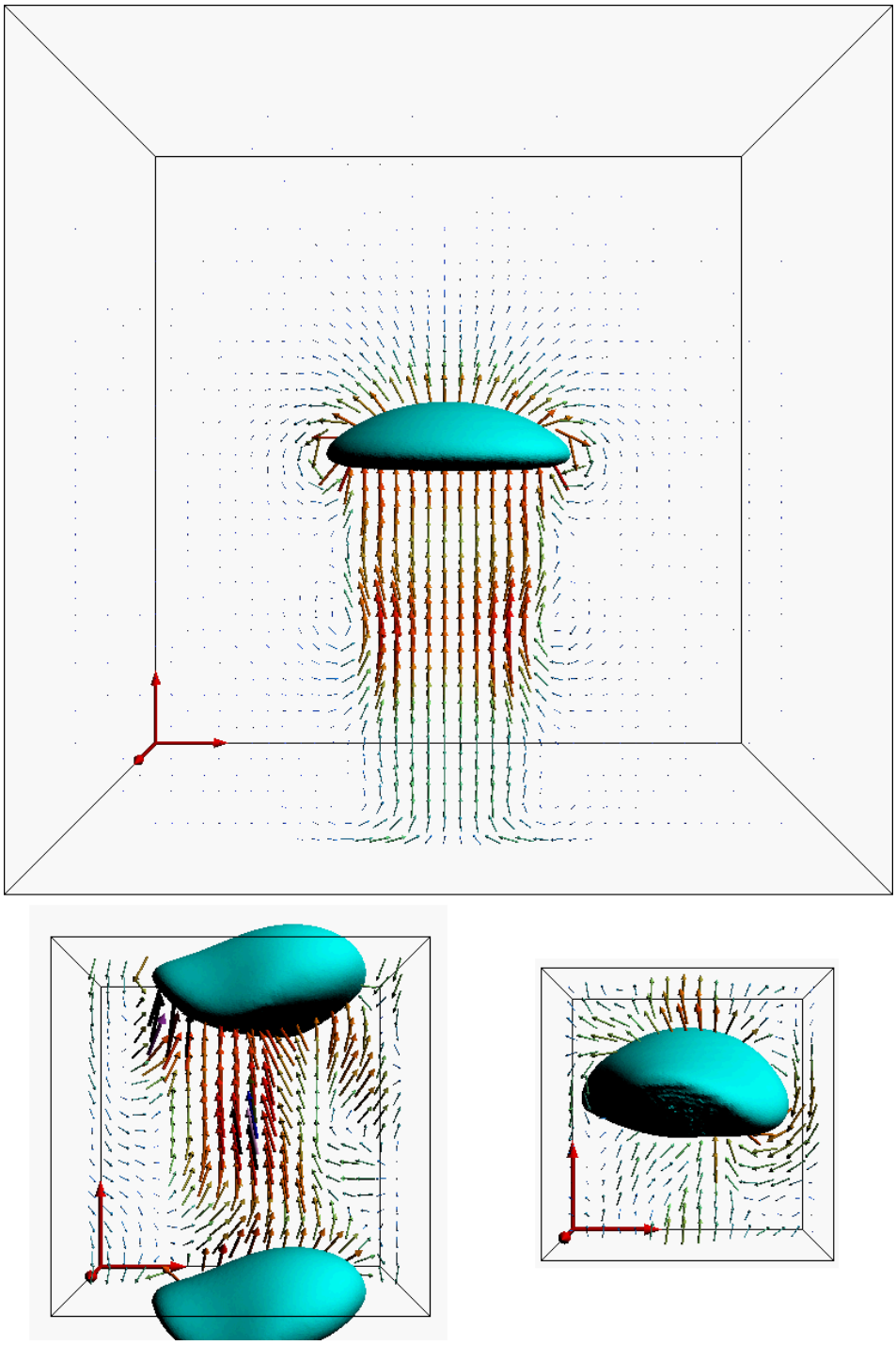

**Figure 6.14:** Flow profile around a 5 mm air bubble in water in a periodic box of different sizes. Top: 'infinite' liquid; bottom: 6% and 13% gas hold-up. Note that the bubble interfaces are snapshots and the bubble shape changes continuously.

## 6.4 Conclusions

In this chapter the effect of bubble swarms on the drag force was studied with a FT model using full periodic boundary conditions, up to a gas fraction of about 14%. It was found that for air bubbles rising in both a viscous liquid and water the relative drag force coefficient increases nearly linearly with the gas fraction, although this increase was much less pronounced in water. Secondly, it was found that deformable bubbles become more elongated at higher gas hold-ups, thereby confirming the hindrance effect. For a swarm of air bubbles in water, this elongation effect stops at a minimum bubble aspect ratio of about 0.5; at this point shape oscillations set in. Finally, it was shown that the relative drag increase is not a function of the Reynolds number at lower Reynolds numbers (Re<1), at least for almost spherical bubbles.

## Symbols

| | | |
|---|---|---|
| $d$ | Equivalent bubble diameter | m |
| $Eo$ | Eötvös number ( $Eo = g\left(\rho_L - \rho_G\right)d^2\sigma^{-1}$ ) | - |
| $g$ | Gravitational constant | $m \cdot s^{-2}$ |
| $i$ | Bubble index | - |
| $n$ | Richardson-Zaki exponent | - |
| $N$ | Number of bubbles | - |
| Re | Reynolds number ( $\mathrm{Re} = \rho_L \left\lvert \mathbf{v} - \mathbf{u} \right\rvert d\eta_L^{-1}$ ) | - |
| $t$ | Time | s |
| $v$ | Bubble velocity | $m \cdot s^{-1}$ |
| $u$ | Continuous phase velocity | $m \cdot s^{-1}$ |
| $\varepsilon_G$ | Gas volume fraction | - |
| $\eta$ | Dynamic viscosity | Pa·s |
| $\rho$ | Density | $kg \cdot m^{-3}$ |
| $\sigma$ | Surface tension coefficient | $N \cdot m^{-1}$ |

Subscripts:

| | |
|---|---|
| $G$ | Gas phase |
| $L$ | Liquid phase |
| $z$ | Vertical direction |
| 0 | At zero gas hold-up (bubble in an 'infinite' liquid) |

## References

1. A. Behzadi, R.I. Issa and H. Rusche, Modelling of dispersed bubble and droplet flow at high phase fractions, *Chem. Eng. Sci.* **59** (2004), 759-770.
2. J. Hadamard, Movement permanent lent d'une sphere liquide et visqueuse dans un liquide visqueux, *Comptes Rendus* **152** (1911), 1735.
3. M. Ishii and N. Zuber, Drag coefficient and relative velocity in bubbly, droplet or particulate flows, *AIChE J.* **25** (1979), 843–855.

4. R. Krishna, M. Urseanu, J. van Baten and J. Ellenberger, Rise velocity of a swarm of large gas bubbles in liquids, *Chem. Eng. Sci.* **54** (1999), 171-183.
5. J.F. Richardson and W.N. Zaki, Sedimentation and fluidization, *Trans. Inst. Chem. Engrs.* **32** (1954), 35-53.
6. K. Sankaranarayanan, X. Shan, I.G. Kevrekidis and S. Sundaresan, Analysis of drag and virtual mass forces in bubbly suspensions using an implicit formulation of the lattice Boltzmann method, *J. Fl. Mech.* **452** (2002), 61-96.
7. M. Simonnet, C. Gentric, E. Olmos and N. Midoux, Experimental determination of the drag coefficient in a swarm of bubbles, *Chem. Eng. Sci.* **62** (2007), 858-866.
8. P. Spelt and A. Biesheuvel, On the motion of gas bubbles in homogeneous isotropic turbulence, *J. Fl. Mech.* **336** (1997), 221-244.

# List of publications

## Journal publications

1. W. Dijkhuizen, E.I.V. van den Hengel, N.G. Deen, M. van Sint Annaland and J.A.M. Kuipers, Numerical investigation of closures for interface forces acting on single air-bubbles in water using Volume of Fluid and Front Tracking models, *Chem. Eng. Sci.* **60** (2005), 6169-6175.
2. M. van Sint Annaland, W. Dijkhuizen, N.G. Deen and J.A.M. Kuipers, Numerical simulation of gas bubbles behaviour using a 3D Front Tracking method, *AIChE J.* **52** (2006), 99-110.
3. W. Dijkhuizen, G.A. Bokkers, N.G. Deen, M. van Sint Annaland and J.A.M. Kuipers, Extension of PIV for measuring granular temperature field in dense fluidized beds, *AIChE J.* **53** (2007), 108-118.
4. W. Dijkhuizen, R. Meijer, N.G. Deen, M. van Sint Annaland and J.A.M. Kuipers. Experimental and numerical study of air bubbles rising in a viscous liquid, in preparation.
5. W. Dijkhuizen, M. van Sint Annaland, J.A.M. Kuipers, An improved 3D Front Tracking method, in preparation.
6. W. Dijkhuizen, M. van Sint Annaland, J.A.M. Kuipers, Numerical investigation of the drag force acting on single air bubbles, in preparation.
7. W. Dijkhuizen, M.S. van Buijtenen, M. van Sint Annaland and J.A.M. Kuipers, Numerical and experimental investigation of the lift force acting on single air bubbles, in preparation.
8. W. Dijkhuizen, M. van Sint Annaland, J.A.M. Kuipers, Direct numerical simulation of the influence of bubble swarms on the drag force, in preparation.

## Conference proceedings

1. N.G. Deen, W. Dijkhuizen, G.A. Bokkers, M. van Sint Annaland and J.A.M. Kuipers, Validation of the granular temperature prediction of the kinetic theory of granular flow by particle image velocimetry and a discrete particle model, proceedings of the 3rd Int. Symposium on Two-Phase Flow Modelling and Experimentation, Pisa, 22-24 September 2004.
2. W. Dijkhuizen, M. van Sint Annaland and J.A.M. Kuipers, Derivation of closures for single air bubbles in water using an improved 3D front tracking model, Proceedings of the 11th Workshop on Two-Phase Flow Predictions, Merseburg, April 5-8, 2005.
3. W. Dijkhuizen, M. van Sint Annaland and J.A.M. Kuipers, Numerical investigations of closures for interface forces in dispersed flows using a 3D front tracking model, CFD2005, Trondheim, Norway, June 2005.
4. W. Dijkhuizen, E.I.V. van den Hengel, M. van Sint Annaland and J.A.M. Kuipers, Numerical investigation of closures for interface forces in dispersed gas-liquid flows using volume of fluid and front tracking models, 7th conference on Gas-

Liquid & Gas-Liquid-Solid reactor engineering, Strasbourg, France, August 21-24, 2005.

5. W. Dijkhuizen, M. van Sint Annaland and J.A.M. Kuipers: Numerical investigation of the lift force acting on single air bubbles in liquids with different viscosities using a 3D Front-Tracking method, Euromech Colloquium 479, Numerical Simulation of Multiphase Flow with Deformable Interfaces, Scheveningen, The Netherlands, August 14-16, 2006.
6. D. Darmana, W. Dijkhuizen, N.G. Deen, M. van Sint Annaland and J.A.M. Kuipers, Detailed 3D Modelling of Mass Transfer Processes in Two Phase Flows with Dynamics Interfaces, ICMF2007, Leipzig, Germany, July 9-13, 2007.
7. W. Dijkhuizen, M. van Sint Annaland and J.A.M. Kuipers, Direct numerical simulation of the drag force in bubble swarms, ICMF 2007, Leipzig, Germany, July 9-13, 2007.
8. W. Dijkhuizen, M. van Sint Annaland, J.A.M. Kuipers. Direct numerical simulation of the lift force in bubbly flows, CFD2008, Trondheim, Norway, June 10-12, 2008.
9. W. Dijkhuizen, I. Roghair, M. van Sint Annaland, J.A.M. Kuipers. Numerical derivation of the drag force coefficient in bubble swarms using a Front Tracking model, CFD2008, Trondheim, Norway, June 10-12, 2008.
10. I. Roghair, W. Dijkhuizen, M. van Sint Annaland, J.A.M. Kuipers. Front Tracking simulations on liquid-liquid systems; an investigation of the drag force on droplets, CFD2008, Trondheim, Norway, June 10-12, 2008.

# Levensloop

Wouter Dijkhuizen werd op 21 april 1980 geboren te Zevenaar. Aldaar groeide hij op en bezocht er de lagere school ‘de Terebinth’. Vanaf 1992 bezocht hij het Liemers College, waar in 1998 het VWO diploma behaald werd.

In september 1998 begon hij aan de ingenieursopleiding Chemische Technologie aan de Universiteit Twente. In het kader van deze opleiding werd in 2002 stage gelopen bij SABIC te Gelsenkirchen, Duitsland. In december 2003 studeerde hij met lof af bij de werkeenheid Fundamentele Aspecten van de Proceskunde op de ontwikkeling van een meetmethode voor de granulaire temperatuur in wervelbedden.

Na afloop van zijn studie trad hij bij dezelfde werkeenheid in dienst als onderzoeker in opleiding om onderzoek te verrichten naar sluitingsrelaties voor stromingen met bellen met behulp van directe numerieke simulaties. De resultaten van dit onderzoek staan beschreven in dit proefschrift.

Sinds februari 2008 werkt hij als onderzoeker bij SINTEF Materials & Chemistry in Trondheim, Noorwegen.

# Dankwoord

Als eerste wil ik Hans Kuipers van harte bedanken voor het aanbod om een promotieopdracht uit te voeren. Het was een buitengewone kans om betrokken te zijn bij de ontwikkeling van het Front Tracking model dat je uit jouw kelder tevoorschijn toverde. Gaandeweg in het proces bleek meerdere keren dat als we dachten een probleem opgelost te hebben, dit toch niet de beperkende factor was. Wat mij vooral opviel was jouw geduld tijdens de maandelijkse meetings, wat met name van belang was tijdens de ontwikkeling van het hogere orde oppervlaktespanningsmodel. Helaas heeft dit niet tot een resultaat geleid, maar gelukkig hebben alle andere veranderingen wel hun nut getoond in dit proefschrift. Ik hoop dat we in de toekomst hier smakelijk om kunnen lachen!

Voor de dagelijkse begeleiding ben ik zeer veel dank verschuldigd aan Martin van Sint Annaland. Zijn uitzonderlijk brede kennis van verschillende numerieke modellen stond altijd garant voor verse ideeën waar ik weer verder mee kon. De brainstorm sessies waarbij talrijke verbeteringen werden uitgedacht zullen mij nog lang bijblijven. Bovendien heeft zijn kennis van de Engelse taal in een belangrijke mate bijgedragen aan de structuur van de tekst in dit proefschrift, door het toepassen van langere zinnen met de juiste logische verbindingen.

Natuurlijk was dit project niet mogelijk zonder de financiële steun van Stichting FOM en Shell Global Solutions. Jennifer Kockx, Peter Veenstra en Wouter Harteveld wil ik tevens bedanken voor hun interesse en inbreng tijdens de review meetings.

Tijdens mijn promotie heb ik twee studenten mogen begeleiden. Allereerst was er Jelle de Jong die zijn Bacheloropdracht invulde met metingen en simulaties voor de stijgsnelheid van enkele bellen in glycerine. De resultaten waren dusdanig veelbelovend dat deze hierna hebben geleid tot een uitgebreide serie experimenten. Maureen van Buijtenen heeft haar Masteropdracht gedaan met als doel het bestuderen van de liftkracht voor enkele bellen en de wrijvingskracht voor zwermen bellen. Hiervoor werd een experimentele opstelling gebouwd en zijn de eerste verkennende metingen hiermee uitgevoerd. Tevens zijn periodieke randvoorwaarden ingebouwd in het Front Tracking model, wat uiteindelijk nogal wat voeten in aarde bleek te hebben. Nogmaals van harte bedankt voor jullie inzet!

Een proefschrift met de focus op numerieke simulaties is natuurlijk niets zonder goed functionerende computerclusters. Ik wil hiervoor niet alleen Robert Meijer als systeembeheerder bedanken, maar ook alle AIO's die zich in de loop der jaren hiervoor in hebben gezet: Dadan, Christiaan, Willem en Sebastiaan. Met name het opbouwen van het speciaal voor Front Tracking berekeningen geselecteerde Donald cluster, zal mij nog lang bijblijven.

Ik wil Wim Leppink van harte bedanken voor het ontwerpen en maken van de opstelling om de liftkracht te meten. Zijn oog voor detail heeft geleid tot een indrukwekkende opstelling, gebouwd volgens zijn 'Deutsche Gründlichkeit'. Tevens waren hij en Gerrit Schorfhaar altijd dichtbij voor allerhande technische bijstand.

Nicole Haitjema wil ik bedanken voor de uitmuntende secretariële ondersteuning. Een half woord was al genoeg en je wist feilloos de weg te vinden binnen de UT. Tijdens haar zwangerschap werden haar taken waargenomen door Ans Wassink, die ik wil bedanken voor het versturen van de correcties en de brieven naar de commissie.

Dan komen we bij het sociale gedeelte, welke minstens zo belangrijk is voor succesvol onderzoek. Het gaat te ver om iedereen te noemen, maar ik wil alle oud-collega's en studenten van FAP en OOIP bedanken voor de gezellige pauzes, borrels bij de Vlugtheuvel en activiteiten als het zeilweekend. In de loop der jaren hebben verschillende borrelcommissarissen de revue gepasseerd: Renske, Jan Albert, Sander en Sebastiaan. Ook Joris en Tymen horen in dit rijtje als organisatoren van de Vlugterlab lezingen. Met het verdwijnen van de oude garde stopte helaas het klaverjassen tijdens de middagpauze, maar op een gegeven moment kwam de mensa hiervoor in de plaats. Hiervoor wil ik Christiaan, Jan Albert, Sebastiaan, Peter, Jacco en Jens bedanken. Toevallig of niet: deze mensen waren ook menige donderdag na werktijd te vinden in de borrelkelder van Alembic, waar het begrip 'laatste biertje' een geheel nieuwe betekenis kreeg.

Tevens wil ik de contact-AIO's van het Burgerscentrum bedanken voor de gezellige etentjes in Amersfoort, die de contacten tussen de verschillende groepen en universiteiten zeker ten goede kwam. Met name tijdens de FOMdagen, Burgersdag en NPS kwamen we elkaar telkens weer tegen.

Liesbeth Kuipers wil ik bedanken voor het organiseren van menig vakgroepuitje. De eerste 'werkweek' van mijn promotie was meteen goed gevuld met een skivakantie naar Flaine. Verder waren er de kleinere skitrips naar Winterberg en het jaarlijkse Waarbeekfeest, waarbij de gehele groep bijeen werd gebracht.

Buiten het werk waren er ook nog de nodige sportactiviteiten bij volleybalvereniging Harambee en wielervereniging Klein Verzet. Met die laatste werd ook regelmatig een weekend of vakantie doorgebracht in de Ardennen of Alpen met de racefiets of mountainbike. Iedereen van harte bedankt voor de gezelligheid door de jaren heen!

Voor het regelen van allerlei zaken terwijl ik in Noorwegen zit en assistentie tijdens de verdediging, ben ik zeer veel dank verschuldigd aan mijn paranimfen Jan Albert en Sander. Beide zijn oud-collega's en vertegenwoordigen respectievelijk de 'balletjes' en 'chemie', zodat ik verdwaalde vragen over deze onderwerpen tijdens de verdediging aan hen kan doorsturen.

Als laatste wil ik mijn ouders en broertje bedanken voor hun vertrouwen en geduld, terwijl zij niet altijd begrepen waar ik me mee bezig hield. Ik hoop dat in ieder geval duidelijk is geworden dat onderzoek naar belletjes leidt tot een goed vakantieadres in het buitenland.

Nogmaals iedereen van harte bedankt!

Wouter